Numerical simulations of binary neutron star merger ejecta

Numerische Simulationen des Auswurfmaterials von Neutronensternverschmelzungen
Zur Erlangung des Grades eines Doktors der Naturwissenschaften (Dr. rer. nat.)
Genehmigte Dissertation im Fachbereich Physik von Christian Schwebler
Tag der Einreichung: 22. April 2025, Tag der Prüfung: 19. Mai 2025

1. Gutachten: Prof. Dr. Gabriel Martínez-Pinedo
2. Gutachten: Priv.-Doz. Dr. Andreas Bauswein
Darmstadt, Technische Universität Darmstadt

TECHNISCHE
UNIVERSITÄT
DARMSTADT

Physics Department
Institut für Kernphysik
Theoretical Nuclear
Astrophysics

Numerical simulations of binary neutron star merger ejecta
Numerische Simulationen des Auswurfmaterials von Neutronensternverschmelzungen

Accepted doctoral thesis in the department of Physics by Christian Schwebler

Date of submission: 22. April 2025
Date of thesis defense: 19. Mai 2025

Darmstadt, Technische Universität Darmstadt

Bitte zitieren Sie dieses Dokument als:
URN: urn:nbn:de:tuda-tuprints-299658
URL: https://tuprints.ulb.tu-darmstadt.de/29965
Jahr der Veröffentlichung auf TUprints: 2025

Gewidmet meinen Vater Richard

Erklärungen laut Promotionsordnung

§ 8 Abs. 1 lit. d PromO

Ich versichere hiermit, dass zu einem vorherigen Zeitpunkt noch keine Promotion versucht wurde. In diesem Fall sind nähere Angaben über Zeitpunkt, Hochschule, Dissertationsthema und Ergebnis dieses Versuchs mitzuteilen.

§ 9 Abs. 1 PromO

Ich versichere hiermit, dass die vorliegende Dissertation – abgesehen von den in ihr ausdrücklich genannten Hilfen – selbstständig verfasst wurde und dass die „Grundsätze zur Sicherung guter wissenschaftlicher Praxis an der Technischen Universität Darmstadt" und die „Leitlinien zum Umgang mit digitalen Forschungsdaten an der TU Darmstadt" in den jeweils aktuellen Versionen bei der Verfassung der Dissertation beachtet wurden.

§ 9 Abs. 2 PromO

Die Arbeit hat bisher noch nicht zu Prüfungszwecken gedient.

Darmstadt, 22. April 2025

C. Schwebler

Abstract

Improving numerical simulations of binary neutron star mergers (BNSM) is essential for advancing our understanding of and ability to interpret observations of these events. We demonstrate that smoothed particle hydrodynamic simulations of BNSM yield differing outcomes for identical merger events. This thesis is the first study to explore these variations, considering the possibility that they may be physical stochastic effects arising from small initial perturbations. We perform simulations of a 1.35-1.35 solar mass binary system with the same physical and numerical setup and discuss the observed variation in ejecta properties and the post-merger gravitational wave signal. We find an antiproportional correlation between the ejecta mass and the amplitude of the main feature f_{peak} of the gravitational wave frequency spectrum. We show that these fluctuations depend on how the double core structure evolves after merging. Our simulations do not yield a reduction of these variations when increasing the resolution, which might be an indication that these fluctuations are a physical effect.

To make reliable predictions for the electromagnetic signal of merger events, it is necessary to evolve the mass-outflows on timescales which are significantly longer than the merger itself. Over this time, the ejecta dilutes and cools down over several orders of magnitude. We present a method to extend tabulated equation of states (EoS) to encompass lower rest-mass densities and temperatures. We investigate the issue that outflowing matter evolve towards negative internal energies in regions of low resolution in our simulations. We improve the discretization of the general-relativistic energy evolution equation to reduce the occurrence of this issue. Utilizing the extended EoS and the improved discretization of the energy equation, we perform a long-term BNSM simulation up to 250 milliseconds after merger. We estimate how much material reaches homologous expansion within this time. Our analysis indicates that the majority of the material expelled during the first 25 milliseconds nearly exhibits homologous expansion, and we estimate an upper bound of 10% for the alteration in its radial velocity. For later ejecta, we observe that they attain a reduced velocity, requiring a duration on the order of seconds to reach homologous expansion. BNSM simulations of this length require a sufficient resolution of the expanding ejecta. We present a method to efficiently increase the resolution of BNSM ejecta in smoothed particle hydrodynamic simulations. We implement particle splitting, test different splitting criteria, and conduct a comparative study between simulations with and without particle splitting. Our findings indicate that the resolution of the BNSM ejecta can be enhanced by a factor of five using our proposed method while maintaining similar computational expenses.

Zusammenfassung

Die Verbesserung numerischer Simulationen von der Verschmelzung von binären Neutronensternsystemen (BNSM) ist für ein besseres Verständnis und eine bessere Interpretation von Beobachtungen dieser Phänomene von wesentlicher Bedeutung. Wir zeigen, dass Smoothed-Particle-Hydrodynamics-Simulationen von BNSM für identische Kollisionen unterschiedliche Ergebnisse liefern. Diese Arbeit ist die erste Studie, die diese Abweichungen untersucht und dabei die Möglichkeit in Betracht zieht, dass es sich um physikalische stochastische Effekte handelt, die durch winzige Perturbationen entstehen. Wir führen Simulationen eines 1,35-1,35-Sonnenmassen Binärsystems mit demselben physikalischen und numerischen Aufbau durch und diskutieren die beobachteten Variationen in den Ejekta-Eigenschaften und dem Gravitationswellensignal nach der Verschmelzung. Wir finden eine antiproportionale Korrelation zwischen der Ejekta-Masse und der Amplitude des Hauptmerkmals f_{peak} des Gravitationswellenfrequenzspektrums. Wir zeigen, dass diese Fluktuationen davon abhängen, wie sich die Doppelkernstruktur nach der Verschmelzung entwickelt. Wir sehen keine Verringerung dieser Schwankungen durch eine Erhöhung der Auflösung, was ein Hinweis darauf sein könnte, dass diese Fluktuationen ein physikalischer Effekt sind.

Um zuverlässige Vorhersagen über das elektromagnetische Signal von BNSM machen zu können, müssen die Massenauswürfe auf Zeitskalen entwickelt werden, die deutlich länger sind als die Kollision selbst. Während dieser Zeit verdünnt sich das ausgeworfene Material und kühlt über mehrere Größenordnungen ab. Wir stellen eine Methode zur Erweiterung der tabellierten Zustandsgleichungen (EoS) vor, um niedrigere Ruhemassendichten und Temperaturen zu berücksichtigen. Wir untersuchen das dabei auftretende Problem, dass sich die ausströmende Materie in unseren Simulationen in Regionen mit geringer Auflösung zu negativen inneren Energien entwickelt. Wir verbessern die Diskretisierung der allgemeinen relativistischen Energieentwicklungsgleichung, um das Auftreten dieses Problems zu reduzieren. Unter Verwendung der erweiterten EoS und der verbesserten Diskretisierung der Energiegleichung führen wir eine Langzeit-BNSM-Simulation bis zu 250 ms nach der Fusion durch. Wir schätzen ab, wie viel Material innerhalb dieser Zeit eine homologe Expansion erreicht. Unsere Analyse zeigt, dass der Großteil des in den ersten 25 ms ausgestoßenen Materials nahezu homologe Expansion aufweist, und wir erhalten ein geschätzte Obergrenze von 10% für die Änderung der Radialgeschwindigkeit. Für spätere Ejekta stellen wir fest, dass sie eine geringere Geschwindigkeit aufweisen und typischerweise einige Sekunden benötigen, bis zum erreichen einer homologen Ausdehnung. Für BNSM-Simulationen dieser Länge ist eine ausreichende Auflösung der expandierenden Ejekta erforderlich. Wir stellen eine Methode vor, um die Auflösung der

BNSM-Ejekta in Smoothed-Particle-Hydrodynamics-Simulationen effizient zu erhöhen. Wir implementieren Teilchen-Splitting, testen verschiedene Splitting-Kriterien und führen eine vergleichende Studie zwischen Simulationen mit und ohne Teilchen-Splitting durch. Wir stellen fest, dass wir mit der von uns vorgestellten Methode die Auflösung der BNSM-Ejekta bei vergleichbarem Rechenaufwand um einen Faktor fünf verbessern können.

Contents

List of acronyms

Notation	Description
ADM	Arnowitt-Deser-Misner
BH	black hole
BNS	binary neutron star
BNSM	binary neutron star merger
CFC	conformal flatness condition
EoS	equation of state
GW	gravitational wave
GRHD	general relativistic hydrodynamic
HMNS	hyper massive neutron star
NS	neutron star
SPH	smoothed particle hydrodynamics
SD	symmetric discretized
AD	asymmetric discretized

1. Introduction

1.1. Physical Context

Neutron stars

neutron stars (NSs) are remnants of massive explosions. At the end of the life cycle of stars with initial masses of at least 8 $M_\odot$ they explode in a core-collapse supernova ([1–3]). Depending on the mass of the progenitor star its core either collapse into a black hole (BH) or forms a proto-neutron star. This hot proto-neutron star with temperatures of several 10 MeV will start to cool down by neutrino emission. Through this process, the temperature decreases to the point where the thermal energy of neutrons and leptons is negligible compared to their Fermi energy, resulting in what is called a cold NS. NSs are the most compact known stable objects in the universe with typical mass ranges from around 1 to 2-3 $M_\odot$ while only having radii of 10-15 km [4]. Therefore, their core densities surpass several times the nuclear saturation density ($\rho_{\text{sat}} \sim 2.7 \times 10^{14}\,\text{gcm}^{-3}$). The lower limit of possible NS masses is limited by the formation mechanism. The maximum mass and the mass-radius relationship are still uncertain due to incomplete knowledge of the equation of state (EoS).

Equation of State

The EoS of a NS defines the relation between pressure P, rest-mass density ρ, the internal specific energy ϵ, and the ratio between the number of electrons and the number of baryons, the electron fraction Y_e, $\text{P} = \text{P}(\rho,\epsilon,Y_e)$. For cold NSs, the electron fraction is determined by the beta-equilibrium condition, and depends on the rest mass density. Temperature and specific energy are considered negligible, making pressure dependent only on rest-mass density. The EoS is uncertain above the nuclear saturation density ρ_{sat} because of many challenges in treating the nuclear many-body problem [2, 5, 6]. The nuclear EoS can be calculated starting with two-, three-, and many-body interactions. These interactions contain free parameters, which need to be constrained by experiments. Heavy-ion collisions add constraints for densities up to 5 ρ_{sat} but only for hot, nearly isospin-symmetric nuclear matter [2, 7]. In contrast, NS matter is cold and very neutron rich. Therefore, a non-trivial extrapolation is required from hot symmetric matter to cold neutron-rich matter to constrain the NS EoS. For densities up to 2 ρ_{sat} and temperatures ≤ 30 MeV pure neutron matter is well constrained by theoretical calculations using Chiral

Effective Field Theory [8–12]. At very high densities around 40 ρ_{sat} matter is described accurately by perturbative quantum chromodynamics (pQCD) [13, 14], however, this is a regime highly above the expected maximum densities in NSs ($\sim 10\ \rho_{\text{sat}}$). Since there is still a wide density range, where the EoS is still unknown, many different EoS models are proposed, using observational constraints and different microphysical approaches.

Internal Structure

The mass-radius relation of NSs is uniquely determined by the EoS. For a static NS the equations for relativistic hydrostatic equilibrium, called the Tolman-Oppenheimer-Volkoff (TOV) equations [15, 16] yield the relations between mass, radius, pressure and central density. The resulting internal structure of NSs can be divided into five regions: atmosphere, envelope, crust, outer core, and inner core [2, 17]. The atmosphere and envelope are extremely thin layers that only contain an insignificant amount of mass and can consist of a range of light nuclei (for example H, He, C, O) and heavier nuclei such as iron [17]. With increasing depth, the rest-mass density increases, and the nuclei become more neutron-rich. Within the crust the neutron drip density ($\rho > 4 \times 10^{11}$ g cm^{-3}) is reached, where the neutrons start to be unbound from the nuclei [18]. At densities between 1/4 and 1/2 of ρ_{sat}, the nuclei deform and form a so-called nuclear pasta phase [19]. At the boundary of the outer core a phase transition occurs to homogeneous nuclear matter. The composition of the inner core is not yet known. It is possible that homogeneous nuclear matter persists until the center. There could also be another phase transition to more exotic matter states consisting of hyperons, pions or kaons coexisting with nucleons or deconfined quark matter in a pure state or mixed with hadrons.

Binary neutron star merger

Binary neutron star (BNS) systems consist of two neutron stars orbiting each other. Over time, the binary loses energy and angular momentum due to the emission of gravitational waves (GWs). The GW signal becomes stronger as their orbits shrink and their orbital velocity increases. The signal amplitude is approximately given by the second time derivative of the mass quadrupole moment of the source [20]. The frequency increase over time and the signal is dependent on the chirp mass

$$\mathcal{M} = \frac{(m_1 m_2)^{3/5}}{(m_1 + m_2)^{1/5}} \tag{1.1}$$

of the system, where m_1 and m_2 are the masses of the binary components [21, 22]. At the end of this inspiral phase, both NSs reach relativistic orbital velocities and the gravitational forces are so immense that both NSs deform before they merge. These tidal effects are described by the tidal deformability [23–26]

$$\Lambda = \frac{2}{3} k_2 \left(\frac{R}{M} \right)^5 , \tag{1.2}$$

in which k_2 is the tidal Love number [27] and these are uniquely determined by the EoS. The inspiral phase can thereby provide invaluable information about the underlying EoS. The merging phase occurs on a time scale of milliseconds [3]. If the total mass of the system is below the threshold mass M_{thresh} for a prompt collapse to a BH [28–30] the merging NSs form a rapidly differential rotating hot NS [31–36]. The total mass of the remnant can exceed the maximum mass of a non-rotating NS, since it is supported against gravitational collapse by rapid differential rotation and thermal pressure. The remnant is severely deformed, non-axisymmetric, and features different fluid oscillations [26, 33, 37, 38]. These oscillation modes also emit GWs. While the inspiral probe the cold EoS, the post-merger GW signal can provide important information about the EoS at finite Temperatures. The dominant frequency feature, f_{peak}, is correlated with the quadrupole oscillation mode [25, 26, 32, 33, 37, 39–51].

During the merger, tidal arms are forming which expel neutron-rich matter. At the interface of the two NSs materials is squeezed out by shock-induced heating. Matter that becomes unbound on the merger-timescale is called dynamical ejecta. Some debris of the merger does not immediately become unbound and forms an accretion disc around the central object. Spiral density waves, which are excited in the disc by the oscillations of the remnant, lead to outward angular moment transport and further mass ejection.

From the hot and dense remnant and disc, a high amount of neutrinos are emitted. These neutrinos interact with matter and can transport energy and momentum, which lead to outflows called neutrino driven wind. Over time, the central object-torus system will continue to eject mass by different mechanisms such as viscous energy dissipation and turbulent angular momentum transport, magnetic pressure, nucleon-recombination heating, and neutrino energy deposition [52–61].

R-process nucleosynthesis

In conditions in which the neutron density is high ($n_N > 10^{20}$ cm^{-3}) and the timescale for neutron capture onto seed nuclei is shorter than the β-decay timescale, elements heavier than iron can be synthesized via the rapid neutron-capture process, called r-process [35, 62–67]. The seed nuclei shift away from the valley of stability of the nuclear chart through repeated neutron captures and reach neutron-rich isotopes, which are highly unstable. The maximum limit that nuclei can reach is the 'neutron drip line,' beyond which further neutron capture becomes impossible. The equilibrium between neutron captures and photodisintegration determine the r-process path and the abundance ratios of the neutron-rich nuclei. Over time, nuclei will climb up the nuclear chart towards higher charge numbers Z through repeated neutron captures and β^--decays. Along this r-process path the seed nuclei will traverse the lines of closed neutron shells (magic numbers N= 82, 126, 196). The nuclei with a closed neutron shell are comparatively more stable. The neutron separation energy is especially low just past a neutron magic number, which makes these nuclei more vulnerable to photodisintegration. This hinders the flow to more neutron-rich species and the path mainly driven by β-decay goes towards stability until the neutron separation energies become larger again. As a consequence, part of the material accumulates at the neutron magic numbers. Under the right conditions, the nuclear flow towards high Z can reach the transactinides region where nuclear fission occurs. The fission products can then start the cycle from the low point toward the high Z. Eventually, the free neutron to seed ratio declines and the neutron captures will freeze out. The neutron-rich matter will approach the valley of stability again through β-decay, α-decay and fission channels. The abundance distribution has imprints of the accumulation at the closed neutron-shells approximately at mass numbers A= 80, A= 130 and A = 195 (first, second and third r-process peak). Burbidge et al and Cameron realized already in the 1950's that roughly half of the elements heavier than iron in the universe must be created by this process [68, 69]. But still to this day, the astrophysical sites where the r-process occurs remain uncertain. One of the most critical quantity to indicate viability of a potential r-process event is the electron fraction Y_e [70–72]. Binary neutron star merger (BNSM) are so far the only confirmed site for r-process nucleosynthesis with their neutron-rich ejecta. Numerical simulations with detailed nuclear network calculations [73, 74] show that elements of the second an third r-process peak ($A \gtrsim 120$) are produced for ejecta with $Y_e \leq 0.2$, with the synthesis of lighter r-process elements strongly suppressed. Whereas, for ejecta with $Y_e \geq 0.25$ only the lighter r-process elements are produced. The different ejecta components of BNSM leads to a wide range of Y_e ($\sim$ 0.05-0.5). Which is an ideal condition for the synthesis of a wide range of elements.

Electromagnetic transient - Kilonova

The radioactive ejecta made up of different newly synthesized elements power an electromagnetic transient, analogous to the transient of supernovae powered by the decay of ^{56}Ni [75, 76]. The emitted electrons through β-decay and accompanied γ-ray emission are the dominant heating source of the material. Decay channels, such as α-decay and fission, also contribute to heating, with the extent depending greatly on the quantity of heavier elements produced. Unlike in supernovae, there are various radioactive decays with varying half-lives across different timescales involved. The combination of different exponential decays lead to a power law decay $\sim t^{\alpha}$, with $\alpha \approx 1.1 - 1.4$ [36, 74, 77, 78]. The peak luminosity is approximately one thousand times brighter than a nova, therefore, called a kilonova[1] [77]. For determining the light curves and spectra of kilonovae, the thermalization efficiency and atomic opacities play an essential role. Most of the energy from the r-process is released on a time scale of seconds [65, 80, 81]. However, a lot of this initial heating is lost to adiabatic expansion since the ejecta is extremely optically thick at early times and radiation can only escape from the outer layers. During expansion, the density decreases and at some point the optical depth becomes small enough so that most of the ejecta becomes optically transparent [35]. Significant electromagnetic luminosity is possible as soon as photons can escape the ejecta on the expansion time scale. The transition from opaque to transparent depends greatly on the opacity of the material. Especially heavy elements with open atomic f-shells (lanthanides and actinides) have a

---

[1] Kulkarni introduced the term 'macronova' which also many authors use today in part because it is not tied to particular luminosity scale [79]

high number of low-energy excitation levels that highly enhance the number of transition lines in the optical and infrared bands [3, 82, 83]. This leads to the effect that more lanthanide-rich ejecta reach their peak luminosity later and at longer wavelength with the same mass and velocity. The lanthanide and actinide opacities are still uncertain because the atomic states and line strength of many heavy elements are not measured experimentally. [67] The Y_e distribution of the ejecta is essential for radiation transfer calculations and determining the abundance pattern. Similarly, the total mass, mass distribution, and velocity distribution are crucial for predicting the resulting light curve. Achieving a comprehensive understanding of the underlying physics requires both observations and numerical modeling of these events.

1.2. Observations

In 2017, a BNSM was detected through GWs for the first time [84]. The detection, named GW170817, measured the late inspiral phase, while no GW signal from the post-merger phase could be found, since this was beyond the sensitivity of the detectors at that time [85, 86]. In addition to the GW signal, an electromagnetic counterpart was detected in different frequency bands, from radio up to gamma-ray emission [87]. First, about 1.7 s after the merging time, a gamma-ray burst was detected [87–90]. Then about eleven hours after the GW detection an optical counterpart was found, which led to the identification of the host galaxy NGC 4993 at a distance of around 40 Mpc [87, 91–93]. From there, over the next 30 days the evolution of the ultra-violet, optical and infra-red components were followed (e.g. [87, 94]). In addition, after 9 and 16 days after the merger, X-ray and radio emission were also found, respectively [87, 95–97].

The analysis of the GW signal from the inspiral phase provided constraints of the tidal deformability and the radius of static NSs and, therefore, on the EoS [84, 98, 99]. In addition to the GW detection, the analysis of the multi-messenger observation from several groups has resulted in numerous constraints on the stellar properties of NSs and on the EoS (e.g. [98–107]). These results of a single event show the importance of BNSMs when it comes to determining the high density EoS. Furthermore, the observed light curves in the ultraviolet, optical and infrared bands provide strong evidence that r-process elements are synthesized through the r-process in the ejecta of BNSMs [87, 108–110]. The estimated r-process nucleosynthesis yields are consistent with the idea that BNSM are the dominant source, given the large uncertainties in BNSM rates [94]. Gamma ray detection supports the theoretical work which suggests BNSM as possible sources for short gamma-ray bursts [64, 111, 112]. The detected gamma-ray burst is compared to typical observed short gamma-ray bursts quite different in spectral evolution and luminosity [87, 113, 114]. This can be partly explained by the fact that the viewing angle was off-axis with an estimated viewing angle about 30° [115]. However, the interpretation of the gamma-ray, X-ray and radio observations and the underlying mechanism that leads to the emission are not yet fully understood (e.g. [113–116]).

In 2019 GW190425, a GW signal from the inspiral of another event, were detected [117]. The analysis of the signal identified it as a possible BNSM. An interesting feature of the system is the total mass of about 3.4 $M_\odot$, which is significantly higher compared to other known BNSs [117, 118]. Because the detected signal had a low signal-to-noise ratio and some of the detectors where at that time offline, GW190425 was a single-detector event. Therefore, the analysis of the signal did not provide additional constraints on the tidal deformability, radii, or EoS of NSs [117]. Furthermore, despite thorough search, no electromagnetic counterpart was found [117, 119]. The Advanced LIGO [120], Advanced Virgo [121], and KAGRA [122] GW detectors currently are in the fourth observation run until October 2025 [123]. Furthermore, an additional detector (LIGO-India [124]) is planned, which should further increase the detection rates and sky localization accuracy [125–127]. Moreover, next-generation detectors such as the Cosmic Explorer [128] and the Einstein Telescope [129] are planned with design sensitivities roughly an order of magnitude higher than from the current detectors.

All these extensive efforts to enhance the detection capabilities of GWs and increase the likelihood of observing more BNSM events underscore the need to dedicate similar efforts to advance our theoretical understanding of these events. Numerical modeling of the different phases of these systems is the only way to approach this. Especially hydrodynamical simulations of the post-merger phase are important to understand their dynamics, and will help to interpret potential future post-merger GW signals. Moreover, these simulations are essential to determine the properties of ejecta such as amount, distribution, composition, velocity, and entropy, which are necessary as initial data for realistic r-process calculations and future kilonovae analysis. Ideally, improving numerical simulations together with detailed investigations of their results will lead to a better understanding of BNSMs and help interpret future observations. This thesis tries to contribute to that goal.

1.3. Numerical modeling

Numerical simulations of BNSM have to take into account several physical aspects for an accurate representation of the event. The system requires the treatment of general relativistic hydrodynamics as well as a dynamical spacetime. For the merging phase, the formation of shocks and fluid instabilities is important, especially at the collision interface. During that phase, matter can reach temperatures of several tens of MeV. Therefore, the microphysical description of NS matter needs a fully consistent treatment of thermal effects. At this point, weak interaction and neutrino radiation also becomes important. The neutrinos interact with free nucleons and changing for a significant amount of the ejecta the composition. To be able to determine the abundance of elements synthesized by r-process nucleosynthesis, neutrino-matter interactions need to be properly taken into account during the BNSM. For the post-merger phase, it is crucial that the outflowing matter, which moves with high velocities over large distances, is resolved with high precision. For accurate calculations of the nucleosynthesis and radiation transfer, this is needed for timescales that are significantly longer than the merger time scale. While the matter expands, already within the first second the density can change up to 20 orders of magnitude. Also, the temperature will cool down several orders of magnitude during that time. To accurately describe matter over this time scale, the chosen EoS must encompass a wide range of parameter space. Section (2.3.1) presents how we approach this in this work.

Another difficulty to tackle, linked to the longer time scale, is the resolution of the ejecta moving over the vast distances. How to deal with this depends on the model one chooses to treat relativistic hydrodynamics. The two most common approaches to simulate the system are Eulerian grid-based code methods and Lagrangian smoothed particle hydrodynamics (SPH) (for details see e.g. 2.2 and [3, 130–136]). The main difference is that Eulerian approaches focus on fixed points in space through which a fluid flows while Lagrangian approaches follow fluid elements as they move through space and time. In this work, we will use SPH.

SPH discretizes the general relativistic hydrodynamic (GRHD) equations on a set of particles. The particles follow the fluid motion, which makes tracing the ejecta straightforward. The particle positions are not limited by a predefined grid. Also, no effort is needed for the treatment of vacuum, which translates just to an absence of particles, unlike in grid-based methods. The particles interact with their neighbors within a specific range, called the smoothing length (see 2.2). Because of this smoothing approximation, the accuracy of the discretization depends on two aspects: The number of neighbor particles and the scale of the smoothing length. Typically, one of this two aspects is regulated within the simulation. In our case we only allow a specific range of number of neighbors. The resolution of an simulation depends on the number of particles. A region is not well resolved if there are not many particles distributed, which results in increased smoothing lengths to find enough neighbor particles. This is especially for the expanding ejecta a challenge. Poor resolution leads to a low accuracy of the discretization of the GRHD equations and can result in nonphysical solutions, such as negative internal energy. There is no unique way to discretize the GRHD equations in SPH and different approaches differ in stability and accuracy under low resolution. We implement a discretization based on the work in [137] an show that it increase stability under low resolution and discuss the impact on the ejecta evolution (see Sect. 4.2).

The improvement of the ejecta evolution helps to reach longer time scales in the simulation, however increasing also the resolution is necessary. While increasing the total number of SPH particles might seem as a trivial solution to do that, including various different physical aspects (e.g. neutrino treatment, viscosity, magnetic fields) in the model with high resolution can make simulations of these systems very computationally demanding[2]. Therefore, an efficient way to tackle this challenge is to increase the resolution only in the regions of interest and not in the whole simulation. We present one approach to achieve this in Sec. 6.

---

[2] e.g. Kiuchi et al. [138] needed 85 million CPU hours for a grid-based magneto-hydrodynamic simulation of a BNSM to evolve for one second.

To calculate the nucleosynthesis yields and the resulting kilonova light curve for a given total ejecta mass and distribution, radiative transfer models are necessary. They describe how radiation interacts with matter as it propagates through a medium. In the case of kilonovae nuclear network calculations are necessary within this framework to know the abundances of the r-process elements, which is essential to estimate the opacity of the matter and how much radiation gets emitted by radioactive decay. Radiative transfer models for kilonovae assume as a initial conditions that the matter is in homologous expansion (the relative velocity between the mass elements is constant). This is a useful assumption, since it untangles hydrodynamics from radiative transfer and allows these models to focus solely on the latter. A key objective for hydrodynamic simulations is thus to attain this phase, where the ejecta is homologous expanding. We present in this work a long-term BNSM simulation and estimate how much ejected matter reach homologous expansion within the simulated time (see Sec. 5).

While improvements and further progress to longer and more precise numerical simulations is crucial, one also need to be aware of its limitations, especially when it comes to interpreting simulation results. Different studies showed that so far no BNSM simulation are fully converged, meaning that the results depend on the resolution [25, 30, 139–142]. A typical trend which is discussed in this regard is, that the resulting ejecta mass increases with higher resolution. However, Collins et al. [143] found that beside the dependence on resolution their simulations showed general fluctuations of their ejecta mass and ejecta distribution. It is not clear if these fluctuations are purely numerical or have a physical root. Merger events are very dynamical and turbulent, and it could very well be the case that already small seed perturbations lead to different outcomes. These small differences would be impossible to observe, and the variation of the outcome for the same observable parameter could be described as stochastic effects. So far, this stochastic effects in BNSM has not been investigated. This thesis is the first study, which investigates this problem (see Sec. 3). It is possible that cause of fluctuations in the results of simulations is just numerical, and it is very challenging to get conclusive answers for that problem. However, even if this is the case, to address these fluctuations, when interpreting simulations results, is important. The before mentioned studies which reported increasing amount of ejecta with higher resolution, for example, did not test how much the amount ejecta fluctuate for different simulation with the same resolution. Even if these fluctuations have a numerical root one needs to take them into account when drawing conclusions from simulations. And the extent to which the amount of ejected material depends on the resolution may have been overestimated in these studies.

1.4. Goals and outline

In this section, we summarize the main goals and provide an outline of this thesis. This work primarily addresses the challenges associated with simulating BNSM ejecta and attempts to advance the capabilities of these numerical simulations.

One part of this thesis examines the question if variations in BNSM simulations are resolving physical stochastic fluctuations of the system or have a numerical root. These fluctuations are a crucial factor that should be considered in the evaluation of simulation results, yet they have not been taken into account or investigated so far. We note that this study does not aim to be entirely conclusive due to inherent challenges posed by the limitations of numerical simulations and the scarcity of prior research on this subject. Nonetheless, it offers the first insightful information regarding the fluctuations.

The next part of this thesis focuses on improving the simulation setup. First, we extend the employed EoS towards lower rest-mass densities and temperatures. We investigate the energy evolution of ejected matter and adjust the energy equation discretization to enhance robustness against low-resolution artifacts. Total mass, temperatures and velocity distribution of the ejecta are still not well constrained, which are important information for kilonova calculation. Our adjustments are important advancing simulations to higher validity, which essential to achieve better constraints. The adjustments allow for simulating BNSM for a longer time, which is a vital point for more realistic kilonova studies. We present results from a long-term BNSM simulation and discuss how much material reached homologous expansion within the simulated time.

In the last part we test particle splitting as a method in SPH to efficiently increase the resolution of the ejecta in BNSM simulations, which is used in this context for the first time. We introduce our splitting method and assess various splitting criteria to identify the one that most efficiently achieves higher resolution of ejecta. A comparative resolution study has been conducted to analyze simulations with and without particle splitting, based on which the improvements are discussed.

Since this thesis focuses more on the technical aspects of simulating BNSM we decided to simulate for each part the same physical event. All models simulate a 1.35-1.35 $M_\odot$ equal mass merger with SFHO as the used EoS [144]. This was essential for the investigation of stochastic fluctuations; maintaining this approach in other sections assisted in accounting for fluctuations, particularly in the context of the resolution study trends.

The outline of this thesis is the following:

In Chapter 2, the foundational physical model and computational methods for BNSMs simulations are detailed. Chapter 3 discusses the impact of stochastic fluctuations on the numerical results of the simulations and addresses potential numerical and physical origins. Chapter 4 shows the improvements of the numerical setup to run long-term simulations and compares the impact of these adjustments under varying the resolution. In chapter 5, we introduce a BNSM long-term simulation and examine the amount of material achieving homologous expansion during the simulation period. Chapter 6 describes particle splitting as an efficient technique for enhancing resolution. We compare simulations with and without particles splitting and discuss the improvements. Finally, in chapter 7 we summarize results, draw conclusions, and discuss some directions for future work. In Appendix A, we show a detailed derivation of the employed GRHD equations in the co-moving frame. Appendix B discusses the impact of using different ejecta criteria.

Appendix C investigates the impact of dissipation in the employed artificial viscosity scheme on the evolution of BNSM.

1.5. Conventions and notations

Unless otherwise stated, we employ a dimensionless system of units for which $c = G = M_\odot = 1$. Throughout this work Latin indices run from 1 to 3 and Greek indices from 0 to 3. Einstein's summation convention is used, which means, unless stated otherwise, that repeated indices are summed over all possible values. The differential operators Δ and ∂_i are with respect to the flat three metric. The metric signature used is $(-,+,+,+)$. The GW signal is described by two polarizations states h_+ and $h_\times$, which are which are equivalent in their informational value. For the analysis of GW spectra, we use the effective spectrum $h_{\text{eff},+}$, which is defined as $h_{\text{eff},+}(f) = f \cdot \tilde{h}_{\text{eff},+}(f)$, where $\tilde{h}_{\text{eff},+}(f)$ is the Fourier transformation of the strain $h_+(t)$ and f the frequency.

2. Theoretical formulation and numerical implementation

This chapter gives an overview of the methods and their numerical implementation for relativistic hydrodynamical simulations. Section 2.1 focuses on the theoretical background, Section 2.2 presents the computational method SPH we employ, and 2.3 will describe specific numerical implementations of our simulation code.

2.1. Numerical Relativistic Hydrodynamics

Numerical models of BNSMs require the treatment of GRHDs and the dynamics of spacetime. Therefore, it is necessary to solve the equations

$$G_{\mu\nu} = 8\pi T_{\mu\nu} \tag{2.1}$$

$$\nabla_\mu (n u^\mu) = 0 \tag{2.2}$$

$$\nabla_\mu T^{\mu\nu} = 0, \tag{2.3}$$

where $G_{\mu\nu}$ is the Einstein tensor, $T^{\mu\nu}$ the energy-momentum tensor, n the number density, and u^μ is the four-velocity. Equation 2.1 is the Einstein field equation that relates the spacetime geometry with the mass and energy within it. Equations 2.2 and 2.3 are the relativistic Euler equations which describe the motion of a perfect fluid in a given spacetime by the conversation of the number of particles, energy and momentum. In general, the combined system of the Einstein field equation and the relativistic hydrodynamic equations is too complex to solve analytically. Consequently, numerical approaches are so far the only way to describe such systems. In order to study the evolution of any physical system, the first step is to formulate it as a Cauchy problem. To do that for spacetime, one assumes that it is globally hyperbolic [132]. Any globally hyperbolic spacetime can be sliced in space-like three-dimensional cuts and a universal time function.

We consider the Arnowitt-Deser-Misner (ADM) 3+1 decomposition [145] that foliates the spacetime into such a set of non-intersecting hypersurfaces Σ_t with a constant coordinate time. The system is described by a timelike four-vector $\mathbf{n}$ normal to the hypersurface, the lapse function α which measures the lapse of proper time between two hypersurfaces, and the shift vector β whose components measure the change of spatial coordinates from one hypersurface to the next.

With that the line element in the ADM formulation is

$$ds^2 = -\left(\alpha^2 - \beta_i\beta^i\right)dt^2 + 2\beta_i dx^i dt + \gamma_{ij}dx^i dx^j, \tag{2.4}$$

with γ_{ij} as the spacetime 3-metric. For the perfect fluid the energy-momentum tensor can be described by

$$T^{\mu\nu} = \rho h u^\mu u^\nu + P g^{\mu\nu}, \tag{2.5}$$

where $g^{\mu\nu}$ is the metric tensor, ρ is the rest-mass density, $h = 1 + \epsilon + P/\rho$ is the specific enthalpy, ϵ the specific internal energy, P is the pressure and u^μ is the 4-velocity of the fluid. The EoS of the fluid brings the pressure in relation to the density and the specific internal energy. With that, a complete hydrodynamic description can be made with a set of 6 primitive variables $\mathbf{W} = (\rho, \bar{v}^i, \epsilon)$, where $\bar{v}^i$ is the fluid 3-velocity. In the ADM decomposition it is possible to cast the conservation laws of the energy-momentum tensor and the matter flux into a system of first-order flux-conservative hyperbolic differential equations, which is called the Valencia formulation [131, 146]. In this formulation the GRHD equations are written in the conservative form

$$\partial_0\left(\sqrt{\gamma}\mathbf{U}\right) + \partial_i\left(\sqrt{\gamma}\mathbf{F}^i\right) = \mathbf{S}, \tag{2.6}$$

where **U** is the set of appropriate chosen variables[1], **F** is the flux of the variables and **S** is the source vector. Here, ∂_0 and ∂_i are the partial derivatives with respect to the chosen local coordinates $x^\mu = \left(x^0, x^1, x^2, x^3\right)$. This formulation offers the advantage that it allows for the use of many high-resolution shock-capturing schemes, initially developed for Newtonian hydrodynamics, to now also be utilized for general relativistic problems. For SPH these GRHD equations need to be formulated in the co-moving frame of the fluid. We will show this in section 2.2, where we talk more in detail about SPH.

2.1.1. Conformal flatness approximation

In addition to the Arnowitt-Deser-Misner (ADM) formalism we employ the conformal flatness condition (CFC) approach [147, 148], which approximates the spatial $3-$metric as

$$\gamma_{ij} = \psi^4\eta_{ij} \tag{2.7}$$

where η_{ij} is the flat spatial metric. In isotropic Cartesian coordinates, this leads to $\eta_{ij} = \delta_{ij}$. Imposing the maximal slicing condition $\mathrm{tr}(K_{ij}) = \partial_0 K = K^i_i = 0$, the Einstein equations can be written in a set of five elliptic equations for the metric elements (e.g.[146, 147, 149]):

$$\Delta\left(\alpha\psi\right) = 2\pi\alpha\psi^5\left(E + 2S\right) + \frac{7}{8}\alpha\psi^5 K_{ij}K^{ij}, \tag{2.8}$$

$$\Delta\psi = -2\pi\psi^5 E - \frac{1}{8}\psi^5 K_{ij}K^{ij}, \tag{2.9}$$

---

[1] Also called
conserved variables due to the structure of (2.6), which has the form of the continuity equation.

$$\Delta\beta^i = -\frac{1}{3}\partial^i\partial_j\beta^j + 2\psi^{10}K^{ij}\partial_j\left(\frac{\alpha}{\psi^6}\right) + 16\pi\psi^4 S^i, \tag{2.10}$$

in which

$$E = \rho h W^2 P, \tag{2.11}$$

$$S = S_i^i = \rho h\left(W^2 - 1\right) + 3p \tag{2.12}$$

are matter contributions to the source terms, W is the Lorentz Factor $W = \alpha u^0 = \left(1 + \gamma^{ij}u_i u_j\right)^{1/2}$ and $\Delta = \nabla^2$ is the flat-space Laplacian. In the conformal flatness - maximal slicing approximation, the extrinsic curvature can be expressed just with the metric elements

$$K_{ij} = \frac{\psi^4}{2\alpha}\left(\delta_{ik}\partial_j\beta^k + \delta_{jk}\partial_i\beta^k - \frac{2}{3}\delta_{ij}\partial_k\beta^k\right). \tag{2.13}$$

The equation for the shift vector β^i can be cast into the more convenient form of two Poisson-like differential equations [150] by the definition

$$\beta^i = B^i - \frac{1}{4}\partial_i\chi. \tag{2.14}$$

Inserting this definition into equation (2.10) leads to the differential equation for B^i and χ

$$\Delta B^i = 2\psi^{10}K^{ij}\partial_j\left(\frac{\alpha}{\psi^6}\right) + 16\pi\alpha\psi^4 S^i, \tag{2.15}$$

$$\Delta\chi = \partial_i B^i. \tag{2.16}$$

These equations are discretized on a uniform Cartesian grid covering a domain around the binary system and are solved iteratively until they converge using a multigrid approach [151]. A multipole expansion of the source terms (2.9) and (2.8) in spherical harmonics up to the quadrupole order provides boundary conditions [130]. This expansion scheme is also used to estimate values of the metric components outside the metric grid for the cases where particles exit the domain of the metric solver.

The CFC approximation ignores off-diagonal spatial metric terms and therefore excludes the degrees of freedom for gravitational waves. To take gravitational waves and their back-reaction to matter into account, a small non-conformally flat correction is implemented. This scheme was developed in [152], while first elements of the scheme can be found in [153]. This approach allows post-merger gravitational wave signals, ejecta and torus masses, and black hole formations, which are in accordance with full general relativistic simulations of BNS systems [28, 30, 44, 154]. More details of this metric solver scheme can be found in [42].

2.2. Smoothed particle hydrodynamics

Gingold, Monagham, and Lucy introduced SPH as an alternative to Eulerian finite difference methods for hydrodynamical problems [155, 156]. An essential part of SPH is the interpolation method. The sifting property of the Dirac delta distribution has the ability to give, for a function $f(\mathbf{r}')$ which is continuous at the point $\mathbf{r}$, the exact value at that point with

$$f(\mathbf{r}) = \int f\left(\mathbf{r}'\right) \delta\left(\mathbf{r} - \mathbf{r}'\right) \mathbf{dr}'. \tag{2.17}$$

SPH using an approximation of this property with a Kernel function $W(\mathbf{r} - \mathbf{r}', h_s)$ which becomes a true delta distribution at the limit $h_s \to 0$, with h_s the smoothing length that defines the integration domain. The interpolation is with that expressed as

$$f(\mathbf{r}) = \int f\left(\mathbf{r}'\right) \mathcal{W}\left(\mathbf{r} - \mathbf{r}', h_s\right) \mathbf{dr}'. \tag{2.18}$$

Conservation of total mass in the complete system volume V is achieved by the normalization condition on the kernel $\mathcal{W}$

$$\int \mathcal{W}\left(\mathbf{r} - \mathbf{r}_b, h_s\right) dV = 1. \tag{2.19}$$

In this work we use the spherical symmetrical cubic spline kernel

$$\mathcal{W}\left(\mathbf{r} - \mathbf{r}', h_s\right) = \frac{1}{\pi h_s^3} \begin{cases} 1 - \frac{3}{2}d^2 + \frac{3}{4}d^3, & \text{for } 0 \leq d \leq 1 \\ \frac{1}{4}\left(2 - d\right)^3, & \text{for } 1 < d \leq 2 \\ 0, & \text{for d} > 2 \end{cases} \tag{2.20}$$

with $d = \frac{|\mathbf{r} - \mathbf{r}'|}{h_s}$.

To apply this interpolation to a fluid, it is divided into a set of mass elements, called particles. Particle a is given the mass M_a, density ρ_a and so on. The interpolation integral $\int f\left(\mathbf{r}'\right) \mathbf{dr}'$ can be written as

$$\int \frac{f\left(\mathbf{r}'\right)}{\rho(\mathbf{r}')} \rho(\mathbf{r}') \mathbf{dr}'. \tag{2.21}$$

This integral can be approximated by a summation over all particles b which overlap with point $\mathbf{r}$.

$$f(\mathbf{r}) \approx \sum_b \frac{M_b}{\rho_b} f(\mathbf{r}_b)\, \mathcal{W}\left(\mathbf{r} - \mathbf{r}_b, h_s\right). \tag{2.22}$$

The calculation of any quantity at any point follows from Eq.(2.22). If a particle overlaps with the point of interest depends on its smoothing length which evolves based on the local particle number density. Mass density can then expressed by

$$\rho(\mathbf{r}) = \sum_b M_b\, \mathcal{W}\left(\mathbf{r} - \mathbf{r}_b, h_s\right). \tag{2.23}$$

Two kind of errors can be attributed to this procedure. First, an error stemming from the smoothing procedure. This has been estimated to be $\mathcal{O}(h^2)$, when using the cubic spline kernel. [157–160]. Second, an error from discretizing the integral, which depends on the distribution of particles and how well ordered they are in space. Zhu et al. [157]

parameterized this error on the number of neighbor particles N_b to be $\mathcal{O}(N_b^g)$, where 0.5 $< g < 1$. $g = 1$ is the extreme case where all particles are perfectly ordered and spaced out like a grid, and $g = 0.5$ is the opposite extreme, where we assume the particle distribution is completely random and convergence should be similar as in Monte Carlo estimates as SPH was originally assumed [155, 156]. In reality, the SPH particles are neither equally spaced nor randomly distributed but are distributed by the dynamics of the systems they describe. However, in highly turbulent and complicated dynamical problems such as BNSM, disorder is to be expected. At low resolution, errors will vary based on the decision to hold either the smoothing length or the number of neighbors constant. Keeping the smoothing length fixed at low resolution will decrease the number of neighbors, thereby raising the discretization error. Conversely, fixing the number of neighbors leads to an increase in the smoothing length, consequently elevating the smoothing error. In our setup we allow a range between 80 and 120 neighbor particles, while the smoothing length evolves accordingly.

In this Lagrangian descriptions of SPH it is possible to formulate the GRHD equations in a co-moving frame (for a detailed derivation, see Appendix A). Analog to the Valencia formulation one defines a set of so-called conserved variables: the rest-mass density ρ^*, the specific momentum $\hat{u}$ and the energy per nucleon τ, which are defined by

$$\rho^* = \rho W \psi^6 \tag{2.24}$$

$$\hat{u}_i = h u_i = h\left(v^i + \beta^i\right)\psi^4 u^0 \tag{2.25}$$

$$\tau = hW - \frac{P}{\rho W} - \sqrt{1 + \frac{\hat{u}_i \hat{u}_j \delta^{ij}}{\psi^4}} = hW - \frac{P}{\rho W} - \omega, \tag{2.26}$$

with $v^i = \frac{u^i}{u^0}$ the coordinate velocity. In the comoving frame the time derivative operator $\frac{d}{dt}$ is related to the Eulerian time derivative ∂_0 by $\frac{d}{dt} = \partial_0 + v^i \partial_i$. Accordingly the set of GRHD equations are

$$\frac{d\rho^*}{dt} = -\rho^* \partial_i v^i, \tag{2.27}$$

$$\frac{d\hat{u}_i}{dt} = -\frac{1}{\rho^*}\alpha\psi^6 \partial_i P - \alpha \hat{u}^0 \partial_i \alpha + \hat{u}_j \partial_i \beta^j + \frac{2\hat{u}_j \hat{u}_j}{\psi^5 \hat{u}^0}\partial_i \psi, \tag{2.28}$$

$$\begin{aligned}\frac{d\tau}{dt} = &-\frac{\psi^6}{\rho^*}\left(v^i + \beta^i\right)\left(1 - \frac{hW}{\omega}\right)\partial_i P - \psi^6 \frac{P}{\rho^*}\partial_i\left(v^i + \beta^i\right) \\ &- 6\psi^5 \frac{P}{\rho^*}\left(v^i + \beta^i\right)\partial_i \psi - \frac{\hat{u}_i}{\psi^4}\left(1 - \frac{hW}{\omega}\right)\partial_i \alpha \\ &+ \frac{1}{\psi^4}\left(\frac{1}{hW} - \frac{1}{\omega}\right)\left(\hat{u}_i \hat{u}_j \partial_j \beta^i - \frac{1}{3}\hat{u}_i \hat{u}_i \partial_j \beta^j\right).\end{aligned} \tag{2.29}$$

2.2.1. Discretization

Besides Eq. (2.22) to describe functions at any point, it is also important how differentiation and differential equations are described in SPH. By using differentiable Kernels we can express derivatives with

$$\frac{\partial f(\mathbf{r})}{\partial x} = \sum_b \frac{M_b}{\rho_b^*} f(\mathbf{r}_b) \frac{\partial \mathcal{W}(\mathbf{r} - \mathbf{r}_b, h_s)}{\partial x}, \tag{2.30}$$

which is the exact derivative of the approximate function. Note also that in the relativistic case the conserved mass density ρ^* is used. The form 2.30 however has the problem that it does not necessarily vanish if $f(\mathbf{r})$ is constant. To ensure that one can write the derivative as

$$\frac{\partial f(\mathbf{r})}{\partial x} = \frac{1}{\Phi}\left(\frac{\partial(\Phi f(\mathbf{r}))}{\partial x} - f(\mathbf{r})\frac{\partial \Phi}{\partial x}\right), \tag{2.31}$$

where Φ is any differentiable function. A common choice for Φ is, for example, the density ρ^*. With that we can write Eq. (2.30) for a particle a as

$$\frac{\partial f(\mathbf{r}_a)}{\partial x} = \frac{1}{\rho_a^*}\sum_b M_b(f(\mathbf{r}_b) - f(\mathbf{r}_a))\frac{\partial \mathcal{W}(\mathbf{r}_a - \mathbf{r}_b, h_s)}{\partial x} = \frac{1}{\rho_a^*}\sum_b M_b f_{ba}\frac{\partial \mathcal{W}_{ab}}{\partial x}. \tag{2.32}$$

This makes it possible to describe the same continuous equations with different discretizations to improve evolution, conservation laws, or minimize numerical noise. The choice of discretization can have a major impact on the evolution of the system. Here we take a closer look at the first two terms of Eq. (2.29) which contain the pressure gradient and the divergence of velocity, and are the part of the conserved energy which is rather related to the hydrodynamical quantities, while the other terms capture the impact of the metric parameters on τ. We will keep the notation, that we discretize for a particle a which has b neighbor particles. The pressure gradient can be discretized by setting $\Phi = \frac{1}{\rho^*}$

$$\begin{aligned}
\frac{\partial_i P}{\rho^*} &= \partial_i\left(\frac{P}{\rho^*}\right) + \frac{P}{\rho^{*2}}\partial_i \rho^* \overset{disc.}{\approx} \sum_b M_b \frac{P_b}{\rho_b^{*2}}\nabla_a \mathcal{W}_{ab} + \sum_b M_b \frac{P_a}{\rho_a^{*2}}\nabla_a \mathcal{W}_{ab} \\
&= \sum_b M_b\left(\frac{P_b}{\rho_b^{*2}} + \frac{P_a}{\rho_a^{*2}}\right)\nabla_a \mathcal{W}_{ab},
\end{aligned} \tag{2.33}$$

so we get for the first term

$$\begin{aligned}
&\frac{\psi^6}{\rho^*}\left(v^i + \beta^i\right)\left(1 - \frac{hW}{\omega}\right)\partial_i P \\
&\overset{disc.}{\approx} -\psi_a^6 \sum_b M_b\left(v_a^i + \beta_a^i\right)\left(1 - \frac{hW}{\omega}\right)\left(\frac{P_b}{\rho_b^{*2}} + \frac{P_a}{\rho_a^{*2}}\right)\nabla_a \mathcal{W}_{ab}.
\end{aligned} \tag{2.34}$$

The second term $-\psi^6 \frac{P}{\rho^*}\partial_i\left(v^i + \beta^i\right)$ can be discretized with the relation

$$\nabla \cdot \mathbf{v} = \frac{\nabla \cdot (\rho^* \mathbf{v}) - \mathbf{v} \cdot \nabla \rho^*}{\rho^*}, \tag{2.35}$$

which leads to

$$-\psi^6 \frac{P}{\rho^*}\partial_i\left(v^i+\beta^i\right) \overset{disc.}{\approx} \psi_a^6 \sum_b \frac{M_b}{\rho_a^{*2}} P_a \left[(v_a^i+\beta_a^i)-(v_b^i+\beta_b^i)\right] \nabla_a \mathcal{W}_{ab}. \tag{2.36}$$

Another possibility is to set $\Phi = \frac{P}{\rho^*}$

$$\begin{aligned}
&-\psi^6 \frac{P}{\rho^*}\partial_i\left(v^i+\beta^i\right) = -\psi^6\partial_i\left(\frac{P(v^i+\beta^i)}{\rho^*}\right) + \psi^6(v^i+\beta^i)\partial_i\left(\frac{P}{\rho^*}\right)\\
&\overset{disc.}{\approx} \psi_a^6 \sum_b \frac{M_b}{\rho_b^{*2}} P_b (v_b^i+\beta_b^i)\nabla_a\mathcal{W}_{ab} + \psi_a^6 \sum_b \frac{M_b}{\rho_b^{*2}} P_b (v_a^i+\beta_a^i)\nabla_a\mathcal{W}_{ab}\\
&= \psi_a^6 \sum_b \frac{M_b}{\rho_b^{*2}} P_b \left[(v_a^i+\beta_a^i)-(v_b^i+\beta_b^i)\right] \nabla_a \mathcal{W}_{ab}.
\end{aligned} \tag{2.37}$$

It was chosen to take the average of both discretization equations $\frac{1}{2}$((2.36) + (2.37)) which leads to

$$-\psi^6 \frac{P}{\rho^*}\partial_i\left(v^i+\beta^i\right) \overset{disc.}{\approx} \psi_a^6 \sum_b \frac{M_b}{2}\left(\frac{P_a}{\rho_a^{*2}}+\frac{P_b}{\rho_b^{*2}}\right) \left[(v_a^i+\beta_a^i)-(v_b^i+\beta_b^i)\right] \nabla_a \mathcal{W}_{ab}. \tag{2.38}$$

This is a common method for symmetrizing the discretization in SPH. In Newtonian codes, for example, it is often used to conserve momentum and energy or to enforce Newton's third law [161]. In this case it is also convenient that both terms can be merged together after discretization

$$\begin{aligned}
&-\psi^6 \frac{P}{\rho^*}\partial_i\left(v^i+\beta^i\right) + \frac{\psi^6}{\rho^*}\alpha\left(v^i+\beta^i\right)\left(1-\frac{hW}{\omega}\right)\partial_i P\\
&\overset{disc.}{\approx} -\psi_a^6 \sum_b M_b \left(\frac{P_b}{\rho_b^{*2}}+\frac{P_a}{\rho_a^{*2}}\right)\left[\left(1-\frac{hW}{\omega}-\frac{1}{2}\right)(v_a^i+\beta_a^i)+\frac{1}{2}(v_b^i+\beta_b^i)\right]\nabla_a\mathcal{W}_{ab}\\
&= -\psi_a^6 \sum_b \frac{M_b}{2}\left(\frac{P_b}{\rho_b^{*2}}+\frac{P_a}{\rho_a^{*2}}\right)\left[\left(1-\frac{2hW}{\omega}\right)(v_a^i+\beta_a^i)+(v_b^i+\beta_b^i)\right]\nabla_a\mathcal{W}_{ab}.
\end{aligned} \tag{2.39}$$

In chapter 4.2 we will discuss in more detail this approach and alternatives.

2.3. Neutron Star merger simulation

This section mainly describes the simulation code of [42, 162]. Here, the main focus will be on parts which will be relevant or modified later in this work and should only give a brief overview.

At the start of every time step, the neighbors of every SPH particle are searched with a linked-list algorithm. The algorithm uses a grid in which it lists all particles in each cell together. A particle is neighboring if it is in the vicinity of $2h_s$ to another particle. All particle outside the grid are treated as there were in a single cell together. Since most particles in a neutron star merger simulation will be in the center, the grid mainly covers the remnant (default length is 28 km in the x- and y-directions and 14 km in the z-direction).

After that, the field equations are solved and the metric components are computed following the method described in 2.1.1. The metric potentials are solved on an overlaid grid and mapped onto the SPH particles. With these can now the hydrodynamical equations be solved. The primitive hydrodynamical quantities are then computed from the conserved quantities. This can not be analytically done and involves a fixed-point iteration scheme which also involves interpolation methods for the EoS table. The time integration is done with an explicit fourth-order Runge-Kutta method. An adaptive time step is used that obeys the Courant-Friedrichs-Levi condition [163].

2.3.1. Equation of state

For the neutron star merger simulations described here, the SFHO EoS is used [144]. The SFHO EoS is organized in three parameters: baryon number density n_B, temperature T and electron fraction Y_e. The table has a minimum baryon number density of $10^{-12}\mathrm{fm}^{-3}$ and a minimum temperature of 0.1 MeV while the electron fraction ranges from 0.01 to 0.6. For each point of this 3D parameter space the table provides hydrodynamical quantities like pressure, total energy per baryon, total entropy per baryon, and several others. Since the SPH code has rest mass density ρ and internal energy ϵ as primitive variables, it is convenient to reorganize the table with only the hydrodynamic quantities needed and with the primitive variables directly accessible. To compute a rest mass density, a fixed baryon mass is assumed

$$\rho = n_B \cdot m_B, \tag{2.40}$$

where the baryon mass m_B is set to the atomic mass unit $m_u =$ 931.494 MeV. The table also gives information on the composition for each point in this 3D parameter space. For protons, neutrons, and nuclei with a mass number A ≤ 4 the number fractions

$$Y_i = \frac{n_i}{n_B} \tag{2.41}$$

is given for each species, while for heavier nuclei a number fraction for an averaged heavy nucleus is given together with the averaged mass and charge number A_{heavy}, Z_{heavy}. The total energy per baryon is defined by

$$E_{\text{tot}} = \frac{e_{\text{tot}}}{n_B} \tag{2.42}$$

with $e_{\text{tot}} = \rho(1+\epsilon)$ the total energy density.

While e_{tot} is well defined for a given composition, the separation between rest mass and ϵ depends on the choice of m_B. In figure 2.1 are the resulting internal energies for different electron fractions shown at a rest mass density of $\rho = 4.17 \times 10^8 \mathrm{gcm}^{-3}$. At low

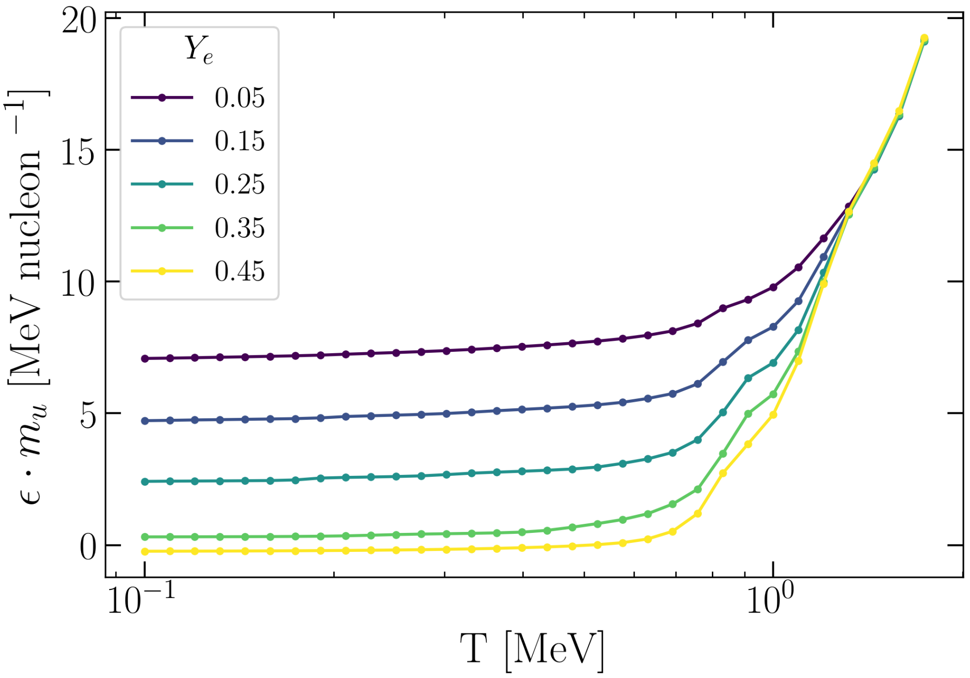

Figure 2.1.: specific internal energy ϵ calculated from the total Energy assuming fixed baryon mass over temperature T for different electron fractions Y_e at a fixed density of $4 \times 10^8 \mathrm{gcm}^{-3}$. At low temperatures the internal energy converges to the difference of the assumed baryon mass and the mass per baryon for the given composition. In cases where this mass per baryon is lower than the atomic mass unit are resulting in negative internal energy.

temperatures converges ϵ to the difference between the atomic mass unit and the resulting rest mass per baryon for the assumed composition. In some cases, for example for higher Y_e, where the composition consists mostly out of ^{56}Fe, which have a lower rest mass per baryon than the atomic mass unit, leads that to even negative ϵ. In the very neutron rich cases converges $\epsilon \cdot m_u$ to around 8 MeV per nucleon. The mass contribution is here the overwhelming dominant part. At low temperatures, the thermal part of the internal energy becomes negligible, as shown in Figure 2.1, where ϵ remains nearly constant. This makes the recovery of T challenging. In section (4.1) we will explain how the EoS was extended to lower temperatures and densities.

2.3.2. Artificial Viscosity

During the merger shocks are produced that heat the material. In addition, they affect the ejection of matter. Therefore, it is essential to consider shock in BNSM simulations. In SPH shocks can not be resolved directly. The SPH code uses therefore an artificial viscosity scheme based on the work of Chow and Monaghan [164]. An additional viscous pressure term, Π_{ab} (symmetric in a and b), is introduced in the first term of the momentum equation (2.28), while a viscous contribution to the total conserved energy, Ω_{ab} (also symmetric in a and b), is added in the first term of the energy equation (2.29). The viscous pressure term is

$$\Pi_{ab} = -2\frac{Kv_{sig}}{\rho_a^* + \rho_b^*}\left(\hat{u}_{i,a} - \hat{u}_{i,b}\right)e_i, \tag{2.43}$$

where e_i is the unit vector from particle a to b

$$\mathbf{e} = \frac{\mathbf{r}_a - \mathbf{r}_b}{|\mathbf{r}_a - \mathbf{r}_b|}. \tag{2.44}$$

$\mathrm{v}_{\mathrm{sig}}$ is the so-called signal velocity and K is a free parameter to adjust the strength of the artificial viscosity. Parallel to Π_{ab} is the energy contribution

$$\Omega_{ab}^i = -2\frac{Kv_{sig}}{\rho_a^* + \rho_b^*}\left(\tau_a^0 - \tau_b^0\right)e_i. \tag{2.45}$$

The signal velocity takes into account the sound speed but also the relative motion between particles. This is necessary since shock fronts can propagate supersonically. The signal velocity is approximated by

$$v_{sig} = c'_{v,a} + c'_{v,b} + |v_{ab}^*|\,, \tag{2.46}$$

with $v_{ab}^* = (v_a^i - v_b^i)e^i$ the relative projected speed of the particles a and b. The speed of sound c'_v as seen in the local frame is approximated by

$$c'_{v,a} = \frac{c_{v,a} + |v_{ab}^*|}{1 + c_{v,a}\,|v_{ab}^*|}. \tag{2.47}$$

For the free parameter K every particle is assigned to its own time dependent viscosity coefficient $\xi(t)$ [165]. K is then

$$K = 0.5(\xi_a + \xi_b)\cdot 0.5(f(a) + f(b)), \tag{2.48}$$

with

$$f(a) = \frac{|(\nabla\cdot\mathbf{V})_a|}{|(\nabla\cdot\mathbf{V})_a| + |(\nabla\times\mathbf{V})_a| + 0.0001c_{v,a}/h_s}. \tag{2.49}$$

The term f reduces the numerical heating in regions of strong vorticity while retaining good shock capturing attributes of the artificial viscosity [166]. The particle viscosity coefficient $\xi(t)$ evolves according to the equation

$$\frac{d\xi}{dt} = -\frac{\xi - \xi^0}{\tau_{\mathrm{visc}}} + S, \tag{2.50}$$

with

$$S = \max(-\nabla\cdot\mathbf{v}, 0) \tag{2.51}$$

Through a shock, S will increase ξ of the particle. After the shock ξ decays exponentially to its default value ξ^0 with a mean lifetime τ_{visc}. The time scale τ_{visc} is defined by

$$\tau_{\text{visc}} = \frac{h_s}{C_1 c_v}, \tag{2.52}$$

the smoothing length h_s, the speed of sound c_v and a non dimensional parameter C_1. In the simulations of this work $C_1 = 0.05$ and $\xi^0 = 0.01$ is typically used.

2.3.3. Ejecta

In this work, a greater focus will be on the ejected material. Given the fact that simulations are run for a limited time, it is necessary to define when a SPH particle is ejected. There are different criteria to use to define whether the matter becomes unbound. The geodesic criterion assumes that ejecta follow spacetime geodesics in a time-independent asymptotically flat spacetime. Therefore, the zeroth component of the contravariant 4-velocity u_0 is a conserved quantity. A SPH particle is unbound if

$$u_0 < -1. \tag{2.53}$$

The main critique point on this criterion is the assumption that the fluid just follows the spacetime geodesic. This is the case if matter just ejects ballistically but for outflows of BNSM thermal and nuclear binding energy impacts the acceleration of the fluid, which is ignored by this criterion.

The Bernoulli criterion states that matter is unbound if

$$hu_0 < -1. \tag{2.54}$$

Through enthalpy h this criterion considers the internal energy, and allows to account for thermal and binding energy. The Bernoulli criterion is based on the assumption of steady-state flow. Although this is in general not true for the outflows of the BNS merger, the criterion still captures the amount of ejecta reasonably well. A more in-depth discussion of both criteria can be found in [167]. In this work, we will use, if not stated otherwise, a virial criterion to decide when a SPH particle is unbound. It is derived and discussed in detail in [168]. It is analogous to the Newtonian energy criterion in which the total energy per unit mass $e_{\text{kin}} + e_{\text{int}} + e_{\text{pot}-}$ is great enough to leave the gravitational potential. The relativistic counterpart $\epsilon_{\text{stationary}}$ is

$$\epsilon_{\text{stationary}} = v^i \hat{u}_i + \frac{\epsilon}{u^0} + \frac{1}{u^0} - 1. \tag{2.55}$$

Material becomes unbound if

$$\epsilon_{\text{stationary}} > 0. \tag{2.56}$$

When we apply this criterion in later chapters we bring the -1 on the the other side and check

$$\epsilon_{\text{stationary}} + 1 = \epsilon_{\text{stat}} > 1. \tag{2.57}$$

Over time all three criteria will converge to the same result when the material is at large distance away from the gravitational potential. As the outflows expand, both pressure and internal energy eventually approach zero. In this limit the enthalpy will converge $h \to 1$ and 2.53 and 2.54 become identical. In the case of 2.55, using the definition of $\hat{u}_i$ from 2.25, the metric terms approach the weak field limit where $\alpha \to 1$, $\beta^i \to 0$ and $\psi \to 0$, and we get

$$\epsilon_{\text{stat}} = v^2 u^0 + \frac{1}{u^0} > 1. \tag{2.58}$$

Using the normalization condition $u^2 = -1$ which is in the weak field limit

$$\begin{aligned} \left(u^0\right)^2 \left(-1 + v^2\right) &= -1 \\ \Leftrightarrow 1 - \frac{1}{(u^0)^2} &= v^2, \end{aligned} \tag{2.59}$$

we can substitute v^2 in 2.58 and get

$$u^0 > 1, \tag{2.60}$$

which is in the weak field limit the contravariant version of 2.53. The limit, where all criteria converge, is in simulations typically not reached. We discuss the differences in the amount of ejecta at different times and distances between the different criteria in appendix B.

Considering internal energy for defining if material is unbound has also a drawback. Our ejecta criterion is prone to identify hot material as unbound. Even when this material has enough energy to overcome the gravitational potential, since it mostly thermal energy it still remains bound. To avoid defining hot disk material as ejecta we use additionally a radial cut, which will be always stated in the following chapters.

2.3.4. Post-merger gravitational wave signal and oscillations modes

In Section 2.1.1 we mentioned the numerical schemes implemented in the calculation of the gravitational wave signal of BNSMs. Here we want to describe the features and their cause of the post-merger signal, on an example SPH simulation of a 1.35-1.35 $M_\odot$ equal mass merger with SFHO as the used EoS and 339×10^3 particles.

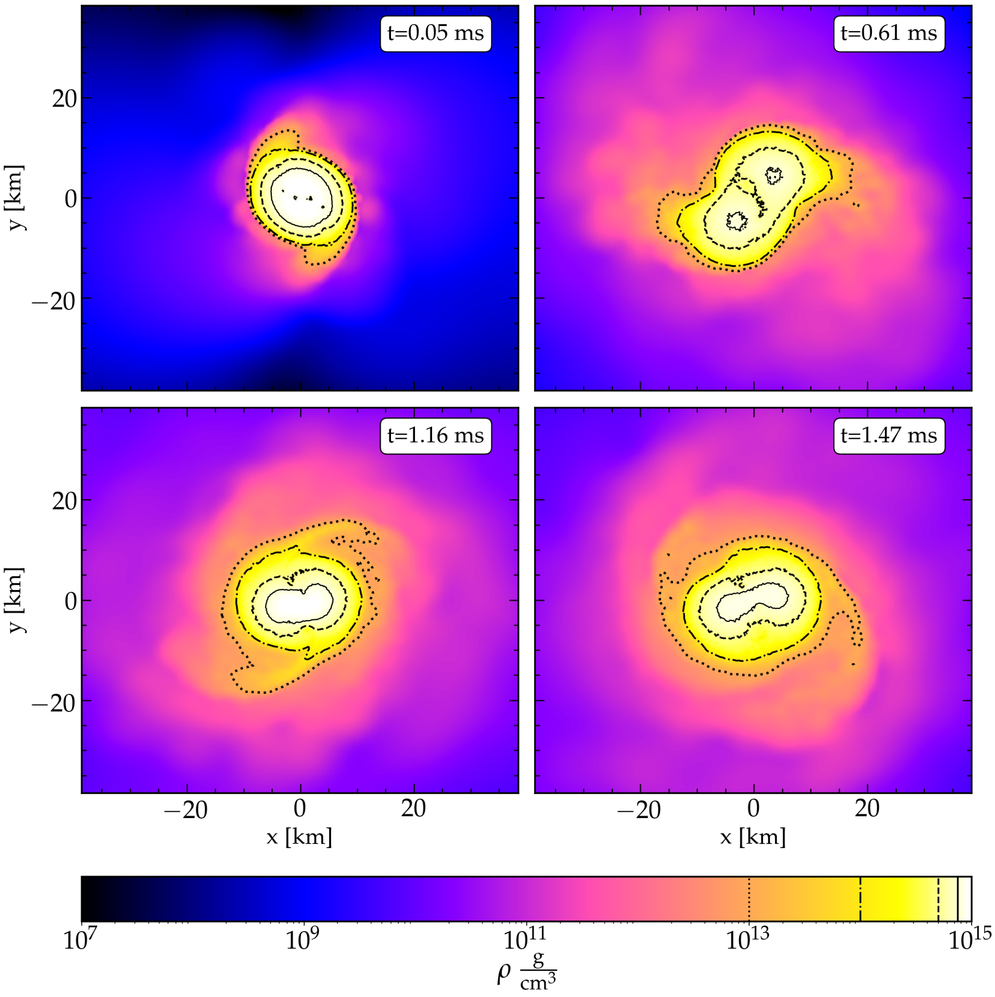

Figure 2.2.: Early Post-merger density profile of an BNSM SPH simulation in the x-y-plane. The four different panels show

In figure 2.2 we show the corresponding rest-mass density distribution of the system in the x-y plane at the very early post-merger phase for four different times. The four contour lines represent the borders of densities of 9×10^{14}gcm^{-3} (solid line), 5×10^{14}gcm^{-3} (dashed line),10^{14}gcm^{-3} (dashed-dotted line) and 10^{13}gcm^{-3} (dotted line). In this early evolution, one can identify the oscillations that are the cause of the post-merger signal GW. Most dominant is the quadrupole oscillation, the fast rotation of the double core structure of the hyper-massive neutron star. Over time, the core structure becomes more spherical, and the quadruple oscillations decrease. During the first oscillation cycles one can see that the distance between the two cores varies, which can be described as a quasi-radial oscillation on top of the quadrupole oscillation. Because of the tidal deformation of the two neutron stars during the merger, two diametrical bulges form which have a lower rotation frequency than the core structure, as can be seen from the changing relative orientation at different times of the bulges and the core structure. They form the spiral arms, which only survives for a few orbital cycles. These three oscillations lead to the main features of the post-merger GW signal.

Figure 2.3 shows the corresponding post-merger signal in the frequency domain. The strongest feature in the post-merger GW spectrum, called f_{peak}, is ascribed to the fundamental quadrupole oscillation mode (also called f_2) [37]. For our setup, the frequency of f_{peak} is 3.3 kHz, marked with a blue dashed line. Although the quasi-radial oscillation mode f_0 does not produce a signal GW, because of its spherical symmetry, in this environment it can be coupled with the quadrupole mode f_{peak} and create two secondary frequency peaks $f_{2\pm0} = f_{\text{peak}} \pm f_0$ (green dashed line and orange dashed line). Another secondary feature is f_{spiral}, which is generated by the orbital motion of tidal antipodal bulges [38] (yellow line). Since the bulges move slower, the central structure has a secondary frequency peak of slightly lower frequency than f_{peak}.

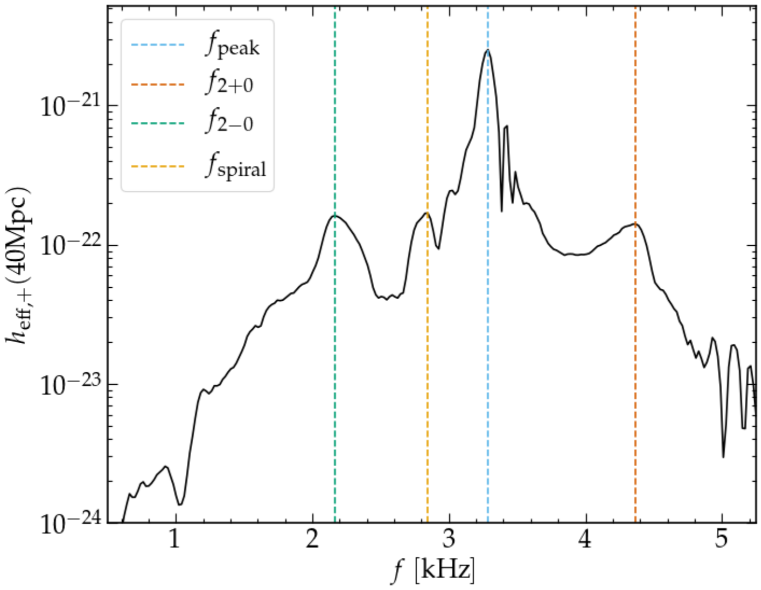

Figure 2.3.: Post-merger gravitational wave signal from a SPH simulation in the frequency domain. The colored dashed vertical lines are marking the frequency peaks f_{peak},f_{2+0},f_{2-0} and f_{peak}.

Another way to study the mass oscillations is by using the complex azimuthal mode decomposition of the conserved rest-mass density integrated over the equatorial plane

$$P_i = \int_{\mathbb{R}^2} \rho^* e^{-im\phi} dx\, dy. \tag{2.61}$$

From these modes, one can identify symmetry breaking in the density distribution. The m=1 mode is a measure for the contravention of 180°-rotation-symmetry (m=2 for 90°-rotation-symmetry and so on) and is therefore used in studies to investigate the one arm spiral arm instabilities [169–171]. In figure 2.4 we show from this example simulation the different density modes. In the left panels, we show the raw calculated modes. Since higher modes can be quite noisy especially, for an easier comparison, we will use the smoothed modes using the Savitzky-Golay filter [172] as shown in the right panel. Hydrodynamical vortices form during the merger (under-dense regions in the center as seen in the upper left panel in figure 2.2). In the early post-merger period, the m = 2 mode, which was the main driver of the inspiral GW emission, remains the dominant as long as the double core structure exists in the remnant. The vortices are moving to the center over time and the double cores subsequently form one off-center core of the remnant. This leads to the rise of the m = 1 mode in the first milliseconds after the merger, and it stays the most dominant after that. We will investigate differences in the post-merger GW signal and density modes in Chapter 3 through the impact of stochasticity and artificial viscosity.

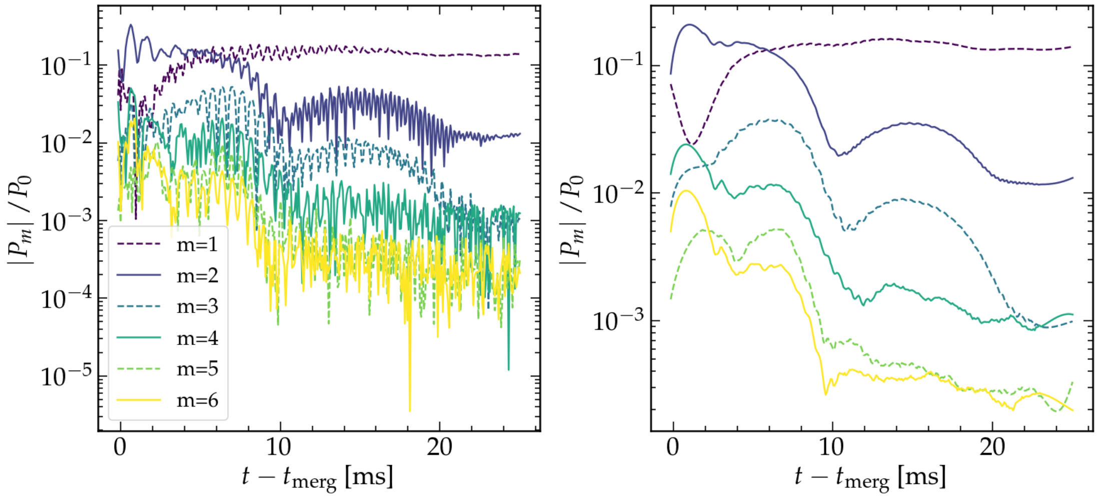

Figure 2.4.: Normalized amplitudes of density modes on the equatorial plane. Left panel: unfiltered modes, right panel: smoothed modes using the Savitzky-Golay filter.

3. Fluctuations in BNSM evolution

3.1. Numerical vs. physical fluctuations in BNSM

Various mechanisms are responsible for the mass ejection in BNSM. In the initial stages of the merger, the NSs develop tidal arms that eject cold, neutron-rich material within the equatorial plane. On the impact interface shock-heated material is blown out in all directions. Some of the matter around the new central object forms a disc, and the tidal arms induce a spiral wind, pushing further material outwards. On timescales that exceed the merger duration, the remnant-disc system expels secular ejecta (neutrino driven wind, viscous outflows). The amount of mass that is ejected depends on the binary system. The mass ratio between the two NSs is an important factor. In more asymmetric mergers, the lighter NS becomes disrupted, forming a more massive tidal arm which ejects more mass and forms a more massive disc [25, 30, 33, 173–176]. Moreover, the total mass of the system impacts mass ejection. More massive systems tend to eject more matter, while beyond the threshold mass M_{thresh}, at least the dynamical mass ejection is reduced because of the prompt collapse into a BH [30].

The total amount of ejecta mass remains not well constrained. Since it also depends on the EoS, one might hope that observations, such as the GW signal, which provides information about the total mass and mass ratio of the binary system, together with the kilonova light curve, which may constrain the ejecta mass, could also help constrain the EoS. However, this is already a challenging task, as deducing the amount of ejecta from the light curve is highly model-dependent, and it is unclear to which precision is this possible. Also, this is true only insofar as the ejecta mass closely correlates to the masses within the binary system, which does not necessarily need to be the case.

Merger events are very dynamical and chaotic, and it could be the case that already small seed perturbations lead to different outcomes. Small perturbations may result from the intrinsic rotation of NSs with rotation axis non-aligned to the orbital axis, or inhomogeneities of their magnetic fields. These minor differences would be unnoticeable and the variation in outcome for the same observable parameter could be characterized as stochastic effects. Furthermore can the material orbiting around the newly formed remnant in a BNSM have a chaotic behavior. It is well established that simple systems in general relativity, such as a point mass in orbit around a BH, can exhibit complex and chaotic behavior, being highly sensitive to initial conditions [177–180]. In these systems, even minimal differences in angular momentum can lead to drastically different orbital trajectories. At the moment, it is not known whether small perturbations significantly affect the evolution of BNSM systems.

In a recent study, Collins et al. [143] discuss the possibility of such stochastic effects. They analyze merger simulations with small increments in total binary masses. They observed variations in the total ejecta mass and the north-south symmetry of the mass distribution of about 10% between near-by models.

Besides this findings, stochastic effects in BNSM has not been investigated. It is not clear, if observed variations in simulations have a physical reason or are purely numerical. BNSM simulation are computational highly demanding. Many different physical effects across various length and time scales need to be addressed with numerical methods which only allow for a finite accuracy. This makes it challenging to identify variations as physical or numerical and it might even not possible with the state-of-the-art simulation codes.

In this chapter we will explore how strong are the variations in the results of simulations with the same physical system using our numerical setup described in chapter 2. In our setup the NSs are irrotational and we do not consider magnetic fields but chaotic behavior could still be which can occur. Regardless of the presence of physical stochastic effects, it is crucial to account for variations in simulation results when drawing conclusions from them. We will focus on the impact on the ejecta and try to give first indications what might be the cause of the variations.

3.2. Ejecta

In the following, we will investigate the stochasticity of simulation results in our setup. First, we check how much stochasticity impact the evolution of ejecta. Therefore, we conduct a set of simulations that are physically equivalent. Then, we test how much different quantities of the ejecta are fluctuating and discuss on the basis of the results correlations and possible reasons.

We set up a BNSM 1.35-1.35 $\mathrm{M}_\odot$ system with a total of 339×10^3 SPH particles and the SFHO EoS. The system is brought to a well-defined initial condition by the relaxation scheme explained in [162] on a circular orbit. To test the effect of stochasticity we take the relaxed set up and rotate it around the center of mass. Thus the neutron stars will inspiral and collide at different angles in the coordinate system of the metric grid, which is described in 2.1.1, while physically the initial conditions are the same. We run 13 simulations up to 25 ms after merger which are rotated between 0° and 180° in 15° steps. We will in the following refer to individual simulations of this set by their corresponding rotation angle (0°-simulation, etc.).

Figure 3.1 shows the ejecta masses outside 100 km (1000 km) over time for the 13 simulations. The mean value of ejected matter at 25 ms after merger is $1.6 \times 10^{-2}\mathrm{M}_\odot$ $(5.1 \times 10^{-3}\mathrm{M}_\odot)$. While the spread around the mean value is around ± 25 % (± 20 %) as can be seen in the lower panels of 3.1. A possible reason for the variations could be uncertainties from the metric grid. In our setup, we utilize a three-dimensional Cartesian grid measuring approximately 143 km along each axis, with a cell size of 1.1 km. The finite resolution may cause an orientation dependence. This dependence could result in variations in the metric potentials α, ψ, and β^i for different rotational angles, thereby influencing the acceleration of the NSs. If the finite resolution would cause a orientation dependence, we would expect to see a pattern in the ejecta masses. The cartesian metric grid has a 90° rotation symmetry which we do not see in the variation of the amount of ejecta. Even the 0° simulation compared to 180° simulation, which only swaps the two NSs have different ejecta masses. This might an argument against uncertainties in the metric as the direct cause. However, during the relaxation phase the NSs might build small inhomogeneities which are not symmetric and result in different evolution for different rotation angles.

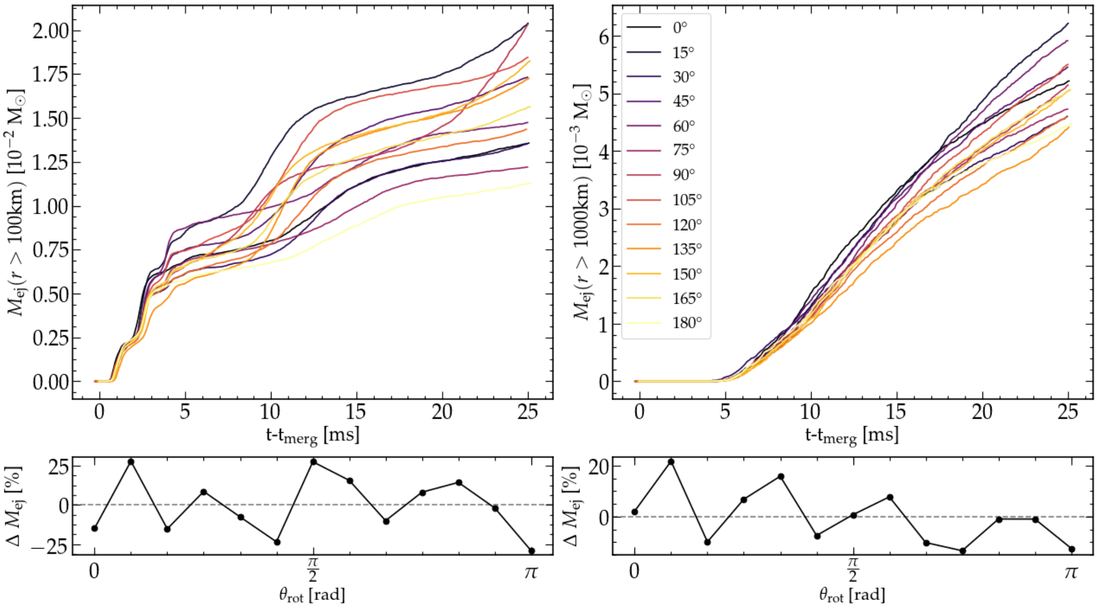

Figure 3.1.: Ejected mass over time outside a radius of 100 km (left) and 1000 km (right) for 13 simulations which started with a different orientations between 0° and 180° in respect to the metric grid. Lower panel shows how the variation of ejecta mass in per cent compared to the average ejecta mass of all 13 simulations over the rotation angle. There is a spread in ejecta mass up to 50 % and no direct dependence on the amount of ejecta and rotation angle.

If this were the case, the center-of-mass velocity for the NSs and the velocity spread among all SPH particles within each NS would be affected. We check the sum of the center of mass velocity of both NSs before merger

$$v_{\mathrm{cm},1} + v_{\mathrm{cm},2} = v_{\mathrm{cm,tot}}, \tag{3.1}$$

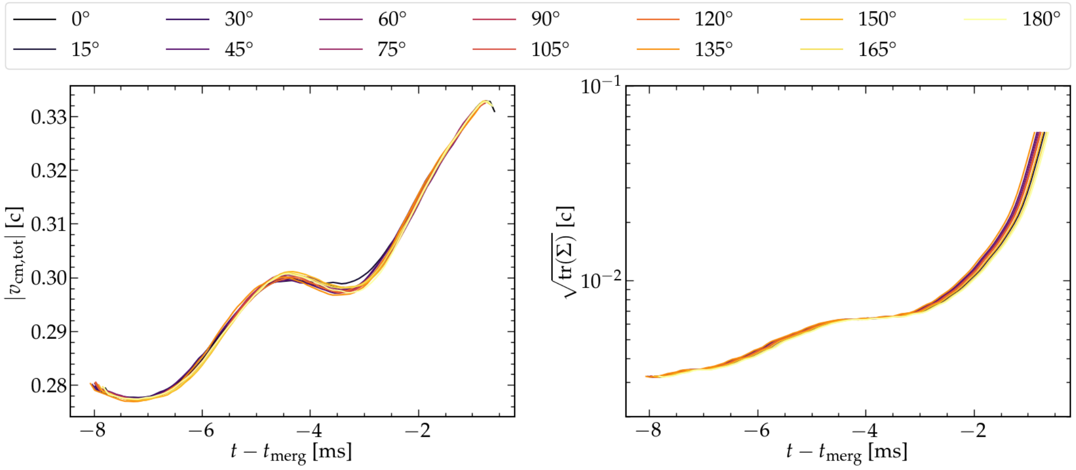

Figure 3.2.: Variance in impact velocity and its asymmetry for all 13 simulations. Left panel: Difference between the maximal coordinate velocity of the mass centers of the two NSs. Right panel: sum of the maximal coordinate velocity of the mass centers of the two NSs.

where $v_{\mathrm{cm},1}$ is the center of mass velocity of one NS and $v_{\mathrm{cm},2}$ of the other. We use the coordinate velocity which is in the simulation recovered from the evolved quantities but does not have a physical meaning in GR. To check the variance of velocity we define first the variance for a velocity vector component j

$$\sigma_{jj}^2 = \frac{\sum_i M_i \left(v_{j,i} - v_{\mathrm{j,cm}}\right)^2}{M_{\mathrm{tot}}}. \tag{3.2}$$

The variance of a vector $\mathbf{v}_{\mathrm{cm}}$ can be described by the variance-covariance matrix

$$\Sigma = \begin{pmatrix} \sigma_{xx}^2 & \sigma_{yx}^2 & \sigma_{zx}^2 \\ \sigma_{xy}^2 & \sigma_{yy}^2 & \sigma_{zy}^2 \\ \sigma_{xz}^2 & \sigma_{yz}^2 & \sigma_{zz}^2 \end{pmatrix} \tag{3.3}$$

To compare a scalar measure of the total spread of the velocity vector we calculate the square root of the trace of Σ.

$$\sqrt{\mathrm{tr}\,(\Sigma)} = \sqrt{\sigma_{xx}^2 + \sigma_{yy}^2 + \sigma_{zz}^2}. \tag{3.4}$$

To capture the velocity spread in both NSs, we calculate the average of their respective velocity spreads.

Figure 3.2 shows in the left panel the sum of both center of mass velocities during the inspiral phase until the NSs reaches its peak velocity. The right panel shows the spread in velocity for both NSs. The 0 ms point is defined for each simulation when the density reaches its maximum during the merger. The NSs are touching over a millisecond before that point and the deformed bulges might touch before the center of mass velocity reaches its maximum. The center of mass velocity difference between the simulations is quite stable and varies only up to 0.5%. Over the inspiral phase is the spread in velocity over all SPH particle in the NSs comparable and less than 1 %. Only around 3 ms before merger when the NSs gets stronger deformed and are about to touch, the spread in velocity rises and also diverges between the 13 simulations. During the inspiral both NSs are affected by numerical heating. Especially at the last milliseconds when the stars deform to a drop shape, the NS crust heats to a temperature of a 2 - 3 MeV, which can also impact the spread in velocity.

From our findings we can not exclude that metric uncertainties play a role in the observed variations of the ejecta mass. However, the spread in velocity within the NSs only diverges between the simulations at times where viscous heating and hydrodynamical effects starts to matter.

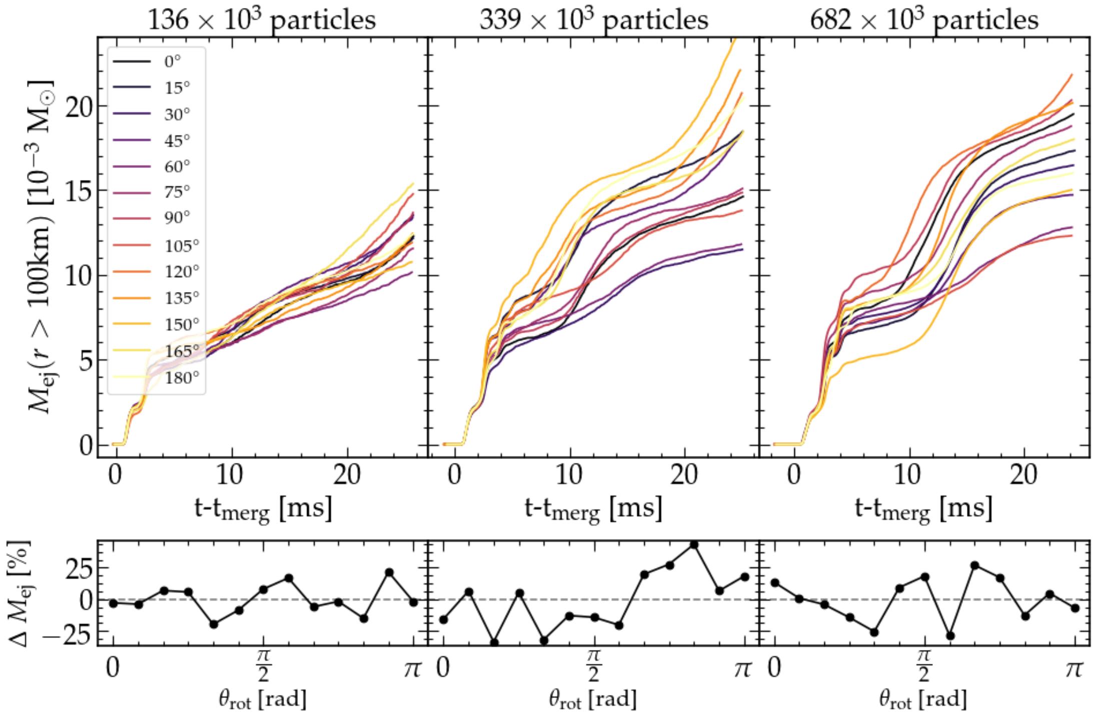

Figure 3.3.: Ejected mass over time outside a radius of 100 km for three sets with different resolution of 13 simulations which started with different orientations between 0° and 180° in respect to the metric grid. Left panel shows for simulation with 136×10^3 particles, middle panel for 339×10^3 particles, and right panel for 682×10^3 particles. Lower panels show the variation in percent compared to the average ejecta mass of each set.

Another possibility could be that numerical uncertainties in the hydrodynamics are the main driver of this variance. We would expect that if the finite discretization of the fluid in SPH particles lead to variations that with a increasing number of particles we would see a converging trend. We conduct a resolution study with additional simulations as the 13 described at the start of the chapter, but this time three sets of 13 simulations. The difference between each set is the total number of SPH particles. One set has 136×10^3 particles, one set 339×10^3 particles again and one set 682×10^3 particles. In this test we run the 339×10^3 particles set again, since we did some minor numerical adjustments to reduce some possible sources of non-deterministic behavior, such as the order of the neighbor particles when summing over them, and for the comparison we want to use the exact same setup.

Figure 3.3 displays for all three sets of simulations the spread of ejecta. Surprisingly, we do not see a reduction of the variation by increasing the resolution. The simulations with 682×10^3 particles have a comparable spread of $\pm 25\%$ in ejecta mass as the simulations with 339×10^3 particles. In the set with 339×10^3 particles we see three simulations which start a steep increase in ejecta just before the end of the simulation leading to a spread of $\pm 35\%$ in ejecta mass this time. The trend indicates that over longer time the spread in ejecta mass might diverge even further between simulations within a set. The variance is lower by the set of simulations with 136×10^3 particles to less than $\pm 20\%$. These results speak against the assumption that the finite discretization of the fluid is the cause of the variation. It may hint to viscous effects such as Kelvin-Helmholtz instabilities which are less resolved at lower particles numbers. Next we will check how the ejecta distribution is impacted by the variations.

3.2.1. Distribution and symmetry

We will focus for the rest of this chapter on the first 13 simulations we described at the start of this section.

Interestingly, in comparing the lower panels of 3.1, the variation in ejecta mass differs between regions beyond 100 km and 1000 km. For instance, the 60° simulation shows approximately 7% less ejecta mass than the average beyond 100 km, but about $\sim 15\%$ more than average beyond 1000 km. The difference points out that not only total mass fluctuates but also the ejecta distribution. The matter closer to the remnant at 25 ms after merger identified as ejecta by the employed criterion has slower velocities and higher temperatures. The faster outflowing material is relevant for the early kilonova signal of the first days, since through faster expansion, it will become transparent earlier. However, in the amount of time we are simulating the post-merger phase we may have fast inner ejecta that should loose speed as it collides with slower ejecta. But in general, differences in the distribution of velocity may result in changes to the timing of peak luminosities, occurring either earlier or later. Also asymmetries in the angular distribution has the effect that the observed spectrum of the kilonova is dependent on the viewing angle.

We will look into the north-south symmetry defining by

$$\Pi_M = \frac{M_{\text{north}} - M_{\text{south}}}{M_{\text{north}} + M_{\text{south}}}, \tag{3.5}$$

and polar-equatorial symmetry defining sphericity by

$$\Upsilon_M = \frac{M_{\text{eq}} - M_{\text{pol}}}{M_{\text{eq}} + M_{\text{pol}}}, \tag{3.6}$$

where M_{pol} is the ejecta mass at polar regions with a solid angle $\Omega = 2\pi$ corresponding to a polar angle $\theta = [0°, 60°]$ and $\theta = [120°, 180°]$, which encloses the same solid angle as the equatorial region for M_{eq} which corresponds to a polar angle $\theta = [120°, 180°]$. Figure 3.4 shows polarity and sphericity over the rotation angle in the left panel. The right panel shows the velocity distribution from the 0°-simulation with red bars for each velocity bin to visualize the spread between the 13 runs. The velocity bins have the size of Δv=0.02 c. For all three quantities only ejecta outside 1000 km at the end of the simulation was considered. Across all 13 simulations, the velocity distribution shows a peak at approximately 0.2 c, followed by a decrease extending to 0.7 c, with some individual SPH particles reaching velocities as high as 0.85 c in a few runs. The main difference between the runs is in the width and height of the velocity peak. A higher peak also corresponds to a more rapid decline to 0.7 c, as illustrated by the red bars. This means less fast material, which would correspond to a weaker early kilonova light signal.

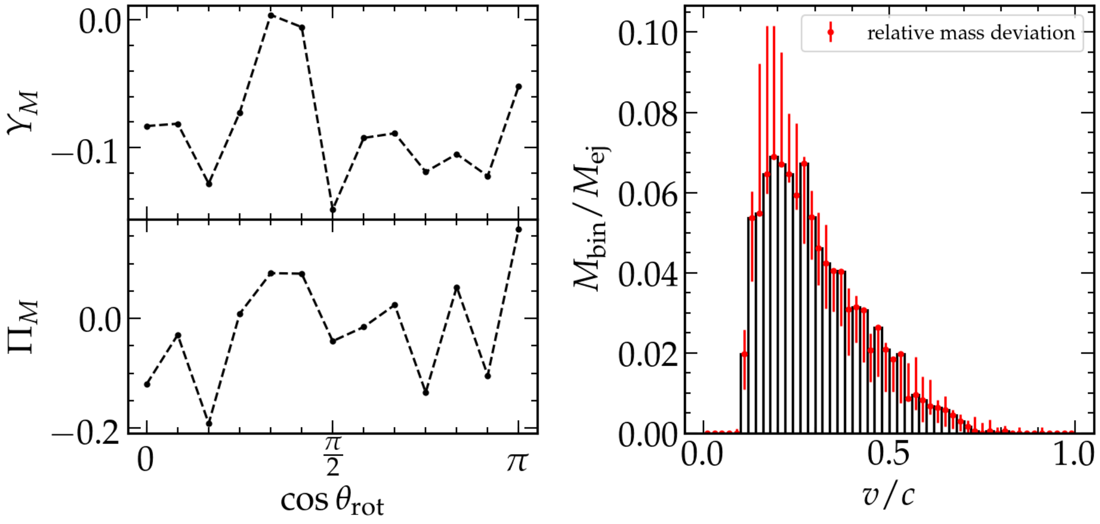

Figure 3.4.: left: Sphericity and polarity, as defined in 3.5 and 3.6, over rotation angle of the 13 simulations for ejecta outside 1000 km at 25 ms after merger. Sphericity varies around 15 % and polarity more than 20 %. right: velocity distribution of ejecta outside 1000 km at 25 ms after merger for the 0°-simulation normalized to the total ejecta mass. Red bars shows how velocity distribution varies between 0°-simulation and the other 12 simulations.

The north-south asymmetry fluctuates around 20%. It ranges from 20% more mass in the southern hemisphere for 0°-simulation up to 7% more mass in the northern hemisphere for the 180°-simulation. The 60°-simulation only deviates 1 % from being north-south symmetric. On average, there are more simulations with more mass in the souther hemisphere. All 13 simulations have a oblate distribution, which means they have more mass in the equatorial region. However, it varies around 15%. The 90°-simulation exhibits a mere 1% increase in mass within the equatorial plane and maintains a high level of symmetry.

These symmetry fluctuations are important to take into consideration for interpreting BNSM detections like GW170817 and the corresponding Kilonova AT2017gfo. Sneppen et al. [181] found, using the strong Sr^+ absorption-emission feature of the Kilonova, that it is remarkably spherical at the first 5 days. In this study is pointed out that current numerical simulations of merger typically produce aspherical ejecta, referencing as example three simulation studies [25, 30, 182]. This was interpret as a possible challenge to current explosion models. For more asymmetric binary component masses, it is understood that through the stronger deformation of the lighter NS, a more massive tidal arm is formed which ejects more matter in the equatorial plane (as seen in [25, 30, 182]). This may indicate that GW170817 was closer to an equal mass merger. From the GW signal GW170817, the mass ratio of the binary system is $q \in (0.7, 1.0)$, which would allow this conclusion [87]. We want to point out that one of the referenced studies [30] used the same SPH code, and one of the symmetric merger simulations used the same resolution, EoS and total mass as in our study. While this study showed aspherical ejecta, we see now that taking stochasticity of the simulations into account, this is not so clear anymore, since within the range of variation, we find simulations which have a sphericity close to zero. This highlights the significance of considering stochasticity, when it comes to interpreting simulation results. We need to point out that this study only addressed dynamical ejecta, and the kilonova study showed that also secular ejecta needs to be spherical, which we do not address here. Also [143] showed that asymmetry in the ejecta mass distribution does show less asymmetry in the kilonova light curves since the observer does not only view radiation emitted from one region of the ejecta.

Next we want to look at the post-merger GW signal and look how the variation affects it. We will also search for possible correlations between the signal and the ejecta evolution.

3.3. Gravitational waves

The mass of the dynamical ejecta is very small relative to the total mass of the binary system, making it extremely sensitive to slight variations in evolution during the highly dynamic merging phase. We examine the post-merger GW spectrum to determine if the variations observed in the ejecta are also reflected there. Figure 3.5 shows the 13 spectra in frequency domain. The strongest feature in the post-merger GW spectrum, called f_{peak}, is ascribed to the fundamental[1] quadrupole oscillation mode.

---

[1] fundamental means in this context, the lowest frequency mode of the oscillation

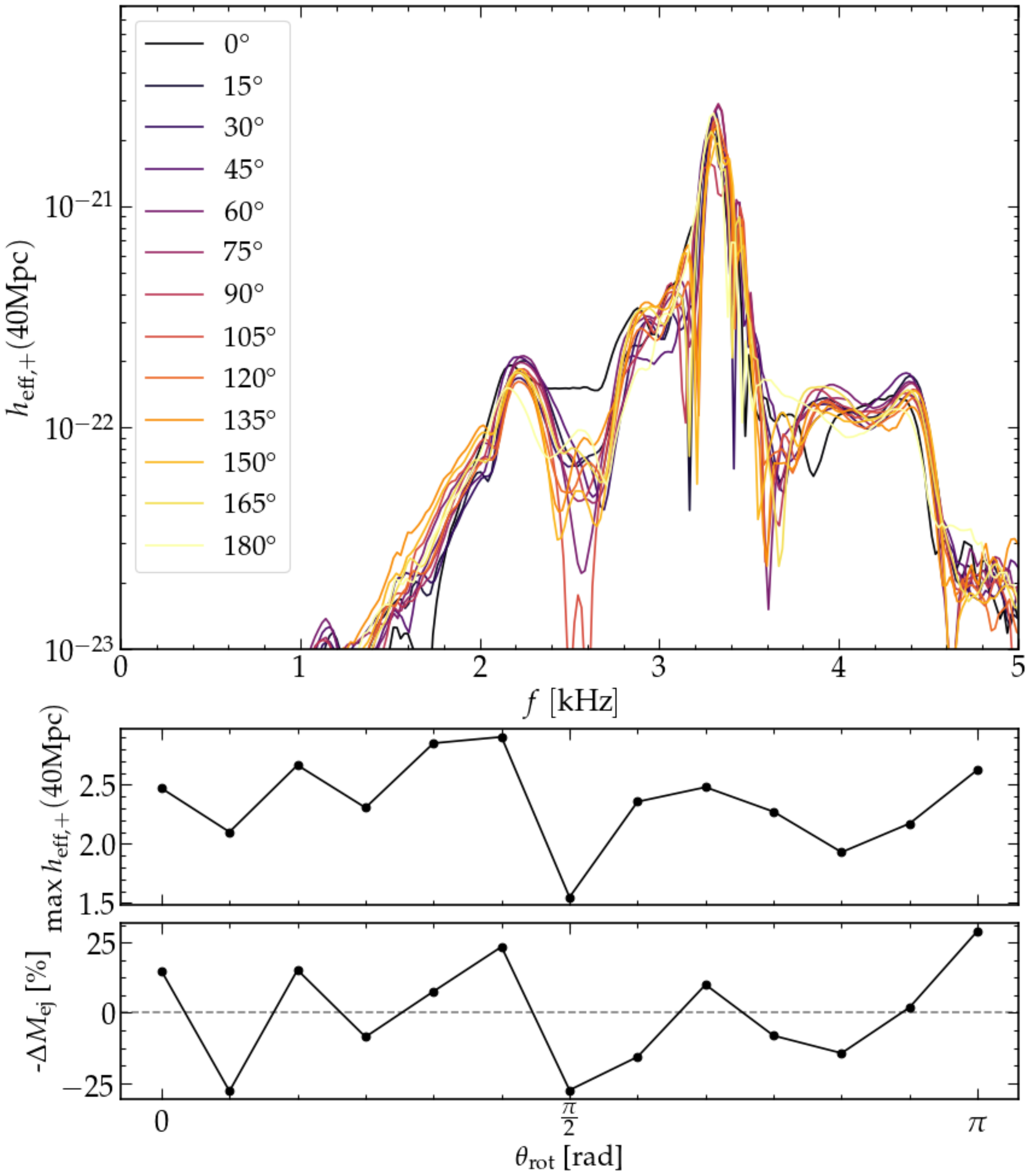

Figure 3.5.: Upper panel: effective GW spectra $h_{\mathrm{eff},+}$ of the post-merger phase in frequency domain for 13 simulations with different orientation to metric grid. Middle panel: Maximum amplitude of f_{peak} over the rotation angle. Lower panel: Variation of the total ejecta mass over the rotation angle. A correlation between the amount of ejecta mass and the amplitude of f_{peak} is apparent.

f_{peak} depends on the EoS and the total mass of the system. For our set up the frequency of f_{peak} is 3.3 kHz. The effect of the stochasticity on the frequency is insignificant with a variation smaller than 50 Hz.

Besides f_{peak} we identified additional secondary features in the spectra as the two frequency peaks $f_{2\pm0} = f_{\text{peak}} \pm f_0$ from the coupling of the quadrupole mode and the quasi-radial oscillation. We estimated for these simulations the frequency of f_0 from the Fourier transformation of the oscillation of the maximum density at the first 5 ms after merger, because f_0 is not distinctively visible in the GW signal. We get on average a $f_0 = 0.995$ kHz. Between the runs, frequencies of f_0 differ up to 30 Hz.

This approximately matches with the peaks around f_{2-0}= 2.2 kHz and f_{2+0}= 4.4 kHz. The slight inequality comes from the fact that we determine $f_{2\pm0}$ at the early post-merger phase, when the remnant and the different oscillations still can evolve rapidly. Under this consideration is the numerical uncertainty of f_{peak} and f_0 not relevant.

Another secondary feature is f_{spiral}, which is generated by the orbital motion of tidal antipodal bulges formed during the merging phase [38]. These bulges formed through the strong deformation during merging and rotate slower than the inner core of the remnant. They form the spiral arms which only survives for a few orbital cycles. This leads to a secondary peak with a slightly lower frequency than f_{peak}. We define f_{spiral} by the highest peak next to f_{peak} which is around 2.85 and 3.15 kHz. It is noticeable that the spectral morphology exhibits more variations around that frequency range. In this range, several spectra display 2 or 3 minor peaks instead of a single prominent one.

The morphology depends on the temporal evolution of the frequency f_{spiral}, making it non-trivial to define f_{spiral}. Between the 13 simulations a variation in frequency for f_{spiral} up to 300 Hz is stronger than the other features of the spectrum. f_{spiral} also couples with the quasi-radial oscillation f_0 and produces a secondary peaks $f_{\text{spiral}\pm0}$ [183]. This would correspond to peaks at around 4 kHz and 2 kHz which are visible features in the spectra. Also on these feature variation over 200 Hz can be identified between the simulations. This suggests that the evolution of the spiral arms is correlated with fluctuations in the ejecta, which is logical, as faster or more massive spiral arms can eject more material.

By looking for any correlations between different features of the GW signal and the ejecta we had one interesting finding, which we show in the middle and lower panel of figure 3.5. In the middle panel is the amplitude of f_{peak} depicted and the lower panel shows the variation of the total ejecta mass in terms of the average over the rotation angle as in 3.1, but inverted. Both depicted over the rotation of the 13 simulations. While the amplitude of f_{peak} also does not change dramatically, one can see in comparison that the trend between the amplitude of f_{peak} and the total amount of ejecta is anti-proportional. This correlation might give hints how the stochasticity impacts the ejecta mass.

Figure 3.6 compares spectrograms, which utilize a wavelet-based scheme [184]. The top and right panels show the GW signal $h_+(t)$ in the time-domain and its Fourier transformed frequency spectrum. We compare the spectrograms of the 75°-simulation and the 90°-simulation, which have the strongest and weakest amplitude of f_{peak} in the set. The amplitude of f_{peak} is affected by the evolution of the dominant frequency. In case of the 75°-simulation the post-merger GW signal decays over a period of 20 ms. In the spectrogram one can see that in the first 5 ms after merger several frequency components contribute but after that only the dominant frequency at 3.3 kHz remains.

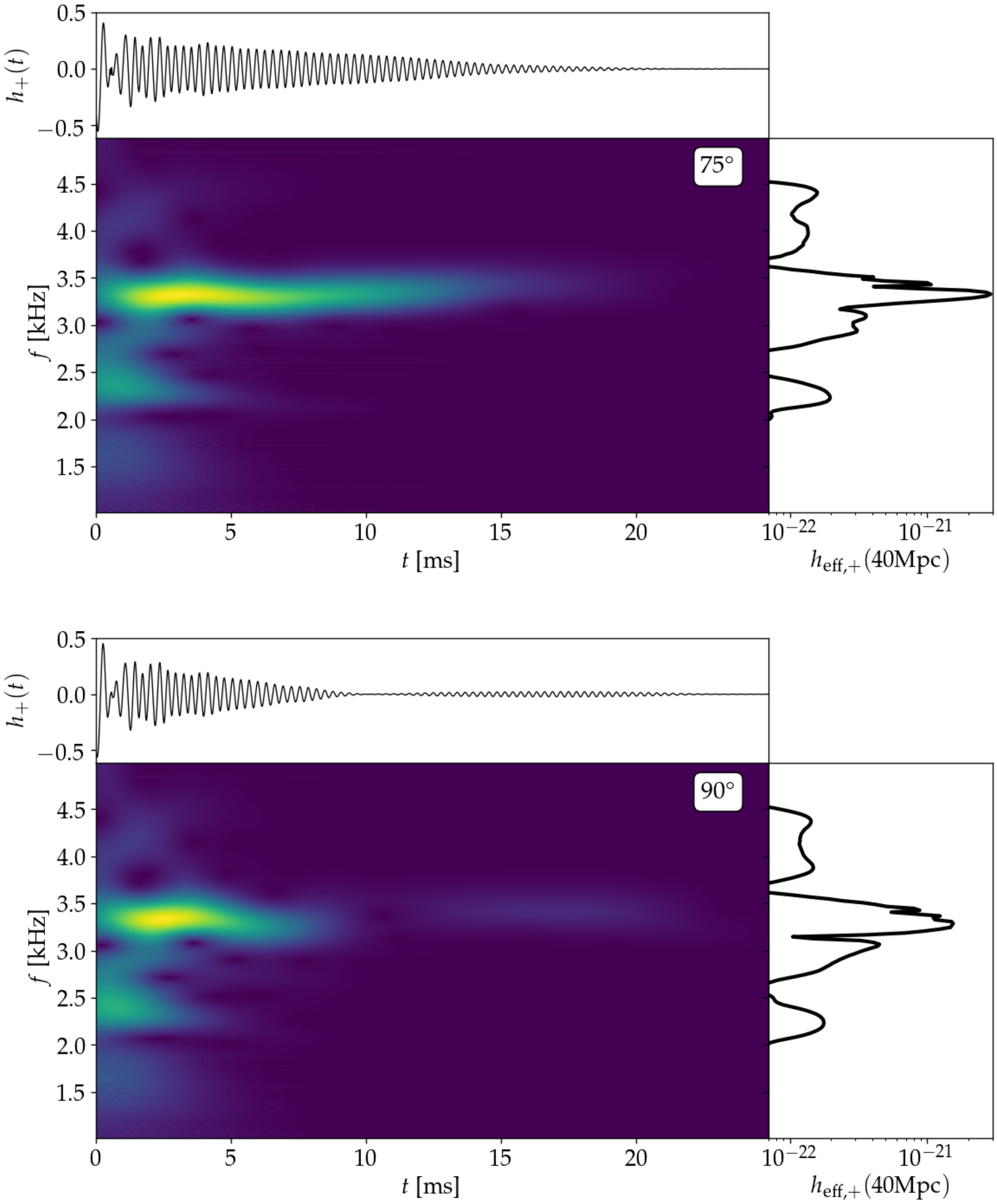

Figure 3.6.: Spectrogram of the strain $h_+(t)$ for the 75°-simulation and the 90°-simulation. The top and right panels show the time-domain waveform component of $h_+(t)$ and frequency-domain spectrum. respectively. The spectrograms are constructed using a wavelet-based scheme. One can see that the 75°-simulation has a stronger f_{peak} amplitude because the dominant frequency decays slower.

This results in a narrow and higher f_{peak}. For the 90°-simulation we see that the signal decays faster over a period of 10 ms with a slight re-excitation between 12 and 20 ms. In the spectrogram are the first 5 ms comparable with the 75°-simulation creating the secondary frequency features. The dominant frequency component has a slightly stronger shift towards lower frequencies and decays faster. At 12 ms seconds the component gets re-excited at a slightly higher frequency. The stronger drift combined with the faster decay results in a wider f_{peak} with a reduced amplitude.

The variation in the post-merger GW signal indicate that the spread in ejecta mass is linked with the evolution of the remnant. We will look in the next section into the evolution of the density distributions.

3.4. Density distribution

First, we look into m=2 azimuthal mode decomposition of the rest mass density using equation 2.61. As described in section 2.3.4 m=2 is the dominant mode during the in-spiral phase causing GW emission. During the early post-merger phase, a double core structure forms and the m=2 remains dominant, albeit decaying over time. We observe for all 13 simulations that the m=2 mode decays to a local minimum at times between 9 and 15 ms after merger before getting in some cases re-excited or the decay just slows down until m=2 mode stays constant.

Figure 3.7 shows in the right panel the strength of m=2 mode normalized to m=0 for all simulations over time. We compare it with the mass ejection rates $\dot{M}_{\text{ej}}$ shown in the left panel. The first dominant peak of $\dot{M}_{\text{ej}}$ is caused by the impact of the two NSs expelling shock heated material from the surface of contact. During the merging process through the quasi-radial oscillation of the double core structure more shock heated material is expelled from the remnant creating the second and third peak of $\dot{M}_{\text{ej}}$. In this early time spiral arms are forming at the outer layers. After that we see also around 9 to 15 ms another local maximum in $\dot{M}_{\text{ej}}$. In the lower panel of 3.7 we show a comparison between the times of the maximum of $\dot{M}_{\text{ej}}$ (black line) and the local minimum in the m=2 mode (gray line) of all 13 simulations, which are in a good agreement with each other. In all cases, the m=1 mode is increasing in strength from the merger phase and is at that time of the local minimum of m=2 already the dominant mode. This dominance of the m=1 mode was in previous studies linked to the one-armed instability [169–171, 185].

The comparison between the m=2 mode strength and $\dot{M}_{\text{ej}}$ shows a clear correlation of the breakdown of the double core structure towards a one-armed spiral instability and mass ejection. The bar shaped double core merges into a single core with an offset to the center of mass. This imbalance feeds one strong spiral arm as counterbalance. During the formation of the one-arm spiral material gets expelled into the disc through shock heating. We want to note that we do not see a local maximum around 10 ms in $\dot{M}_{\text{ej}}$ if we use the geodesic criteria to define ejecta, which shows that the expelled material in this process mostly gets thermal energy.

The variation we see in the one-arm instability agrees well with the variation in f_{peak} amplitude and the variation in the amount of ejecta per simulation. The double core oscillation is the strongest post-merger source of GWs. The earlier the double core breaks down, the earlier it stops emitting GW at 3.3 kHz for our set up and the weaker gets the amplitude of f_{peak}, while the earlier switch to the one-arm instability leads to an earlier increase in mass ejection which results in a higher total amount of ejecta at the end of the simulation.

Figure 3.8 illustrates a comparison of the remnant density evolution between two simulations. Left panel shows the density distribution from the 75° simulation, which has longer lasting strong m=2 mode and the right panels show the 90° simulation which had a quickly growing one-arm instability. The two upper panels show the density profiles during the inspiral. In the second panels is seen the density profiles shortly after merger when the double core structure and the two spiral arms are forming. At both times, the density profiles look especially in the high density region very similar. In the next two panels, the remnant is shown at around 5 ms after merger.

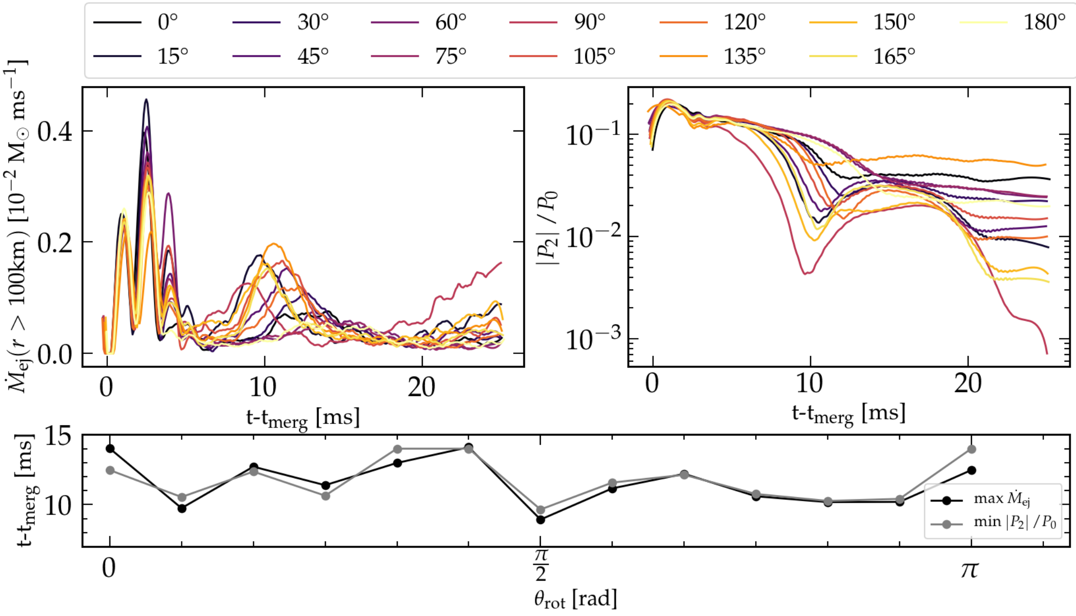

Figure 3.7.: upper left panel: mass ejection rates $\dot{M}_{\text{ej}}$, upper right panel: m=2 density mode over time. The different mass ejection rates have a local maximum around 10 to 15 ms after merger, at the same time the m=2 mode has a local minimum before re-excitation. Lower Panel: Comparison between the times of local $\dot{M}$ maxima and m=2 density mode minima over the rotation angle. Both agree with each other indicating a correlation between m=2 mode and the ejection rate. Both $\dot{M}_{\text{ej}}$ and m=2 modes are smoothed using the Savitzky-Golay filter.

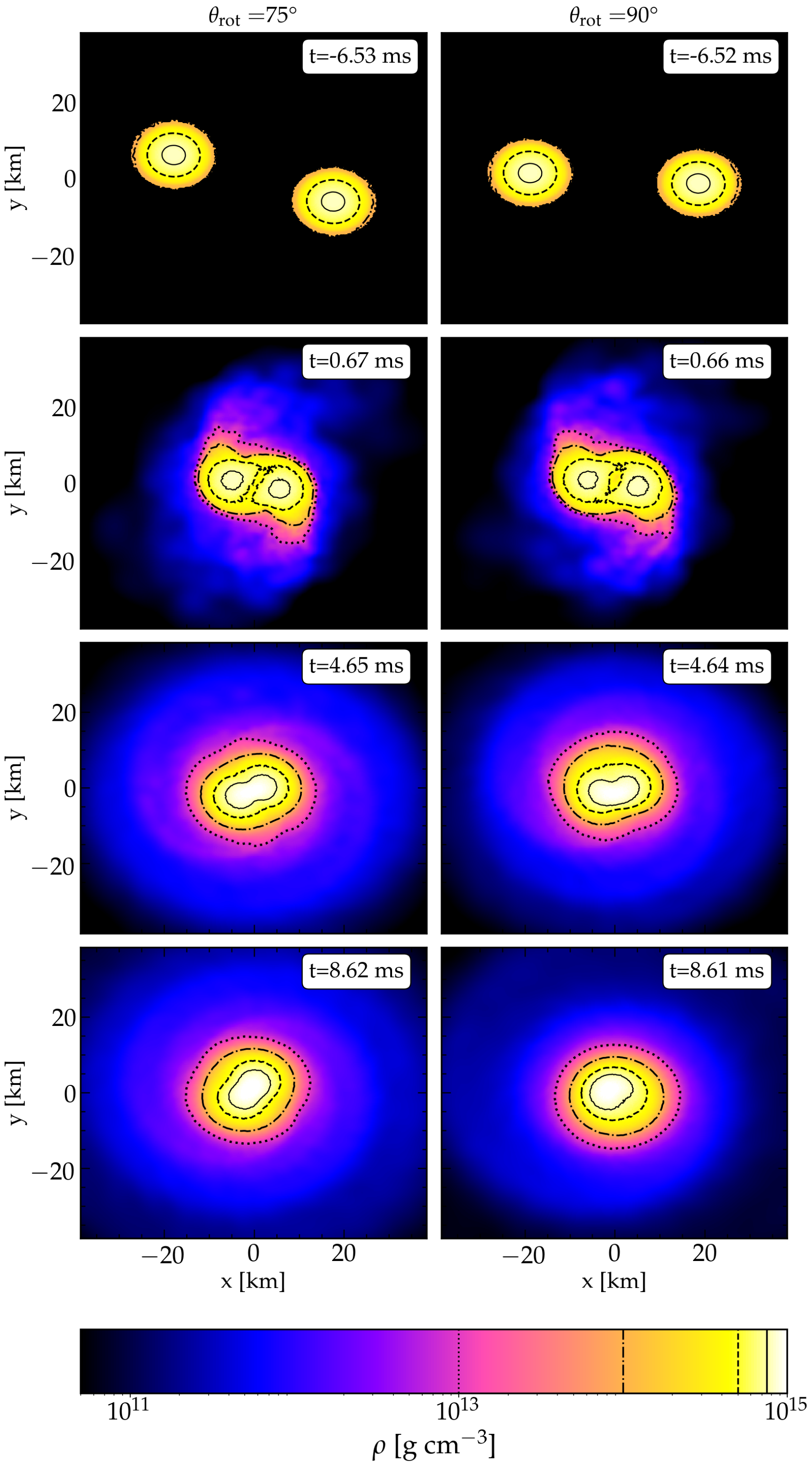

Figure 3.8.: density distribution at different times compared between two simulations (left 75°-simulation, right 90°-simulation).

In both simulations the bar shaped core is visible, but one can see that the double core in the left panel is more symmetric while in the right panel the core is more bean-shaped with a slight bulge of opposite curvature forming in the layer around it. In the panels at the last row one can see that in the left panel the double core still persists, while now one side becomes slightly bigger. In the right panel the double core broke down to a single core with an offset and a counterbalance bulge around it.

In the case of the 90°-simulation the early break of the double core structure leads to an instability in the GW signal. The forming off-center core with the counter balance bulge around it leads to an re-excitation at a slightly higher frequency. Over time the core wanders towards the center and the re-excited signal also decays.

Paschalidis et al. [169] linking in there study the one-arm instability with forming vortices from shearing during merger which move into the center of the remnant, creating an underdensity around the rotation axis. We see similar behavior in our simulations (compare upper panels of 3.8). The shearing and the Kelvin-Helmholtz instability might seed small asymmetries in the mass distribution which trigger the one-arm instability. This could explain why for lower resolution the spread in ejecta mass is smaller since in these cases is the Kelvin-Helmholtz instability more poorly resolved. Since we point out that shock heating and shearing and the Kelvin-Helmholtz instability may play a role in the divergence of the ejecta mass, we need also to look into the treatment of artificial viscosity of our setup. We conduct a first test of our artificial viscosity scheme in Appendix C.

In this chapter we conducted the first study to explore fluctuations in the evolution of BNSM. While the tests we conducted are not conclusive, we could give the first indications that stochastic fluctuations in BNSM might exist. We did not see a clear correlation to resolution effects, which would indicate that the stochasticity is mainly numerical. We see that the evolution of the ejecta is very sensible to the evolution of the remnant core structure. This makes it plausible that small seed perturbations could lead to different outcomes.

However, wether the observed stochasticity in simulations is a real physical effect or has just a numerical cause, we could show that it is important to take this uncertainty into account when it comes to drawing conclusions from simulations.

4. Evolution of ejecta

The goal of this chapter is to present the adjustments we have made for BNSM simulations in the SPH code to improve the description of the ejecta. Specifically, we address the problem of artifacts that are caused by poor resolution, such as negative internal energy, and make the evolution of the hydrodynamic quantities more resilient against it. This allows to simulate the ejecta over longer times with more meaningful results.

For long-term simulations, the EoS must cover the relevant density and temperature regime in addition to a robust development of the hydrodynamic quantities. The range of interest can be for densities from above nuclear saturation density and temperatures of several tens of MeV to densities and temperatures of interstellar medium ($10^{-10}\,\mathrm{g\,cm^{-3}}$, 10 K). For the simulations we use the SFHO EoS [144], which uses the statistical model [186] for EoSs of Hempel and Schaffner-Bielich. In this approach matter consists of nuclei, nucleons, electrons, positrons and photons. Electrons and positrons are described as a general Fermi-Dirac gas. The Fermi-Dirac integrals are calculated with high precision for electrons and positrons as well as for nucleons to take possible degeneracy fully into account. At high densities for interacting nucleons is a relativistic mean field model applied. At number densities below $10^{-5}\mathrm{fm}^{-3}$ ($\sim 10^{7}\,\mathrm{g\,cm^{-3}}$) interactions become negligible and nucleons are treated as non-interacting ideal Fermi-Dirac gases. Nuclei can form below nuclear saturation density and treated as non-relativistic Boltzmann gas. While SFHO already covering a wide range of parameter space, its main focus is on nuclear matter properties. The lower limits of $1.6 \times 10^{3}\,\mathrm{g\,cm^{-3}}$ in density and 0.1 MeV in temperature, while for most astrophysical applications adequate, are insufficient for long-term evolution of BNSM ejecta. That is why we need to extend the EoS table. Section (4.1) will explain the employed scheme to do that.

In section (4.2) we will focus on improving the hydrodynamical evolution of the ejecta. While the ejecta is expanding, the resolution is decreasing. At low resolution the errors of the employed numerical approximations can become large and impact the evolution. We will test a alternative discretization of the GRHD equations which improves the robustness of the evolution of the ejecta even at low resolution. To see how much resolution impacts the ejecta we run simulation with different numbers of SPH particles for both discretizations and make comparisons in section (4.3). With the extended EoS and the new implemented discretization we run a long-term simulation up to 275 ms after merger. Results from this simulation will be shown in chapter (5).

4.1. Extension of the equation of state

The extension of the EoS table is for regions of low rest-mass density in the parameter space. Therefore treating baryonic matter as a Boltzmann gas will be sufficient for a consistent extension. Under this condition we need for a given ρ, T and Y_e to compute the total energy per nucleon

$$E_{\text{tot}} = \sum_i Y_i m_i + \frac{3}{2} \sum_i Y_i k_B T + E_e + E_\gamma + E_C, \tag{4.1}$$

where Y_i is the number fraction of each species i of nuclei and nucleons, and their corresponding baryon masses m_i, E_e is the energy contribution from electrons, E_γ the energy contribution from photons and E_C is the Coulomb energy contribution. The first term is the rest mass contribution which depends on the composition of the baryonic matter. First tests trying to use a second EoS table for low densities showed that the assumed composition is important. Using two tables resulted in differences of internal energies for the same ρ, T and Y_e. Consequently, the discontinuity caused the recovery scheme of the primitive variables to fail to converge. For this first test we used the EoS from [60], which was used in their study for a Black Hole Torus system and its outflows. This EoS assumed for the composition just four species: neutrons, protons, ^{4}He and one representative nucleus ^{54}Mn.

Although employing a second table with a assumed composition of four species was ineffective, this does not imply that a fully detailed composition is required for a continuous extension of the EoS table. One approximation which could be made is to average over all species of nuclei. The number fractions is defined by

$$Y_i = \frac{n_i}{n_B} = \frac{X_i}{A_i}, \tag{4.2}$$

where X_i is the mass fraction of the species and A_i. Due to normalization $\sum Y_i A_i = 1$ can the number fraction be expressed just by the average amount of nucleons per nucleus

$$\bar{A} = \frac{\sum Y_i A_i}{\sum Y_i} = \frac{1}{\sum Y_i}. \tag{4.3}$$

With that the second term, the thermal energy contribution can be computed by

$$\frac{3}{2} \sum_i Y_i k_B T = \frac{3}{2} \frac{1}{\bar{A}} k_B T. \tag{4.4}$$

Already by using this approximation and treating electrons as a Fermi-gas it is possible to get the thermal and the electron contribution. The Coulomb contribution is mostly negligible in the parameter space where the ejecta are evolving. We can now at a boundary of the parameter space of SFHO EoS calculate the thermal and electron contribution. We define the difference between the tabulated energy and our calculated energy as the missing rest-mass contribution. By this construction the internal energy will match exactly.

We assume that the composition will stay constant for lower densities and temperatures, and use the same rest mass contribution as for the edge case. To calculate the thermal and electron contribution we use the Timmes EoS [187]. The EoS presumes that the described matter is composed of a photon gas in local thermodynamic equilibrium, along with a Boltzmann gas of nuclei and a Fermi-gas containing electrons and positrons. The EoS uses a precise quadrature schemes from [188] to solve the generalized Fermi-Dirac integrals to describe the Fermi-gas. The input parameters are the temperature, density, average nucleon count per isotope $\bar{A}$, and the average charge per isotope $\bar{Z}$, which is provided by SFHO and used in the extension. It outputs pressure, specific thermal energy, along with various other hydrodynamic quantities. This treatment for matter is very similar to SFHO at low densities.

The SFHO table covers the following ranges. The mesh for baryon number density is defined by

$$n_B = 10^{-12} \times 10^{0.04(k-1)}\,\mathrm{fm}^{-3} \text{ with } k = 1, \dots, 308 \tag{4.5}$$

which corresponds to a rest mass density between 1.6×10^3 and $3.2 \times 10^{15}\mathrm{g\,cm}^{-3}$ respectively using Eq. (2.40). The temperature range is

$$T = 0.1 \times 10^{0.04(i-1)}\,\text{MeV with } i = 1, \dots 81. \tag{4.6}$$

We extend the mesh, while keeping the same definition but extending the range of the indices. The baryon number density index k ranges then $k = -517, \dots, 308$ which correspond to a minimal rest mass density of $1.9 \times 10^{-9}\mathrm{g\,cm}^{-3}$, while the temperature index i ranges from $i = -160, \dots, 81$, which corresponds to a minimum temperature of 3.9×10^{-8} MeV ($\sim$ 500 K).

Figure (4.1) shows for a given temperature and rest mass density the extension of internal energy and pressure. The gray line indicates the lower bound of the original SFHO table. The upper panels show the extension of internal energy. Since for very low densities and temperatures the rest mass contribution dominates (see discussion in (2.3.1)), the rest mass contribution ϵ_0 is subtracted. We define ϵ_0 as the internal energy at the minimum temperature for a specified rest mass density, which corresponds to the missing contribution at that match of the two EoS. The upper left panel shows the extension towards lower temperatures for a wide range of rest mass densities. The upper right panel shows the extension towards lower rest mass densities over a wide range of temperatures. In both cases the EoS extends smoothly with our procedure. The assumption that the composition stays constant over the lower range of temperature and rest mass density seems appropriate, as changes in rest mass contribution would show a visible change in internal energy. Over those temperatures the r-process will take place that changes the composition. However, we neglect this energy production here.

The lower panels show the pressure over density (left) and temperature (right). The values are in very good agreement as a continuous extension. We chose for all four panels rest mass density an temperature ranges which are relevant for the long time evolution of BNSM ejecta. The ejecta contains a significant amount of free neutrons. As we are not taking neutrinos into account, the ejecta remains highly neutron-rich, with

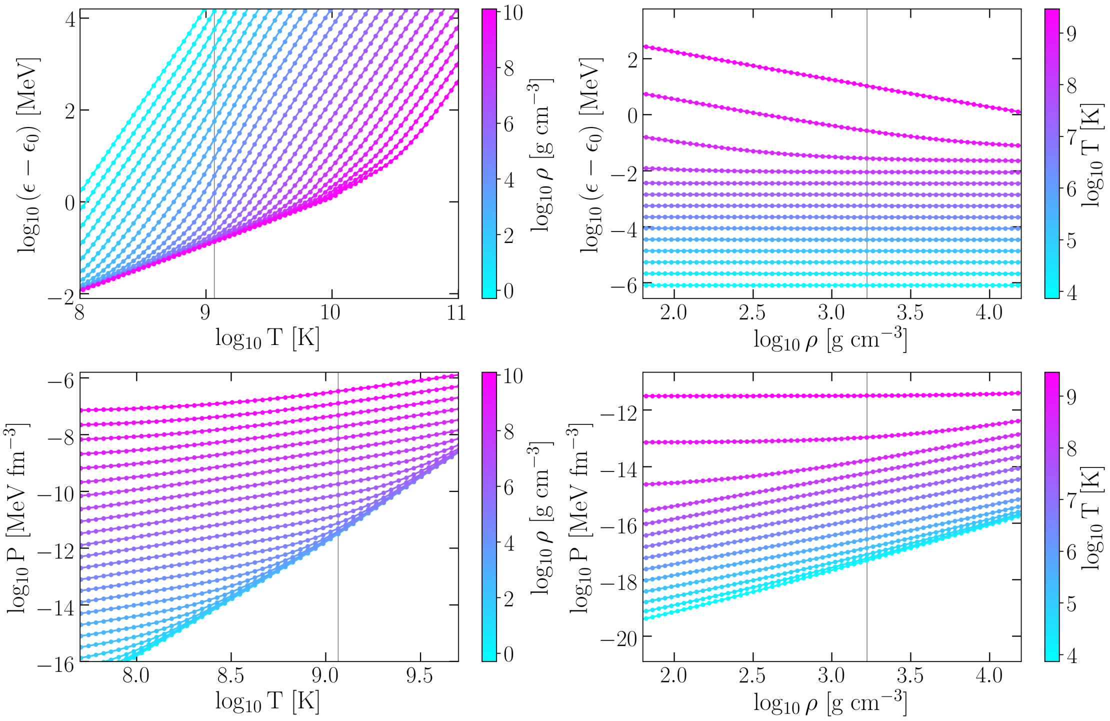

Figure 4.1.: Extension of EoS table in internal energy ϵ and pressure P in rest mass density ρ and temperature T. Upper left: internal energy over temperature for different rest mass densities. Upper right: internal energy over rest mass density for different temperatures. Lower Left: Pressure over rest mass density for different temperatures. Lower Right: Pressure over temperature for different rest mass densities. For all plots a electron fraction $Y_e = 0.02$ was chosen. For a better visibility only every tenth row of temperature (density) of the showed range is plotted. The dots are the tabulated values. Grey vertical line shows where the extension of the EoS starts.

$0.01 \leq Y_e \leq 0.06$. Since we assume a Boltzmann gas, the extension to lower temperatures is only applicable for low densities. At some point degeneracy effects will get non-negligible for neutrons. These can be estimated with the degeneracy parameter

$$\eta = \frac{\mu - m}{T}, \tag{4.7}$$

with μ the chemical potential including rest mass m. A system is "non-degenerate" when $(-\eta) \gg 1$, while it is "highly degenerate" for $\eta \gg 1$. Apart from these two extreme cases, degeneracy effects become significant near $\eta \simeq 0$. We checked for a temperature of 0.1 MeV at which density $\eta = -1$ and how pressure and other quantities are effected at this points. We recognized that above $10^9\,\mathrm{g\,cm^{-3}}$ degeneracy effects become apparent and above $10^{10}\,\mathrm{g\,cm^{-3}}$ the differences between Timmes EOS and SFHO are greater than 2 %. This was decided to be the upper limit for the extension. We could extend Timmes EOS to allow degenerate nucleons , but we decided against it. Even if we considered degeneracy we would only increase the upper limit but still not be able to extend the temperature for the whole density range, since at even higher densities nucleon-nucleon interactions need to be considered.

However extending not over the full density range has a drawback for using the EOS table in the SPH simulation. Since now the table is no longer symmetric in all three parameter ranges. While for high densities the lowest temperatures will be still 0.1 MeV. A switch has to be implemented into the code to allow lower temperatures for the ejecta in the simulation as soon as they reach densities where the baryonic matter can be treated as Boltzmann gas. This is not a trivial task since as mentioned in section (2.3) the primitive quantities are calculated by an iterative numerical scheme. Switching between possible temperature ranges (and with that internal energy) is a high non-linearity which can lead to non convergence and failing the primitive variable recovery. Therefore deciding the allowed temperature range before the recovery scheme is better to avoid this problem. To do this, the rest mass density needs to be estimated before calculated in the recovery scheme. As a criterion we use

$$\frac{\rho^*}{\psi^6} = \rho \cdot W \approx \rho. \tag{4.8}$$

This is an estimated upper limit for the rest mass density before the density and the Lorentz factor are recovered, since W is bigger or equal one. As soon as this upper limit reaches a rest mass density of $3.14 \times 10^9 \mathrm{g\,cm}^{-3}$, we allow the recovery scheme to consider lower temperatures. We put in the table lower temperature extension up to a rest mass density of $10^{10} \mathrm{g\,cm}^{-3}$ as leeway for the iterative recovery scheme.

With that, the EoS covers now the necessary density and temperature ranges for long-term simulations. In the next section we will take a closer look into the hydrodynamic evolution of the ejecta.

4.2. Evolution of the energy per nucleon

In section (2.2) we described the employed variables (2.24)-(2.26) that are evolved in the GRHD equations (2.27)-(2.29) and in section (2.3) the numerical scheme that is used to calculate the primitive variables rest-mass density ρ, coordinate velocity v^i, and specific internal energy ϵ. Other quantities, such as pressure and temperature are in this scheme evaluated by using the EoS table for the evaluated primitive variables. A trilinear interpolation is used to find for given rest-mass density ρ, electron fraction Y_e and specific internal energy ϵ the matching pressure and other quantities of the EoS.

One problem that occurs mostly in regions of the outflowing ejecta, is that the recovery of the primitive variables starts to fail. The energy per nucleon τ falls below the minimum physical value and the inversion to the specific internal energy ϵ produces nonphysical values. In cases where the recovery produces nonphysical values for ϵ the trilinear interpolation to find the matching pressure and temperature just uses the minimal value ϵ in the tabulated EoS. This also has an impact on the further evolution of the SPH particle, since the evolution equations(2.28) and (2.29) uses the recovered pressure. To check for how many SPH particles in the ejecta this occurs we run a simulation of 1.35-1.35 $M_\odot$ BNSM up to 25 ms after merger. In the test simulation are 339×10^3 particles, from which 4.0×10^3 got ejected. At 25 ms after merger 0.72×10^3 particles, which is roughly 18% of the ejecta, suffer from this problem. This can have an impact on the global properties of the ejecta, including the spatial, velocity, and temperature distributions of the ejecta. These are important information for nucleosynthesis and radiative transfer calculations to predict r-process yields and kilonovae light curves.

To improve this, we should first understand how the energy per nucleon τ should evolve for an outflowing SPH particle. While a mass element gets ejected of the system, the gravitational and pressure forces and the temperature will steeply decrease. When the particle reaches asymptotically constant velocity the pressure gets negligible and the enthalpy $h = 1 + \epsilon + P/\rho$ converges to $h \approx 1 + \epsilon_0$, where ϵ_0 is the specific internal energy at zero temperature. The total energy per nucleon

$$\tau^0 = hW - \frac{p}{\rho W} - 1, \tag{4.9}$$

should therefore converge to

$$\tau^0 \approx (1 + \epsilon_0)W - 1. \tag{4.10}$$

The energy per nucleon,

$$\tau = hW - \frac{P}{\rho W} - \omega, \tag{4.11}$$

which is the variable evolved in the code, has an additional term subtracted, which accounts for kinetic energies [42]. The additional term can be expressed as

$$\omega = \sqrt{1 + \frac{u^2 h^2}{\psi^4}} = \sqrt{1 + (W^2 - 1)h^2} \approx \sqrt{1 + (W^2 - 1)(1 + \epsilon_0)^2}, \tag{4.12}$$

with u^2 the 4-velocity squared. How it behaves for outflowing particles can be estimated by a Taylor expansion around $\epsilon_0 \to 0$ up to the first order. With

$$\sqrt{1 + (W^2 - 1)(1 + \epsilon_0)^2} \approx W + W\epsilon_0 - \frac{\epsilon_0}{W}, \tag{4.13}$$

we can now estimate that τ should converge to

$$\tau \to (1 + \epsilon_0)W - (1 + \epsilon_0)W + \frac{\epsilon_0}{W} = \frac{\epsilon_0}{W}. \tag{4.14}$$

In low Y_e regions as shown in Figure (2.1) $\epsilon_0 \cdot m_u$ can be up 7 MeV per nucleon due to rest mass contributions and while most of the ejected particles have a velocity below $0.3c$, which corresponds to a Lorenz factor of $W < 1.05$. Thus the energy per nucleon energy should asymptotically evolve roughly to this minimum of 7 MeV per nucleon. Through the example of a single trajectory of an ejected SPH particle we can look how ejected particles behave in the simulation.

Figure (4.2) shows the energy per nucleon τ, the internal energy ϵ, the internal energy at zero temperature ϵ_0 and the corresponding density, pressure and velocity over time. The particle gets accelerated during the merger up to a velocity of $0.4c$ within half of a millisecond. At 0 ms the density, pressure, and the energy per nucleon τ are decreasing rapidly. As it is flying outwards, it decelerates while overcoming the gravity of the remnant. At 0.2 ms after merger the particles internal energy ϵ falls below the minimum ϵ_0 indicated by the red line in the upper left panel. While it moves outwards it is hit by a shock front from a spiral arm. At 0.6 ms after merger energy, pressure density and velocity are increasing for a short amount of time. After it flies beyond the spiral arm the energy falls again below the minimal internal energy ϵ_0. The point is marked with a gray vertical line in all panels. From this point onward the energy keeps decreasing.

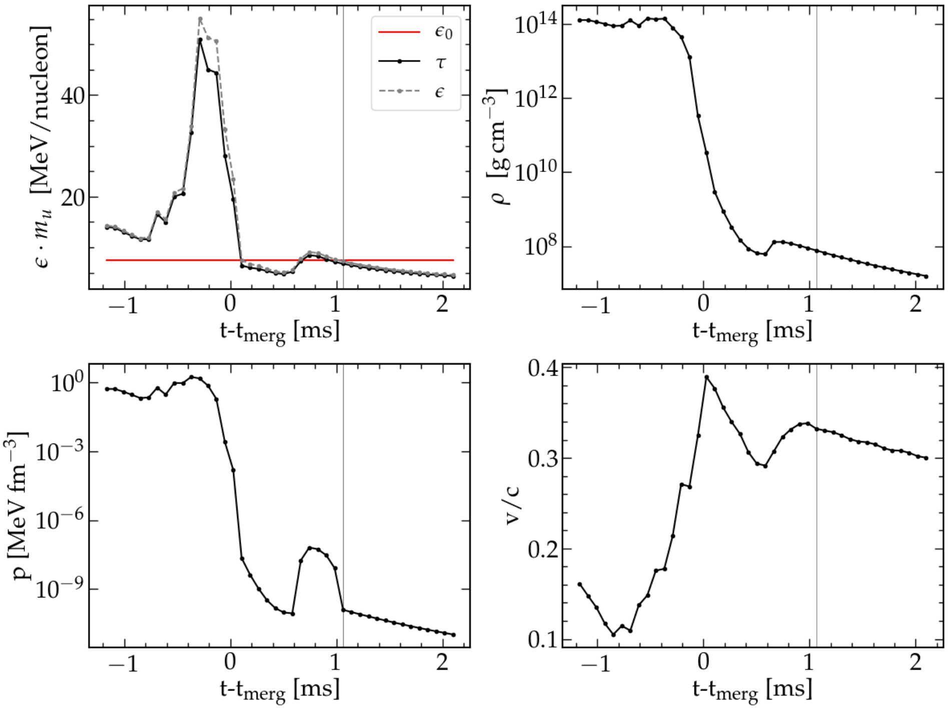

Figure 4.2.: upper left: temporal evolution of energy per nucleon τ and the corresponding internal energy ϵ of a single ejected SPH particle. The red line shows the minimum internal energy ϵ_0 in the EoS table. At 1.0 ms after merger the energy per nucleon evolves below ϵ_0 and decreases until it reaches zero, which is indicated by the gray vertical line. upper right: corresponding density of the ejected SPH particle. After it gets ejected the density decreases over several orders of magnitude in 2 ms. lower left: evolution of the particles pressure, after 1.0 ms it is the minimal pressure for the given density. lower right: evolution of the velocity. The particle accelerates gets ejected and decelerates slightly while it overcomes the remnants gravity

ϵ_0 is virtually constant even if the density is decreasing over several orders of magnitudes, like the upper right panel is showing. Since neutrinos were not taken into account in this simulation the electron fraction of the particle remained constant at $Y_e = 0.02$, which the parameter ϵ_0 is quite sensitive to, as (2.1) showed. The internal energy ϵ should asymptotically approach ϵ_0. The difference $\epsilon - \epsilon_0$ is the thermal energy which should decrease over time. Following eq. (4.14), the energy per nucleon $\tau \cdot m_u$ in the upper left panel, as the velocity of the particle approaches $0.3c$, which corresponds to a Lorentz factor of 1.05, should just staying slightly below ϵ_0 at a value of 6.6 MeV per nucleon. One can see that in general the recovery of the thermal energy is challenging for the cooling ejecta, because the thermal energy gets very small compared to the binding energy contribution. Instead of staying around ϵ_0, τ is just crossing this limit and evolving towards zero, without any sign to recover back to physical values.

As a consequence, the recovery scheme fails and the minimal pressure of the EoS is assigned to the particle, which impacts also energy and momentum evolution from that point onward. Since the mass element crossed the minimum energy ϵ_0, its thermal energy is negative. The recovery scheme just assigns the minimum temperature and the EoS extension in temperature can not be used. Mass elements and their trajectories which are facing this issue are unusable for nucleosynthesis calculations, since temperature and internal energy are for that essential quantities.

The example makes clear that already parts of the dynamical ejecta at early times facing this problem of evolving into nonphysical regimes. To understand why this is happening, we will take a closer look at the energy equation, its individual terms, and how it is discretized in the SPH code.

4.2.1. Discretization

The right-hand site of energy equation has 5 terms

$$\frac{d\tau}{dt} = \mathcal{A} + \mathcal{B} + \mathcal{C} + \mathcal{D} + \mathcal{E}, \tag{4.15}$$

with

$$\mathcal{A} = -\psi^6 \frac{P}{\rho^*} \partial_i \left(v^i + \beta^i\right) \tag{4.16}$$

$$\mathcal{B} = -\frac{\psi^6}{\rho^*} \left(v^i + \beta^i\right) \left(1 - \frac{hW}{\omega}\right) \partial_i P \tag{4.17}$$

$$\mathcal{C} = -6\psi^5 \frac{P}{\rho^*} \left(v^i + \beta^i\right) \partial_i \psi \tag{4.18}$$

$$\mathcal{D} = -\frac{\hat{u}_i}{\psi^4} \left(1 - \frac{hW}{\omega}\right) \partial_i \alpha \tag{4.19}$$

$$\mathcal{E} = +\frac{1}{\psi^4} \left(\frac{1}{hW} - \frac{1}{\omega}\right) \left(\hat{u}_i \hat{u}_j \partial_j \beta^i - \frac{1}{3} \hat{u}_i \hat{u}_i \partial_j \beta^j\right). \tag{4.20}$$

We will now look into how the individual terms contribute to the evolution of energy per nucleon, on the same example particle as in the section before. The left panel of figure (4.3) shows $\frac{d\tau}{dt}$ and its individual terms over time. We did not include the viscosity term which can only increase τ. Around 0.6 ms after merger on can see that $\frac{d\tau}{dt}$ is greater than the sum of the individual terms. This is because the viscosity contribution. The right panel shows how τ and ϵ evolves over time. As the particle gets ejected the terms $\mathcal{C}, \mathcal{D}$, and $\mathcal{E}$ that account for the change in the metric terms $\partial\alpha$, $\partial\beta$ and $\partial\psi$ are decreasing and become negligible since the particle is leaving the strong gravity field of the remnant. While the pressure is rapidly decreasing the pressure gradient term $\mathcal{B}$ is also decreasing. The divergence of velocity in general does not need to vanish, but since the term $\mathcal{A}$ includes also the pressure, it also should evolve towards zero. While we see that trend the divergence of velocity term $\mathcal{A}$ still dominates and leads to a rapidly decreasing energy per nucleon. Even after 1 ms after the merger when ϵ is below ϵ_0 the term $\mathcal{A}$ does not vanish. Energy is expected to decrease during the ejection but this fast evolution to nonphysical energies indicates that the divergence of velocity term $\mathcal{A}$ in $\frac{d\tau}{dt}$ is overestimated.

We will look into the discretization of this term in the SPH code. In section (2.2.1) we showed the current implementation of the discretization of the pressure gradient and divergence of velocity in the energy per nucleon evolution:

$$-\psi^6 \frac{P}{\rho^*}\partial_i\left(v^i+\beta^i\right) \overset{disc.}{\approx} \psi_a^6 \sum_b \frac{M_b}{2}\left(\frac{P_a}{\rho_a^{*2}}+\frac{P_b}{\rho_b^{*2}}\right)\left[(v_a^i+\beta_a^i)-(v_b^i+\beta_b^i)\right]\nabla_a \mathcal{W}_{ab}. \qquad (4.21)$$

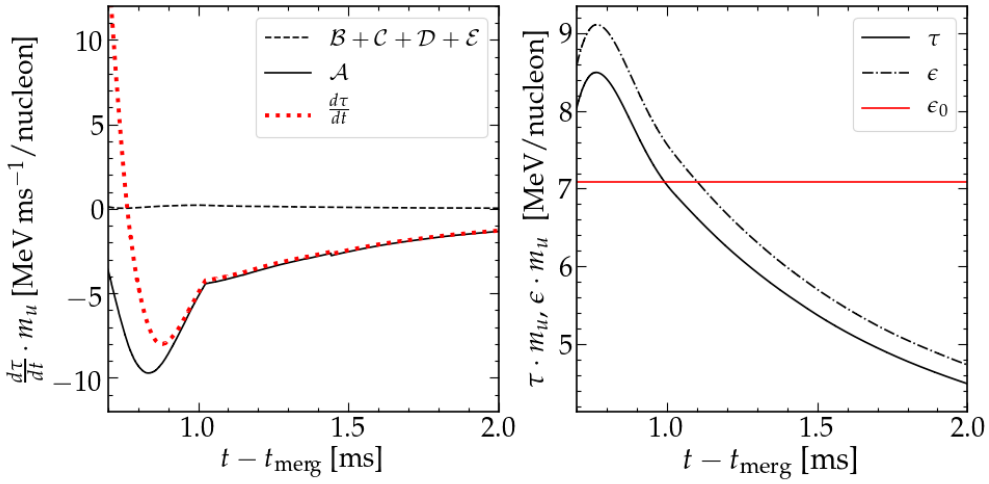

Figure 4.3.: Left: individual terms of the time derivative from the energy per nucleon $\frac{d\tau}{dt}$ and total $\frac{d\tau}{dt}$ over time of a ejected particle. Right: resulting energy per nucleon τ as well as internal energy ϵ over time.

This discretization uses a pair-wise symmetrization with arithmetic means for the pressure. Symmetrization in discretization is typically used for conservation of quantities in SPH, for example momentum. This approach guarantees that the momentum lost by particle a is transferred to particle b, thereby conserving the total momentum. However, as Springel and Hernquist pointed out [137], there is no compelling need to distribute pressure work done by a particle pair equally between them.

As shown in section (2.2.1) symmetrization was in the SPH code also used to combine term $\mathcal{A}$ and $\mathcal{B}$ together. Another possibility is to use eq. (2.36) to discretize the divergence of velocity without symmetrization. With this non-symmetric discretization we get instead of eq. (2.39) now

$$
\begin{aligned}
&-\psi^6 \frac{P}{\rho^*}\partial_i\left(v^i+\beta^i\right)+\frac{\psi^6}{\rho^*}\alpha\left(v^i+\beta^i\right)\left(1-\frac{hW}{\omega}\right)\partial_i P \overset{disc.}{\approx} \\
&\psi_a^6 \sum_b M_b \left\{\left(1-\frac{hW}{\omega}\right)\left(\frac{P_b}{\rho_b^{*2}}+\frac{P_a}{\rho_a^{*2}}\right)\left(v_a^i+\beta_a^i\right)-\frac{P_a}{\rho_a^{*2}}\left[\left(v_a^i+\beta_a^i\right)-\left(v_b^i+\beta_b^i\right)\right]\right\}\nabla_a \mathcal{W}_{ab} \\
&=\psi_a^6 \sum_b M_b \left\{\left[\frac{P_a}{\rho_a^{*2}}\left(v_b^i+\beta_b^i\right)\right]+\left[\left(\frac{P_a}{\rho_a^{*2}}+\frac{P_b}{\rho_b^{*2}}\right)\left(1-\frac{hW}{\omega}\right)-\frac{P_a}{\rho_a^{*2}}\right]\left(v_a^i+\beta_a^i\right)\right\}\nabla_a \mathcal{W}_{ab}.
\end{aligned}
\tag{4.22}
$$

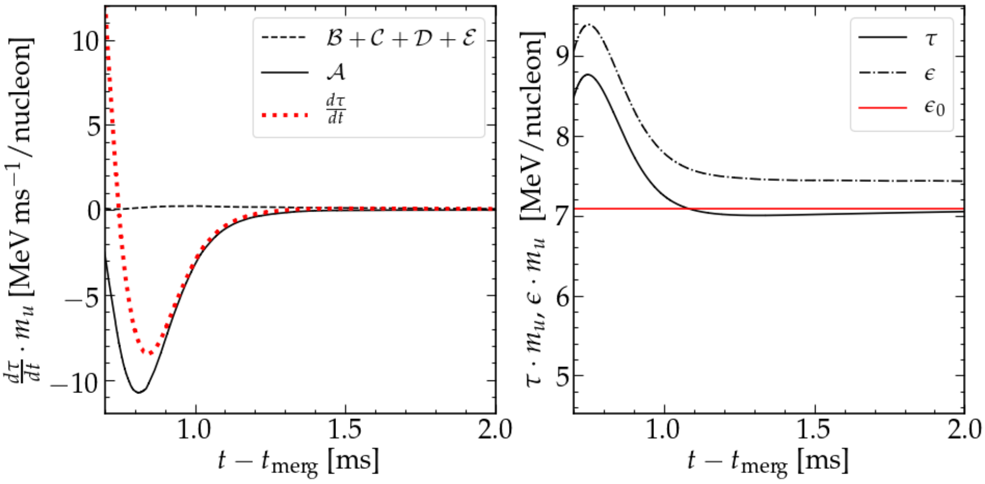

Figure 4.4.: pressure gradient term and divergence of velocity term of the time derivative from the conserved energy over time after changing the discretization. Right: conserved energy τ and internal energy ϵ over time. After minimal pressure of the EoS is reached τ stops to decreasing and ϵ decreases asymptotically to the EoS minimum.

Benz discussed already for the Newtonian case in [189] that the disadvantage of the symmetrized discretization is that it can lead to non-physical solutions like negative internal energies and temperatures. A practical way to understand this is by recognizing that the pressure work of a particle is influenced by the pressure P_b of its neighboring particles b. This is the reason why the divergence of velocity term is overestimated.

It also implies that, because the total energy is conserved and the evolution with this discretization tends to underestimate the internal energy, it overestimates the kinetic energy of the ejecta. Benz showed that the non-symmetrized discretization still conserves total energy.

In the Newtonian case this discretization is frequently used for the derivative of the internal energy instead of the symmetrized form [137, 190–199]. Couchman et al. showed that the non-symmetrized discretization produces less scatter in entropy [194]. Springel and Hernquist investigated different SPH formulations under conditions of poor resolution and strong explosions and showed that the non-symmetrized discretization is preferable since it avoids artifacts from nonphysical behavior [137].

These studies used Newtonian hydrodynamics and focused mainly on physical systems such as gas cloud collapse and star and galaxy formations. We test now if the non-symmetrized discretization also in the general relativistic case show improvements and improve the evolution of the ejecta of BNSMs.

We want to point out, that we focus on the long term evolution of the dynamical ejecta, which is less then 1 % of the mass of the system but contains all particles which are reaching non-physical regimes. Studies which focus more on the remnant, for example, the formation of hyperons or quark gluon plasma and their impact on gravitational waves may not be impacted by this problem since the system reaches high temperatures through shock and viscous heating and it may be insignificant to have less accurate ratio between internal and kinetic energy. Changes in the ejecta velocity, temperature and entropy might have a significant impact on nucleosynthesis network calculations and resulting kilonova light curves.

We restarted the test simulation at the time of merger after applying the changes, and figure (4.4) shows the impact on the same particle we used for figure (4.3) on the $\frac{d\tau}{dt}$ terms on the left side and on the evolution of the energy per nucleon and internal energy on the right side.

The divergence of velocity term is at 1.0 ms after merger decreases faster towards zero. The particle gets ejected promptly and density and pressure declines very rapidly. In poor resolution, this can lead to particles which still fall below the minimum energy of the EoS for a given density and electron fraction. But in this case as seen around 0.8 ms after merger the divergence of velocity terms also drops and $\frac{d\tau}{dt}$ becomes small and the energy per nucleon τ stays consistent with the EoS. While in highly dynamical regions still some particles overshoot the minimal energy of the EoS, the prevention of overestimation of the divergence of velocity term improves the problem. Figure (4.5) shows the relative amount of SPH particles which are below the minimal energy of the EoS for a given density and electron fraction. The dashed line shows the impact of the changed discretization which halves the amount of particles in the ejecta with non-physical energies. Now only around 5 % of the ejecta faces this issue. Additionally particles which are reaching the non-physical regime recover over time or stay approximately near the lower limit instead of for drifting away.

In the next section we will have a closer look on the impact of the change in discretization on the ejecta dynamics.

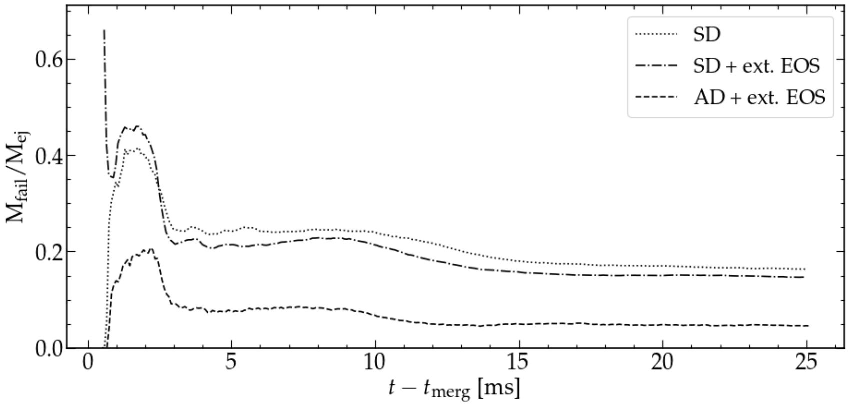

Figure 4.5.: The relative amount of SPH particles in the ejecta where the recovery scheme fails. Dashed line shows how the changed discretization of the divergence of velocity improved the evolution of the ejecta. Upper figure: relative to the total ejecta mass, lower figure: relative to the total amount of ejected particles.

4.2.2. Impact of discretization on ejecta evolution

To explore the impact of the choice of discretization we setup two simulations. The original discretization we refer to as symmetric discretized (SD) and the new implementation as asymmetric discretized (AD).

Both simulations are set with a 1.35-1.35 $M_{\odot}$ NS-NS binary system with a total number of roughly 339×10^3 SPH particles. Both use the extended SFHO EoS described earlier and also have otherwise the same setup. The only difference is the discretization of the divergence of velocity in the derivative of the energy per nucleon τ. With this setup, we ran both simulations up to roughly 60 ms after merger which is more than two times as long as before. As discussed in the last section the original discretization has the tendency to underestimate the share of internal energy in the total energy and therefore overestimates the amount of kinetic energy. This results in higher velocities of the ejecting material and a higher amount of total ejecta. Figure (4.6) shows the amount of ejecta outside a radius of 1000 km over time for both simulations. The mass ejection rate in the SD case is clearly higher, by reaching $10^{-3} M_{\odot}$ of ejecta at 60 ms (blue line), while the AD case reaches only half that value with $5 \times 10^{-4} M_{\odot}$.

We chose to look at ejecta outside of 1000 km since at this radius different ejecta criteria are converging to the same result (See appendix B) and we showed in (3.2) that stochastic effects are also smaller (see (3.1)). Compared to the variance caused by stochasticity, which was around 20 % the difference caused by using a different discretization is significant.

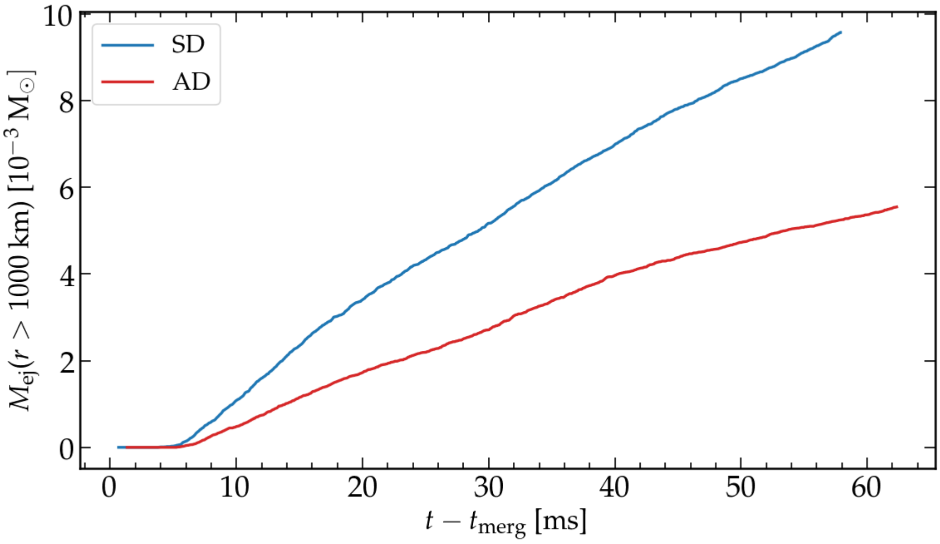

Figure 4.6.: comparison between the total ejecta of the AD and the SD simulation over time. Blue line is in the case of the original implemented symmetric discretization of the divergence of velocity in the derivative of energy per nucleon τ, red line is with the new implemented asymmetric discretization.

The total ejecta using the virial criteria (eq. (2.57)) is in both cases above $3 \times 10^{-2} M_\odot$ and are comparatively high for the typical dynamical ejecta masses of $10^{-4} - 10^{-2} M_\odot$ [83, 142, 200–203] at this time after merger. A reason for that is without any treatment of neutrinos the material does not have an effective cooling mechanism in the simulation. This leads to higher temperatures of the material outside the remnant resulting to higher thermal pressure, which pushes more material out. Thermally generated outflows leads also to more spherical symmetric ejecta.

However, the polar regions of the system still suffer the most from poor resolution, since most outflow will be ejected perpendicular to the rotation axis. There we expect a stronger impact on the ejecta. We compare the relative amount of fast ejecta ($v >$ 0.15 c) in the polar region at $\cos\theta > 0.9$ (corresponding to an opening angle of 26°). Figure (4.7) shows the evolution over time.

Shortly after the merger part of the shock heated material from the impact will eject the first material in polar direction. This material is in both cases faster than 0.15 c. Over the next 60 ms the following ejecta in the AD case is mostly slower than 0.15 c and the relative amount of fast ejecta drops fast to below 20 % and decreases steadily after and tangents to 3% at 60 ms. For the SD case the trend is similar but significant more fast ejecta is in the polar region at all times and it is still over 40% at 60 ms. Next, we will look in more detail into the differences in the velocity distribution of the ejecta.

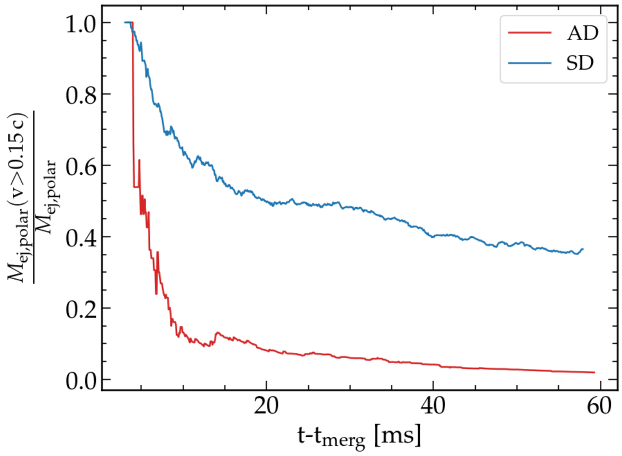

Figure 4.7.: relative amount of fast ejecta (v > 0.15 c) of the ejected mass M_{ej} in the polar regions ($|\cos(\theta)| > 0.9$) over time.

Velocity

First we have a look at the velocity distribution at the end of the simulations in figure (4.8). The velocity is in $\Delta v = 0.02\,\mathrm{c}$ bins subdivided and each bar shows the relative amount of ejecta in each velocity bin. In both simulations we see a peak at the 0.02-0.04 c bin. In the AD case this peak is more narrow and falls off first very steep up to 0.16 c and then slower until 0.7 c. In the SD scenario, the peak widens to 0.24 c, following which there is a gradual decline until 0.7 c, with a few mass elements exceeding this speed. The crossed bars show the amount of matter M_{fail} in each velocity bin which correspond to SPH particles for which the recovery scheme failed. In both cases most of the fastest particles have this problem. Nevertheless in the AD case a clear improvement is visible, especially at velocities below 0.16 c the relative amount of M_{fail} is decreasing even so the M_{bin} is steeply increasing.

This indicates a velocity dependence on M_{fail}, which would be expected as very fast ejecta tend more easily to overshoot the minimum ϵ since their more highly dynamical trajectory is less accurate resolved. One thing worth to point out is that the slowest velocity bin of <0.02 c has no SPH particles where the recovery scheme failed. In the SD case this velocity dependency is not as clear as in the AD case. While in the peak region around 0.1 c also most of the material is consistent with the EoS, the trend of M_{fail} is still increasing albeit not steeply as the M_{bin} peak.

Another point we want to emphasize here again is that even while in the AD case still a not negligible amount of SPH particles fails the recovery of the pressure there are in most cases only slightly below the minimum of the table and the discrepancy between the matching pressure $p(\epsilon)$ of the EoS and the recovered internal energy ϵ is only a few percent, while in the SD case all the SPH particles drift further away from thermodynamic consistency over time and a substantial part of them have negative internal energy ϵ.

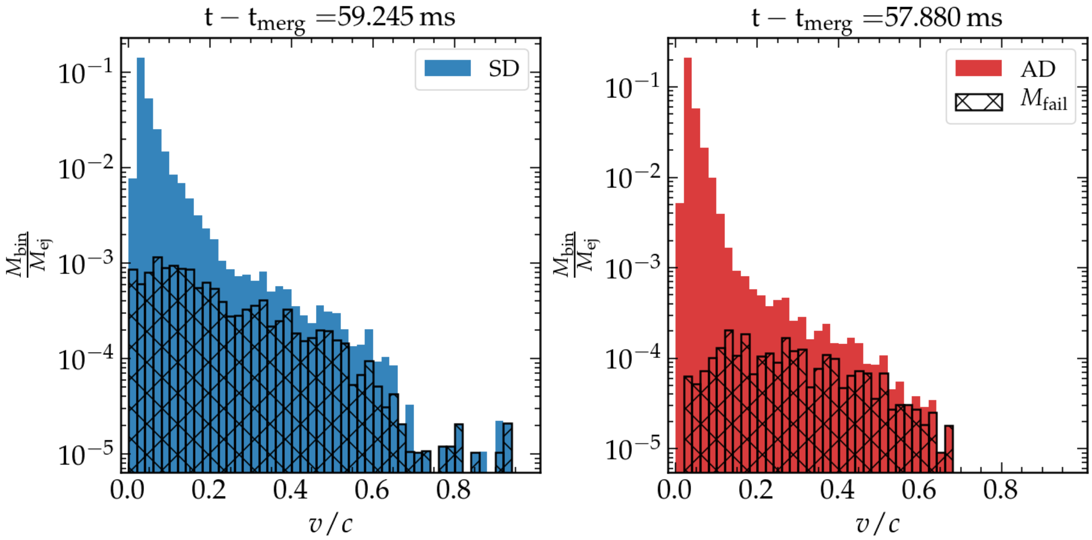

Figure 4.8.: velocity distribution of ejecta at 58 ms for both simulations. Crossed bars show the amount of matter which correspond to SPH particles for which the recovery scheme for the primitive variables failed.

In figure (4.9) we look in more detail on the angular distribution of the velocity of the ejecta. Each angle bin has an equal solid-angle with the width of $\cos\theta = 0.1$. Every angle bin is divided in velocity bins with a width of 0.02 c. The color shows how much mass is in each bin relatively to the total ejected mass M_{ej}.

We can see around 0.04 c in both cases that the peak of (4.8) is evenly distributed over the polar angle. The broader peak in the SD case comes from the fact, that at the polar region velocity distribution tends to faster velocities. There, most of the ejecta has velocities between 0.1 -0.2 c. In general we see relatively more material in higher velocities in the SD case. In both cases the fastest material is near the equatorial plane. In the AD case we see clearly less fast ejecta over the polar angles.

The velocity distribution is important for kilonova light curve calculations. Faster material gets earlier transparent, which impact how much light is emitted. Material faster than 0.2 c contributes mainly to the luminosity within the first day. Viewed from the polar region, the SD simulation would demonstrate increased luminosity at early times.

Next will have a look at the impact on the temperature and entropy, which are an important parameter for r-process nucleosynthesis.

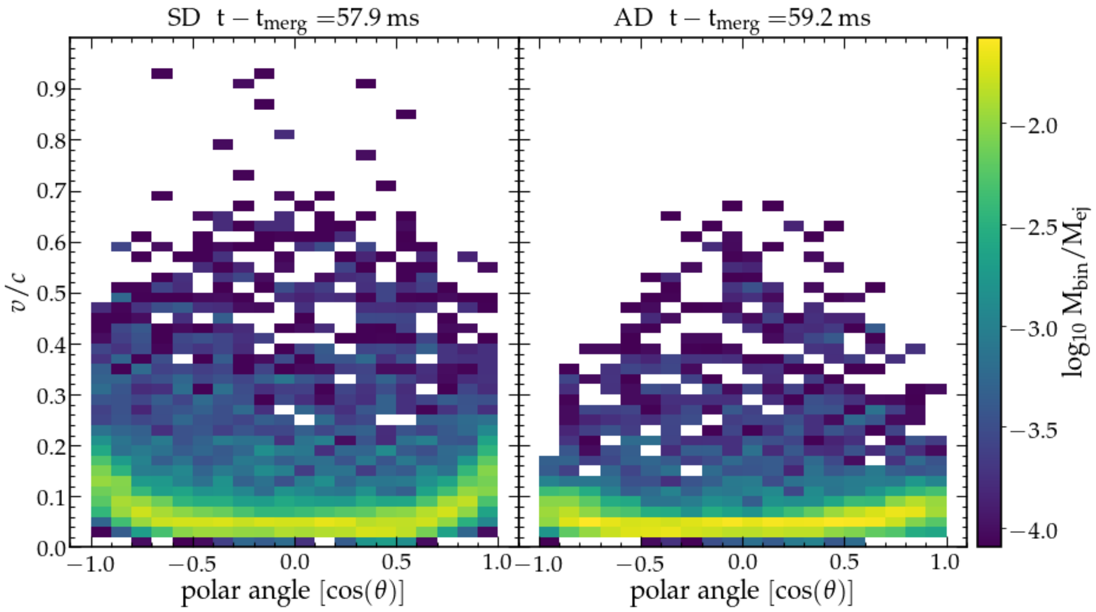

Figure 4.9.: mass distribution in velocity and polar angle bin, where each angle bin has an equal solid-angle with the width of $\cos\theta = 0.1$ and a velocity bin a width of 0.02 c. The color scale indicates how much mass is in each angle at a certain velocity.

Temperature and Entropy

In BNSM entropy is generated through shock heating or viscous heating. In our simulation the artificial viscosity increases the entropy by converting kinetic energy into thermal energy. The matter ejected by tidal forces has typically low entropy, while the ejecta components which comes from the collision interface consists of hot and high entropy matter. Furthermore, the shock heating in the disc from the formed spiral arms, which increases temperature and entropy in the disc steadily also lead to higher entropy in the disc outflows. In our code entropy is not used for the simulation, but can be extracted from the EoS using the other primitive quantities.

In figure (4.10) we look on the angular distribution of entropy of the ejecta. We show entropies between 0-100 k_b but we want to note that a few individual particles had even higher entropies (more in the SD case). In both cases most of the ejecta has entropies around 10 -20 k_b. We see that in the SD case more material reaches higher entropies than in the AD case. This is in agreement with the observation in Newtonian SPH applications [194]. Also in the AD case the higher entropies are more towards the equatorial plane, while for the SD simulation high entropy matter is more evenly distributed. Similar to the velocity distribution, we at the poles the most difference between AD and SD in entropy distribution. While in both cases the entropy interval with the most material is higher in the poles in the SD case this behavior is more pronounced. We want to point out the lowest entropy bin around 0 k_B also includes all nonphysical particles where the recovery of the primitive quantities failed. The plot shows that more particles are in the SD in this bin across all polar angles.

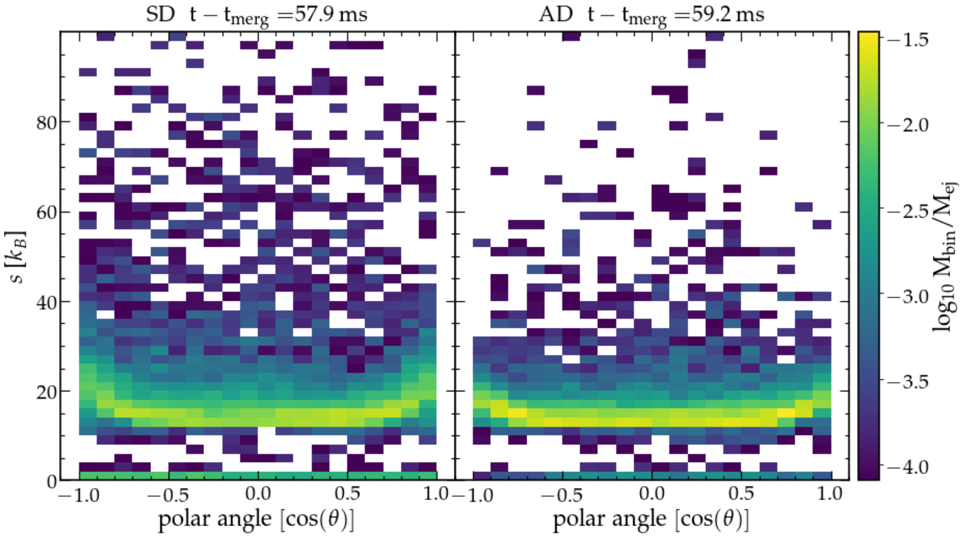

Figure 4.10.: mass distribution in entropy and polar angle bin, where each angle bin has an equal solid-angle with the width of $\cos\theta = 0.1$ and a entropy bin a width of 2 k_B. The color scale indicates how much mass is in each angle at a certain entropy.

Next we take a look on the angular distribution of the temperature in figure (4.11). Each angle bin has an equal solid-angle with the width of $\cos\theta = 0.1$ and a temperature bin with a width of 0.1 MeV. The color scale indicates how much relative mass is in each angle at a certain temperature. In both cases higher temperature is reached on the poles, but the peaks are more clear in the AD case. Most of the ejected material has temperatures below 1 MeV at that time.

Similar to the entropy plot did we include the particles which failed the recovery scheme in the lowest temperature interval 0-0.1 MeV. The SD run contains a higher concentration of particles at the poles within that interval, and across all polar angles, there is more material present in that temperature interval. In the AD case is more material above 0.5 MeV. While both have very similar peak temperature, the AD run has on average higher temperatures.

The temperature and entropy of the ejecta is highly relevant for the r-process nucleosynthesis. When the temperature drops below 1 MeV nucleons start to form the initial seed nuclei. If the ejecta are hotter, this will happen later at lower rest-mass densities. This can change the resulting element production yields, which is determined by the balance between photodisintegration and neutron captures.

In conclusion, we could show with these comparisons, that the discretization has an impact on the ejecta evolution and especially in the polar region where poor resolution is most prevalent. This would also impact nucleosynthesis calculations and the resulting kilonova light curves based on these simulations. We chose for the comparison a total particle number of 339×10^3 which was often used in previous studies [30, 143, 176, 204–206]. Of course, the impact of the discretization depends on the total particle number so in the next section we do a resolution study to see if we can reach convergence between the discretizations.

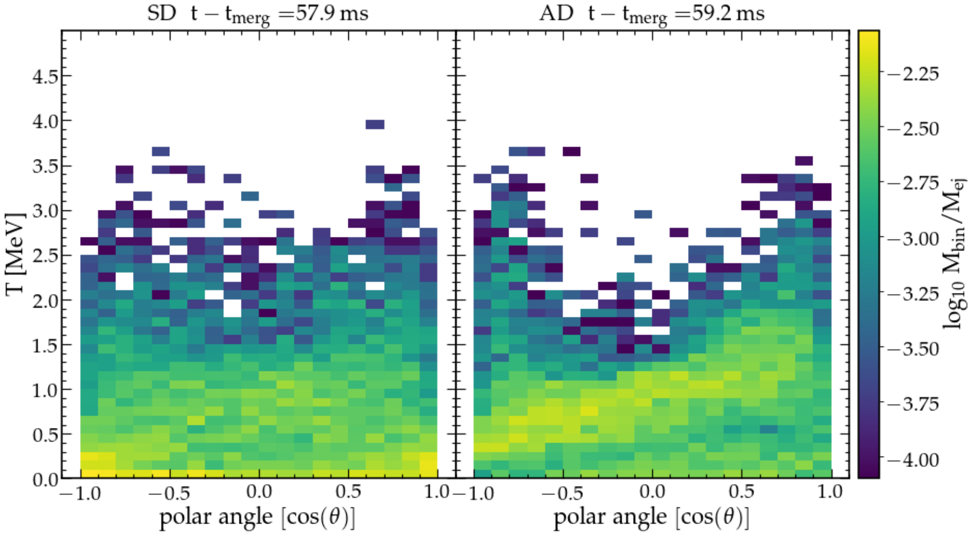

Figure 4.11.: mass distribution in temperature and polar angle bin, where each angle bin has an equal solid-angle with the width of $\cos\theta = 0.1$ and a temperature bin a width of 0.1 MeV. The color scale indicates how much mass is in each angle at a certain temperature.

4.3. Resolution study

At first we will look how sensitive the total ejecta mass over time is to the total particle number. Therefore, we conduct simulations with total particle numbers of 70×10^3, 136×10^3, 283×10^3, 339×10^3, 682×10^3 and 1420×10^3 for both discretizations. As before we look at ejecta which is outside of a radius of 1000 km from the remnant. For each simulation, Table (4.1) presents the duration until the simulation terminates, the ejecta mass in $10^{-3}\mathrm{M}_\odot$, and the count of particles N_{ej} at that time. The simulations revealed that the duration of the inspiral phase is resolution-dependent, with higher resolution runs merging at somewhat later times, even when using the same code time.

Table 4.1.: comparison of simulations with different particle numbers for both discretizations. Table shows the amount of ejecta at end of the simulation outside a radius of 1000 km.

number of particles	discretization	$t - t_{\mathrm{merg}}$ [ms]	M_{ej} $[10^{-3}\mathrm{M}_{\odot}]$	N_{ej}
1420×10^3	sym.	22.70	6.57	12917
682×10^3	sym.	24.33	5.32	3429
339×10^3	sym.	25.09	4.34	1283
136×10^3	sym.	25.65	4.17	495
70×10^3	sym.	25.95	3.64	279
1420×10^3	asym.	22.87	4.21	7518
682×10^3	asym.	24.33	3.71	2346
339×10^3	asym.	25.10	2.21	636
136×10^3	asym.	25.68	1.70	193
70×10^3	asym.	26.06	1.61	115

That is the reason why end of simulations time after merger vary around 2 to 3 ms. For this comparison we choose to run until roughly 20 ms after merger, since the higher resolution runs with 682×10^3 and 1420×10^3 particles are computational expensive and it took already several month to run up to 20 ms after merger.

There is a clear trend between total number of particles and amount of ejecta for both discretizations.

Also the difference in ejecta between the AD and the SD simulations for the same resolution decrease with higher particle numbers. While for the 70×10^3 particle runs the SD run has more than double the amount of ejecta, it is only around 50 % more in the 1420×10^3 particle run. This trend may indicate that simulation with a few million particles could already converge in terms of total amount of ejecta between this two discretizations.

The two upper panels of figure (4.12) show how the amount of ejecta outside 1000 km evolves over time for the differently resolved runs. In both cases the mass ejecting rate increases with higher resolution. Also at around 25 ms the ejection rate for the higher resolutions are steeper while especially in the AD case the lower resolution runs seem to flatten out earlier. The lower panels show the relative amount of the total ejecta for which the recovery scheme fails. In the SD case there is no clear trend between resolution and the amount of thermodynamically inconsistent particles. For all simulations the amount stays between 15% to 25%. However, in the AD case one can see that the amount of thermodynamically inconsistent particles decreases with higher resolution, as one would expect if one assumes that the reason for it is low resolution. For the highest resolution run the amount stays around only 3 % while for the lowest resolution it is around 30% at the run.

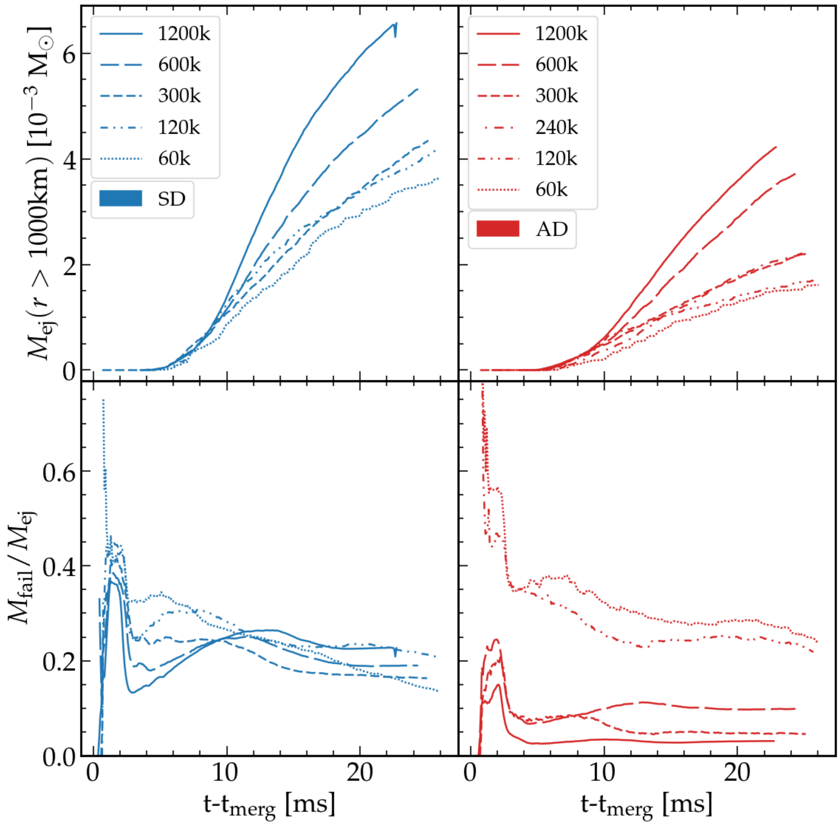

Figure 4.12.: Upper panels: comparison between total ejecta outside 1000 km over time for different total particle numbers. On the left for the symmetric discretization on the right for the asymmetric discretization. Lower panels: relative amount of ejecta for which the recovery scheme fails for different total particle numbers.

The only outlier from this trend is the 682×10^3 particle run which has a higher amount than the 339×10^3 particle run. Since none of these runs are near convergence it is expected that there is some variation, even between runs with the same set up. The reason, why the simulation 682×10^3 particle has more particles which reached nonphysical regimes than the simulation with 339×10^3 particles, could be an effect from stochasticity. How areas in the outflowing matter are resolved depends also on how the ejecta is distributed, and this can vary even within the exact same setup as we discussed in chapter (3). Nonetheless, a clear trend is recognizable.

While for very low resolution the SD simulations have less particle reaching nonphysical regimes, for higher resolution runs the asymmetric discretization is preferable since in that case the amount of nonphysical particles drops with higher resolution.

Next we take a look on the polar mass distribution changes with resolution. Figure (4.13) shows the ejected mass distributed in 20 solid angle bins, here shown in terms of $\cos\theta$. The black hatched bars show the amount of fast ejecta (v > 0.15 c). The rows show the different total particle number runs from 70×10^3 to 1420×10^3. The left column are the SD runs, while the right column are the AD runs. It shows the distribution at the end of each run, at the times stated at table (4.1). For the AD simulation one can see that the distribution is more sensitive to resolution. At low resolution the angular distribution is quite noisy and aspherical with almost no ejecta at the polar regions. The main reason is here the very low amount of ejecta.

As the resolution increases, the ejecta exhibit a trend towards a more spherical distribution. At the outer most angle bins the amount of fast ejecta to drop down, while around the equatorial plane is the relative highest amount of fast ejecta. This characteristic get less pronounced with increasing resolution. Only at the highest resolution the drop in fast ejecta occurs only on the south pole while the rest of the fast eject distribution is very evenly distributed over the polar angle. The mass distribution retains a off center peak at every resolution. For the highest resolution it has a two peak structure at $|\cos\theta| = 0.9$ with a minimum around $\cos\theta = 0.5$. Which is similar to how the mass distribution look in the SD case especially at particle numbers above 339×10^3. In general the mass distribution in the SD runs do not change drastically with higher resolution. However, one interesting change can be seen in the fast ejecta distribution. As discussed in the section before, one characteristic is that at the solid angle bins of the polar region the SD runs have a peak of fast ejecta. This can also be seen here but with increasing resolution this feature gets less pronounced and at the highest resolution it is not visible anymore. This is a strong indication, that this feature arises numerically due to poor resolution in this discretization and not physically. At the highest resolution the total ejecta and the fast ejecta distribution are having the same features, which suggest that there is no specific azimuthal direction where is relatively more fast material is ejected.

Next we look at the velocity distribution over different resolutions. Figure (4.14) shows for the different simulations the velocity distribution of the ejecta at the end of the run, at the time stated in table (4.1). The crossed bars showing the amount of ejecta which reached nonphysical regime within each velocity bin. For all resolutions we see that the SD simulations are reaching higher velocities than the AD simulations. This comes from the overestimation of the kinetic energy in the evolution. Also in both cases higher velocities are reached with increasing resolution. The shift of the highest reached velocities seem in both cases very similar from 0.5-0.6 c to 0.75-0.85 c and the difference in highest reached velocity does not decrease with increasing resolution. The distribution gets the shape of a power law in the high resolution simulations. This could be an indication that in even higher particle numbers where convergence is reached the distribution will be a decay from a low velocity peak like a power law up to close to the speed of light. A characteristic of the AD simulations are, that reaching nonphysical regimes seems to correlate with the particle velocity. The higher the velocity the higher the chance to reach nonphysical regimes. This is to be expected, since the fastest material is further away from the other mass elements. Also in this cases the kinetic energy is large and the material is expand rapidly. This leads to very small internal energies, which need during the cooling high precision to recover correctly. For both discretizations the high share of nonphysical particles at high velocities is not an issue. In these instances the kinetic energy should be the dominant driver for the evolution and internal energy be quite small. The failed recovery assigns the lowest temperature and pressure to the particles, which is in this cases be close to the actual value. In the SD case this correlation between velocity and relative amount of nonphysical particles is not prevalent. While there is always a lot of material physically consistent at the peak around 0.1 c the rest of the distribution of the nonphysical particles follow a similar shape like the total velocity distribution. Also as mentioned before in the AD case the amount of thermodynamically inconsistent material decreases with higher resolution. This can be clearly seen in the highest resolution where the relative amount of nonphysical particles is roughly one order of magnitude lower for velocities below 0.3 c.

These comparisons show that the asymmetric discretization improve thermodynamical consistency and lead to more consistent results by higher resolution, which is a desirable behavior of simulations. In the next chapter we will investigate the long term evolution of ejecta and try out different approaches to it.

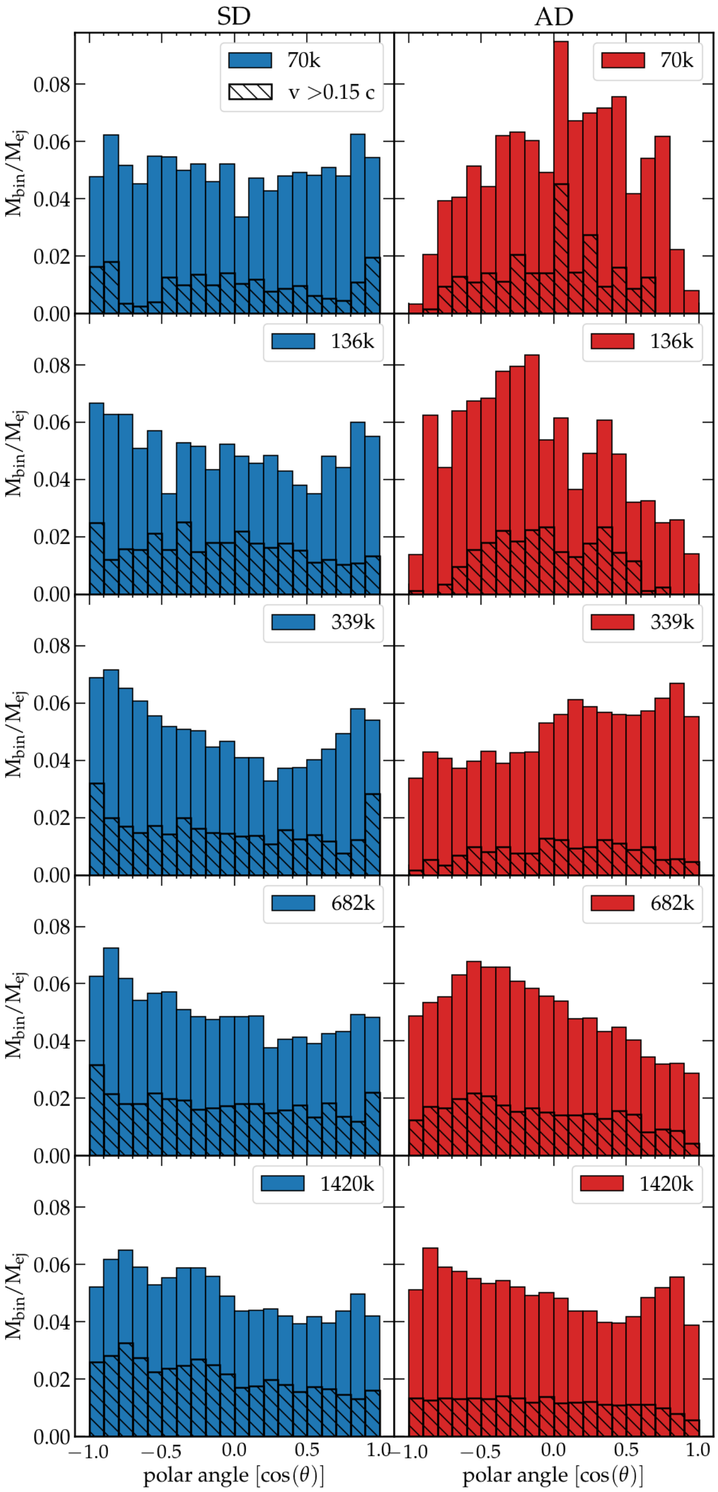

Figure 4.13.: Comparison of the mass distribution over polar angles for simulations with different particle numbers for both discretizations. These are the distributions at the times which can be find in table (4.1). Crossed bars shows amount of matter velocities v>0.15 c.

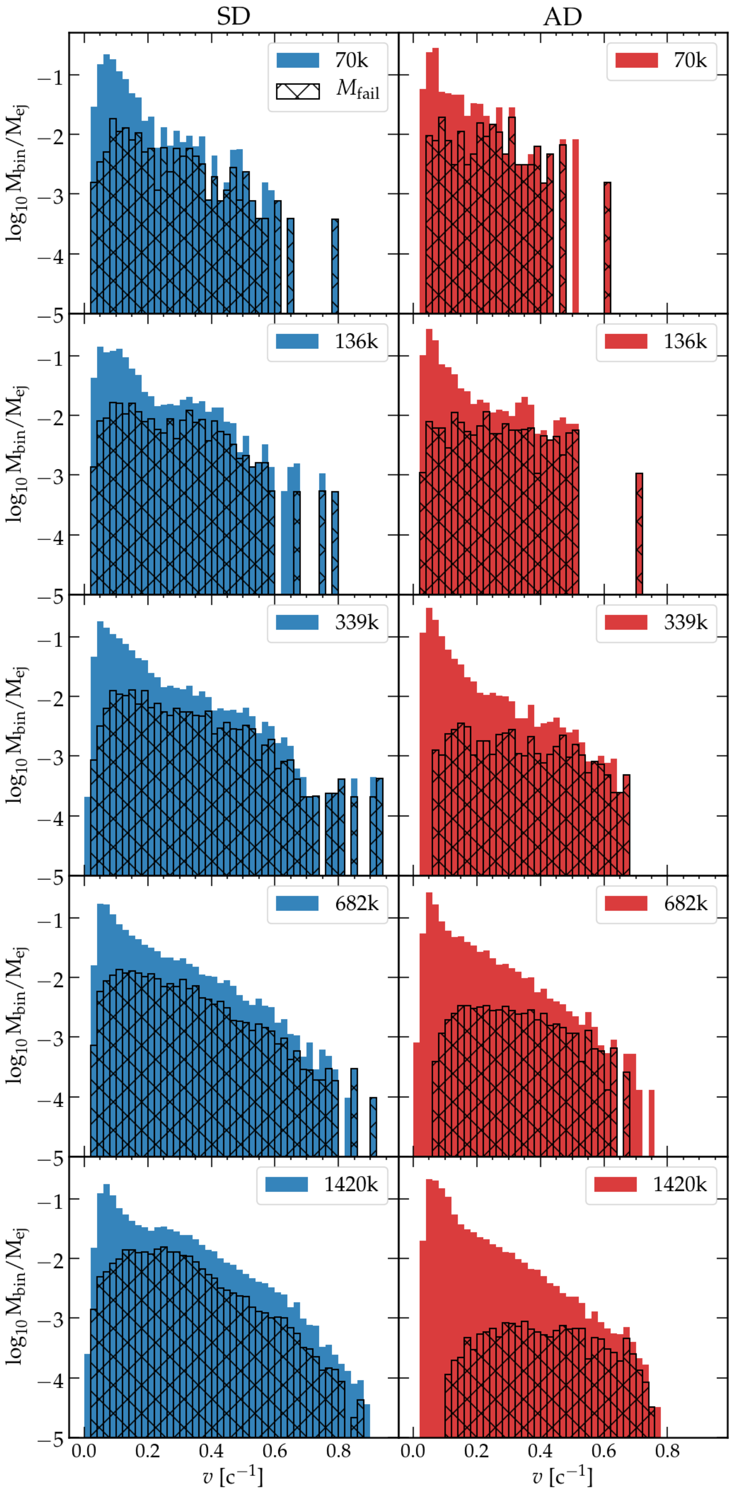

Figure 4.14.: ejecta velocity distribution of simulations with different total particle numbers. Crossed bars are showing amount of matter in each velocity bin for which the recovery scheme fails.

5. Long-term evolution simulations

In the last section we could show that the asymmetric discretization of the energy equation is favorable for a physical consistent evolution of the dynamical ejecta especially within low resolution. For typically chosen total particle numbers this can affect kilonova light curve calculations. Another important point, if BNSM simulation results are used as initial data for radiative transfer calculations, is that the ejecta reached homologous expansion. In this chapter we will show results of a long-term BNSM simulation and discuss homologous expansion on the basis of the results.

5.1. Homologous expansion

Over time the ejecta of BNSM expand and move away from the compact remnant. Therefore pressure and gravitational forces are decreasing. Consider for a ejected fluid element the Newtonian equation of motion in Lagrangian formulation

$$\rho \frac{d\mathbf{v}}{dt} = -\nabla P - \rho \nabla \phi, \tag{5.1}$$

with P, ρ, $\mathbf{v}$, ϕ denoting pressure, density, velocity and gravitational potential. One can see that in the limit of vanishing pressure gradient and gravitational potential the relative velocity change of fluid elements moving with the expansion also approaches zero. At this point homologous expansion is reached. The fluid velocity is constant for each fluid element and the radial profile of velocity becomes proportional to the distance r to the remnant

$$\mathbf{v}(t) \propto r. \tag{5.2}$$

The morphology of the ejecta remains invariant while its rest-mass density is decreasing

$$\rho\left(r,t\right) = \rho_0 \left(\frac{r}{t}\right) \left(\frac{t_0}{t}\right)^3, \tag{5.3}$$

where t_0 defines the $t = 0$ point of homologous expansion and ρ_0 the corresponding rest-mass density at that time. This characteristic is very useful for kilonova modeling since it decouples the hydrodynamic evolution of the ejecta from the radiative transfer. Therefore most studies which calculate kilonova light curves use as a fundamental assumption homologous expansion of the ejecta from the start.

Recent studies, which used SPH simulations as initial data for kilonova modeling, typically took the ejecta at ∼10 - 20 ms after merger and either propagated first the SPH particles with constant velocities for 0.5 s and assumed from there homologous expansion [204, 205] or mapped it into an axial-symmetric simulation to evolve over a longer time [176]. One goal for long-term simulations of BNSM would be to reach the phase where constant velocity approximations or mapping into a different numerical hydrodynamical simulation is not anymore necessary for kilonova calculations.

To determine whether the ejecta have reached homologous expansion Rosswog et al. [182] proposed the homology parameter

$$\chi = \frac{\bar{a} \cdot t}{\bar{v}}, \tag{5.4}$$

with $\bar{a}$ and $\bar{v}$ the average acceleration and velocity. For $\chi = 1$ the material has a constant acceleration and for $\chi = 0$ it has a constant velocity and has reached homologous expansion. In the SPH framework we have the advantage to evaluate integral quantities as χ always on the same amount of matter, which can be difficult in grid based codes. For our numerical set up we define χ for individual SPH particles and have then later the free choice over which matter we take the average. We define χ in our numerical framework for a single SPH particle a as follows

$$\chi_a = \frac{\left|\frac{d\hat{u}_a}{dt}\right| \cdot t}{|\hat{u}_a|}. \tag{5.5}$$

The change in conserved specific momentum will reach zero $\frac{d\hat{u}}{dt} \longrightarrow 0$ when a particle reaches homologous expansion. The specific momentum will reach $\hat{u}_i = (1 + \frac{P}{\rho} + \epsilon)\left(v^i + \beta^i\right)\psi^4 u^0 \longrightarrow W \cdot v^i$ in the limit $P \to 0, \epsilon \to 0, \beta \to 0, \alpha \to 1, \psi \to 1$. With this definition it is possible, to check when individual trajectories reach homologous expansion but also averaging over a specific or the total amount of ejecta to draw conclusion over the ejected material as a whole. Following 5.4, we define the averaged parameter as

$$\chi_{\text{hom}} = \frac{\langle\left|\frac{d\hat{u}}{dt}\right|\rangle \cdot t}{\langle|\hat{u}|\rangle}, \tag{5.6}$$

where $\langle|\hat{u}|\rangle$ and $\langle\left|\frac{d\hat{u}}{dt}\right|\rangle$ are the mass weighted average of the specific momentum and its time derivative. Alternatively, one could also average $\langle\chi_a\rangle$. A comparison showed us that both averaging results in very similar values for χ_{hom}.

In previous studies, χ was used to make qualitative statements of the total ejecta evolving towards homologous expansion [182, 207]. Rosswog et. al showed χ over time for a long-term simulation where the ejecta was cut out 20 ms after merger and evolved for 100 years. They showed that with considering radioactive heating in the ejecta χ falls below 0.01 after 2000 s for a symmetric mass merger. While that shows that the average acceleration at that time is only one per cent of the average velocity, it does not necessarily mean that the velocity will not change more than one per cent for the rest of the time. In the following will try to get a better understanding on what a certain value of χ can say about the change in velocity.

To study the long-term evolution we continue the full simulation from previous section with asymmetric discretization and extended EoS to run up to ~ 250 ms after merger.

5.1.1. Quantifying Homology

At early times various ejecta criteria can differ in the amount of ejecta they are defining. Over time this should eventually converge to the same amount. Using our setup, we can determine whether, throughout the simulated post-merger phase, the variation in the defined amount of ejecta influences the prediction of its proximity to becoming homologous.

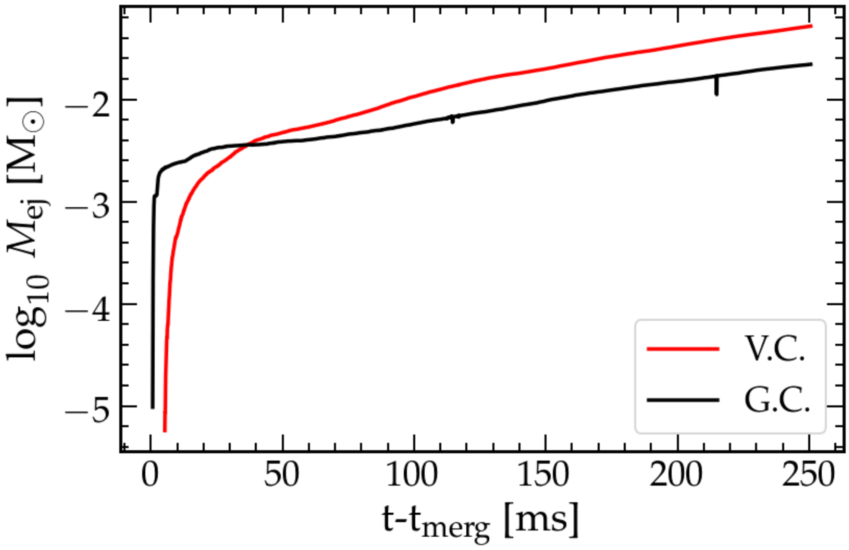

Figure 5.1.: ejected mass of long term simulation over time. Red line is for the virial criteria and a radial cut at 1000 km, which we used in the last section. Black line is the ejecta criteria which is used in [207].

Neuweiler et. al. investigated when the condition of homologous expansion is satisfied for dynamical ejecta with the grid based code BAM [207]. In that work the unbound matter was defined by $u_0 < -1$ and $v_r > 0$, which is a combination of the geodesic criterion (see Sec. 2.3.3) and positive radial velocity (G.C.). They cut out the ejecta at 20 to 30 ms after merger and evolved it further for around 100 ms. On this timescale a decrease of the homology parameter was not apparent. They argue, that this is because the homologous parameter is dominated by the dense material with low velocities. One challenge which might also lead to this result is the difficulty to trace mass flow and define acceleration of it in grid based codes.

We will use for this section the same ejecta criterion and compare it with the virial criterion with a radial cut at 1000 km (V.C.) which we used in the chapter before (also discussed in Appendix (B)). Figure (5.1) shows the amount of ejecta for both criteria. V.C. defines generally more ejecta, since it considers also thermal and nuclear binding energy which can impact the acceleration of fluid elements. The additional radial cut we impose is to avoid defining hot disk material as unbound. In this comparison it has the effect that G.C. has more ejecta in early times, since it does not use a radial cut. Over time, while the dynamical ejecta and the disc are expanding beyond the chosen radial cut, V.C. starts to define more unbound material at around 40 ms after merger. At the same time the amount of unbound matter defined by G.C stagnates for around 10 ms before rising again. This stagnation is consistent with results from different BNSM simulation studies which run until a few tens of milliseconds after merger, and used the geodesic criterion to determine the amount of dynamical ejecta [208–211]. It is conventionally often used to distinguish between early dynamical ejecta and later phases. We see with both criteria the amount of ejecta keeps rising until the end of the simulation at 250 ms with a comparable rate at later times.

We want to point out, since the simulation does not have any treatment of neutrinos or proper treatment of viscosity there are no neutrino driven wind or viscous disc outflows ejecta components, but only dynamical ejecta. We note that no effective cooling mechanism is present without neutrinos, which leads to stronger thermal expansion and an overestimated outflow rate.

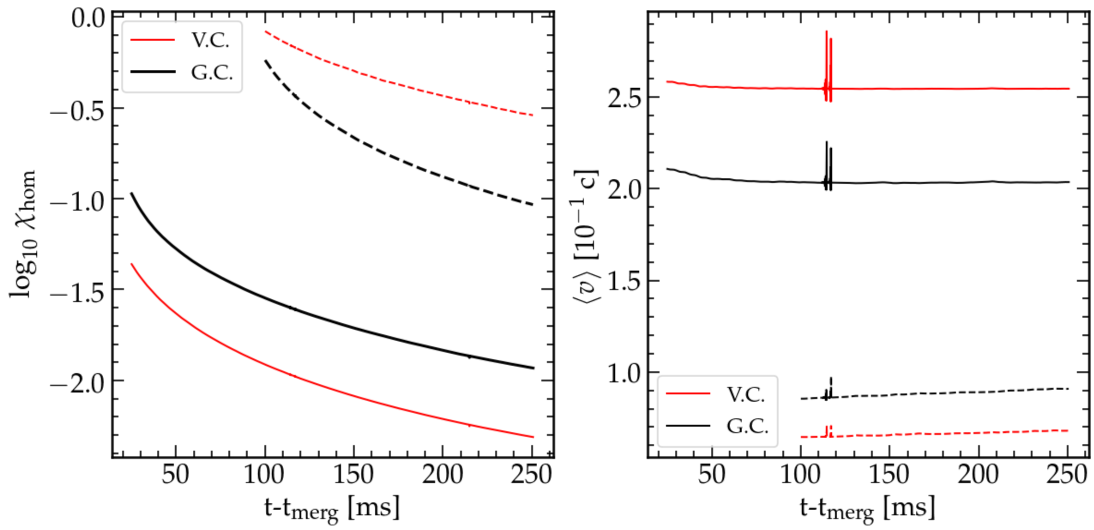

Figure 5.2.: left: homology parameter $\chi_{\rm hom}$ over time. right: average velocity over time. Solid lines is material ejected before 25 ms, dashed lines material which is ejected between 25 ms to 100 ms. For the Black lines the virial criterion is used to define ejecta and for the red lines the geodesic criterion.

To investigate when the ejected material satisfies the condition of homologous expansion we will first consider just the ejecta which became unbound before 25 ms after merger (early) and second material which was ejected between 25 ms and 100 ms after merger (late), and look how the averaged χ_{hom} of this material evolves to later times. Figure (5.2) shows in the left panel the evolution of χ_{hom} for a constant amount of material defined by the virial (red lines) or geodesic criterion (black lines) ejected either early (full lines) or late (dashed line) and at the right panel the corresponding average velocities for this material over time. For the early ejecta χ_{hom} starts at values below 0.1 and is decreasing to 0.005 at 250 ms, while the average velocity stays constant, which shows that for the early dynamical ejecta the deviation from homologous expansion are already negligible at 250 ms. As we saw in figure 5.1, G.C. considers more early ejecta with a lower average velocity compared to V.C., which results in general higher values for χ_{hom} while the decrease in χ_{hom} over time is the same for both ejecta criteria. This parallel shift stems mainly from using a radial cut, which leaves out slow material. To reach 1000 km within the first 25 ms the ejecta needs at least a velocity of $0.13c$. In the case of the late dynamical ejecta, the radial cut excludes only material moving slower than $0.03c$, which has a minimal impact. For the late ejecta, both criteria begin with χ_{hom} values near one and decrease more slowly than in early ejecta, also possessing significantly lower average velocities, suggesting that this material reaches a homologous state over a much longer timescale. Since the virial criterion takes thermal energy into account it considers slow but hot material. We see now a reversed relation, that V.C. considers more material with lower average velocity as unbound and has therefore higher values of χ than G.C.

One also can see for the later ejecta, that the average velocity is slightly increasing over time. This shows that for this material a significant part of energy resides as thermal energy and over time converts to kinetic energy through pressure-volume work. For the early ejecta with higher kinetic energies is this effect insignificant.

The averaged homologous parameter indicates that, over time, the material progresses to freely expanding, but does not quantify how much material deviates and how strong this velocity deviation can be. It is not clear what a value of, for example, $\chi_{\text{hom}} = 0.01$ says. This could be helpful for radiative transfer models for error estimation when using ejecta from BNSM simulations. Next, we want to try to make more quantitative statements about the ejecta using the homology parameter.

For that we look at the correlation between the value of χ and the change in velocity. We look at the early ejecta and define for specific velocity intervals of the early ejecta the average χ_{hom} value at 25 ms as $\chi_{\text{hom},0}$. The early ejecta has velocities between 0.1 c and 0.64 c. We divide it in intervals of the size of $\Delta v = 0.02$. We look how χ_{hom} and v changes over time for each velocity interval. Figure (5.3) shows in the left panel the normalized decrease $\chi_{\text{hom}}/\chi_{\text{hom},0}$ for each velocity interval. For ejecta faster than 0.16 c χ_{hom} decay roughly at the same rate. For slower ejecta, one can see that the decay rate is slower. The right panel shows the change in velocity for each velocity interval relative to the velocity v_0 at 25 ms. For the most velocities the change is less than 3 %, while for the material slower than 0.16 c changes between 6 and 15 %. Most of the ejecta gets slower over time, but for a few velocity intervals the velocity increased slightly. The average χ_{hom} at 25 ms after merger is 0.07. While on average it might be not a bad estimate to assume a change of 7 % in velocity, we see through this that especially the slower material can have a change up to 15 % in velocity. 10 % of the early ejecta has a velocity between 0.1 and 0.12 c.

For kilonova light curve, using estimation of the photospheric radius, the ejecta faster than 0.2 c is relevant for the roughly the first 4 days [212]. Material with velocities between 0.1 c and 0.2 c are relevant for 4 to 6 days after merger.

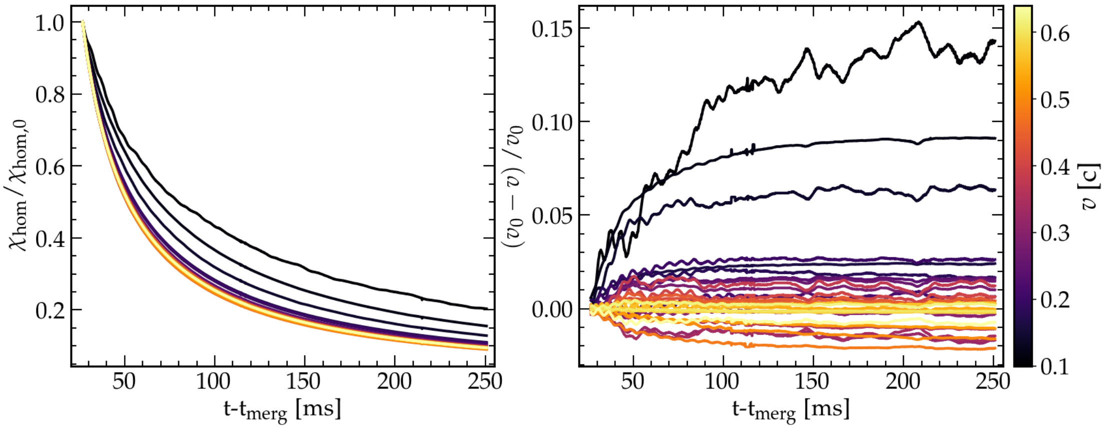

Figure 5.3.: Left: decrease of the homology parameter $\chi_{\rm hom}$ over time for different ejecta velocity intervals normalized to $\chi_{\rm hom,0}$ at 25 ms after merger. Right: Change in velocity over time for different ejecta velocity intervals relative to the velocity v_0 at 25 ms after merger.

5.1.2. radial velocity

Since we defined χ on a particle level we can check not only an average of a given time or velocity, but also the full distribution at a given time. This for once makes it possible to test if the homologous parameter can be used to predict an upper limit when fluid elements deviation from homology falls below a certain threshold. Figure (5.4) shows in the left panel the χ value distribution of the ejected particles at $t_0 = 25$ ms after merger over the absolute value of change in radial velocity

$$\Delta v_r = \frac{v_r(t_0) - v_r(t_1)}{v_r(t_0)} \tag{5.7}$$

until $t_1 = 250$ ms after merger. The right panel shows the change in radial velocity over the radial velocity at t_0. The black points are particles for which the radial velocity increased, red points for which the radial velocity decreased. While for each value of χ exist a broad range of Δv_r, one can see a clear linear trend. The change rate depends also on the velocity itself, as seen in the right panel, which shows a anti-proportional relation between Δv_r and v_r and was also indicated by figure (5.3). Slower mass elements have a larger relative change in velocity, since for the same pressure work will their ratio between thermal and kinetic energy change more as for a mass elements, which has already most of its total energy as kinetic energy. For the correlation between χ and Δv_r one can think of $\Delta v_r / \Delta t$ as an approximation of the acceleration a which is proportional to χ and t/v as the constant of proportionality.

The spread of these roughly linear correlation stems from the variation in temperature and pressure for different mass elements in different regions. While in some regions a slower moving particle has more material around it and feels more pressure, a particle moving in less dense regions with the same velocity might encounter less pressure, which lead to smaller changes in velocity.

We observe a broadening linear trend between χ and Δv_r. This can be used at early times to estimate an upper limit of how much the velocity could change. The gray dashed line indicate this upper limit, which gives a power law relation $\Delta v_r = k \cdot \chi^l_{\text{hom}}$ between homology parameter and the variation in velocity. This makes it possible to give the homology parameter a quantifiable value of how close matter is to reach homologous expansion. We get as relation between change in velocity over time Δv_r and the homology parameter χ

$$|\Delta v_r| = 1.01 \chi^{0.74}_{\text{hom}}. \tag{5.8}$$

The value $l = 0.74$ describes the slope of the gray line. We find only a few outlier from this trend exist for decreasing velocity but 98 % of particles are below this limit.

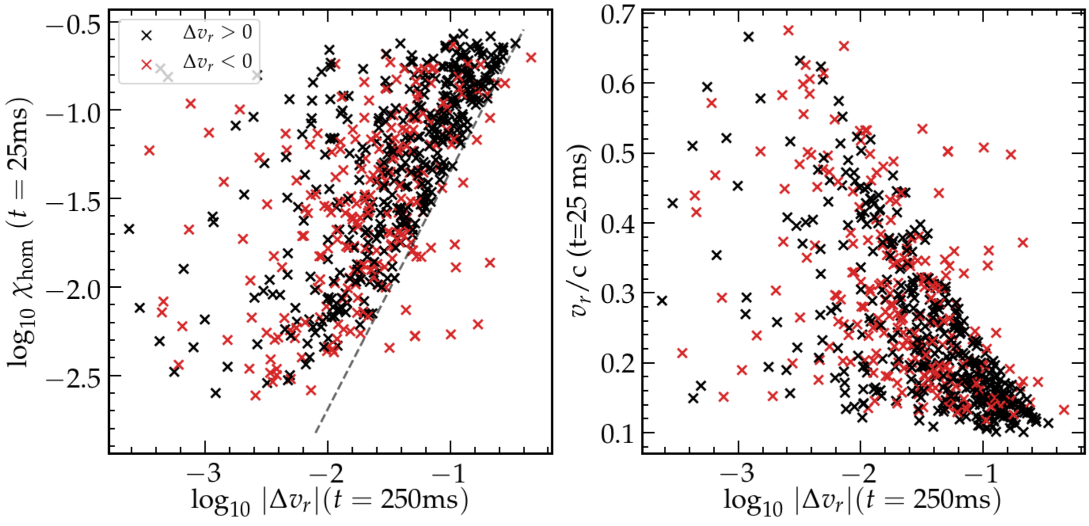

Figure 5.4.: homology parameter at 25 ms after merger. left: over the absolute value of change in radial velocity after 225 ms for ejected SPH particles at 25 ms. Black crosses are particles which $\Delta v_r > 0$,and red $\Delta v_r < 0$ right: change in radial velocity over the particles velocity at t= 25 ms after merger.

Using the relation eq. (5.8) we can quantify the amount of matter which falls below a certain threshold deviation in velocity over time. By using different thresholds of χ_{hom} it is possible to show how close different relative amount of mass are at reaching homologous expansion.

Figure (5.5) shows the relative amount from early ejecta and late ejecta, which reached below a certain value of χ_{hom}. As for (5.1) early ejecta is material which became unbound before 25 ms after, and late ejecta became unbound between 25 ms and 100 ms. Three different thresholds for χ_{hom} were chosen. The solid line shows the relative amount of ejecta which reached $\chi_{\mathrm{hom}} < 0.01$, which correspond to an upper limit of Δv of about 3%. The dashed line shows the amount ejecta with $\chi_{\mathrm{hom}} < 0.04$ which corresponds to a Δv of 10% and the dashed-dotted line shows $\chi_{\mathrm{hom}} < 0.1$ which corresponds to a Δv of 20%.

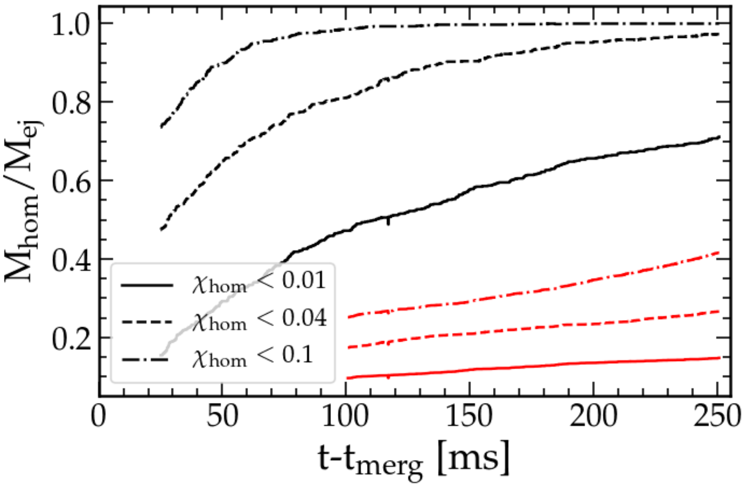

Figure 5.5.: Upper limit of expected change in velocity for three different thresholds. $\chi_{\mathrm{hom}} < 0.01$ (solid line) correspond to a maximal change in radial velocity of about 3%, $\chi_{\mathrm{hom}} < 0.04$ (dashed line) corresponds to 10% and $\chi_{\mathrm{hom}} < 0.1$ (dashed-dotted line) corresponds to 20%. The plot shows amount of early ejecta (black lines, ejected before 25 ms) and late ejecta (red lines, ejected between 25 ms and 100 ms) which are below the thresholds over time.

From this we can estimate that 97% of early ejecta will change their radial velocity not more than 10% , and 71% of it not more than 3% from 250 ms after merger onward. For the late ejecta will change 41% their radial velocity not more than 20% , 26% of it not more than 10%, and 14% of it not more than 3% from 250 ms after merger onward. This is consistent with figure (5.2) where we saw that later ejected material is more turbulent then the early ejecta of the first 25 ms. Over the 150 ms the amount of late ejecta falling under a certain threshold is comparatively slow, indicating that it will need several seconds until the velocity remains constant, in which the velocity distribution of the ejecta still can change. In the next section we look at the velocity distribution of the ejecta at 250 ms of the long-term simulation and make comparisons with two approaches reaching late times to use early ejecta for radiative transfer models assuming homologous expansion, without evolving the whole system for a long time.

5.2. Velocity distribution

In earlier kilonova studies ejecta was taken at 25 ms from SPH simulations and extrapolated with constant velocity to later times to map the velocity distribution into a radiative transfer model and assume homologous expansion. Another common approach to reach later times is to cut out ejecta at early times and restart a simulation only with the ejected material, which saves a lot of computational cost. One problem with that approach is that the material will loose pressure support from the cut out bound matter. We can compare the velocity distribution of our long-term simulation with distributions using these approximations.

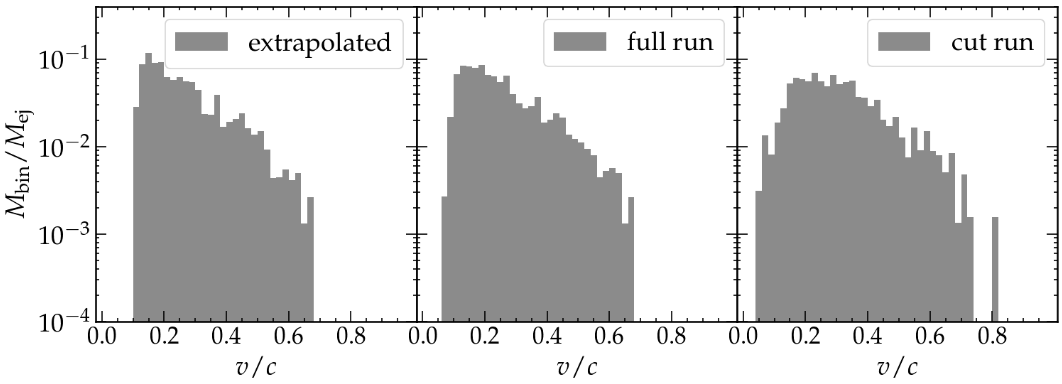

Figure 5.6.: velocity distribution at 250 ms of material M_{ej} which is ejected at 25 ms for three different approaches to reach that late times. left: ballistic extrapolation from 25 ms to 250 ms. middle: complete run until 250 ms. right: cut out of remnant at 25 ms and only simulate ejecta until 250 ms.

Figure (5.6) shows the velocity distribution at 250 ms of material which was ejected at 25 ms (virial criterion and r > 1000 km) for the three different approaches reaching this time. The left panel shows the distribution using the extrapolated approximation. This distribution coincides with the velocity distribution at 25 ms. In the middle panel is the velocity distribution of the full run of the whole system. The peak velocity at 0.15 c do not change over time. A part of the material decreased slightly its velocity since now 0.06 c is the slowest ejected material in the full run other than 0.1 c in the extrapolated approach. The slope is less noisy in the full run. Overall, the extrapolated method yields a similar velocity distribution and serves as a reasonable approximation. In the simulation where only the ejecta was evolved, the setup was as follows: We removed all particles which were inside a radius of 100 km around the center of mass of the system or were still bound by the definition of the virial criterion.

We kept the metric from 25 ms after merger fixed and also turned off the back reactions which are used to account for the loss of energy and angular momentum carried away by gravitational waves. We modified also the neighbor search routine, which originally uses a fixed-sized grid and assigns all particles outside that grid in a single cell (see sec. (2.3)).

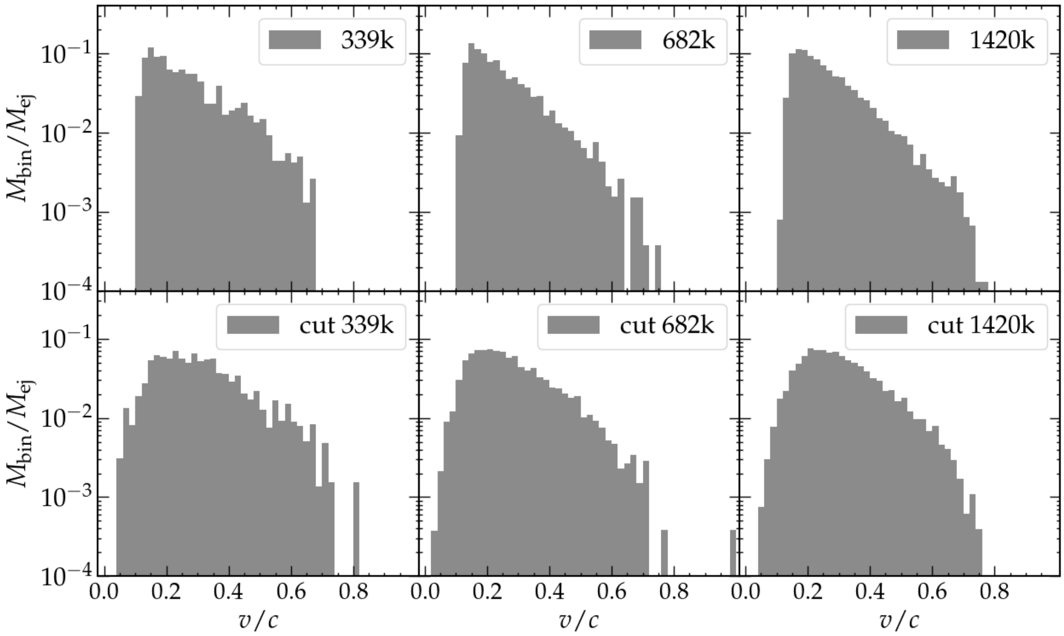

Figure 5.7.: Comparison between the velocity distribution from material ejected at 25 ms and extrapolated with constant velocity (upper row) or cut out ejecta simulation (lower row) to 250 ms after merger for three different resolutions.

Now the grid size is dynamic such that all particles are within the grid. With that approach we restarted at 25 ms with 3259 particles. The right panel of figure (5.6) shows the velocity distribution of the same SPH particles as in the other two panels. Due to the truncation of bound matter at 25 ms after merger, the absence of pressure support leads to a reduction in velocity for some material. We chose for the cut a radius of 100 km to limit the amount of lost pressure support for the ejecta above 1000 km. None of the ejecta above 1000 km fall back. But we see a wider spread in velocity which is also noisier than in the full run. Because for some particles a sudden change of neighbor particles, or change in number of neighbors can lead to numerical effects on their trajectory which can slow down or accelerate specific particles. With all this impairments the distribution is still similar to the distribution of the unaltered run. The peak at 0.15 spreads wider up to 0.35 c and a few particles reached velocities over 0.7 c. One challenge faced by the truncated long-term simulation is its very low resolution. Therefore, we check for the higher resolution runs we did in section (4.3) how the velocity distribution looks like for long-term cut runs. Figure (5.7) shows for 339×10^3, 682×10^3 and 1420×10^3 a comparison between the velocity distribution for evolving the ejecta ballistically to 250 ms (upper row) and and cutting it out and running the simulation until 250 ms (lower row). While one can see the effect of higher resolution on the velocity distribution towards a power law from minimum velocity as peak to maximum velocity, the main issue with the cut out simulations do not improve with higher velocity.

The distributions are becoming less noisy, but the missing pressure is having a clearly visible impact, causing the velocity distribution to blur. For the evolution of the early ejecta,it is a better approximation to use the ballistic approach, since one can avoid the smearing. In all this approaches the biggest flaw is the missing later ejecta, since as we saw in figure (5.1) the mass ejection does not converge at these early times but continues over a greater time scale. Using only early time ejecta for kilonova models always excludes matter which will be relevant for a complete light curve. Because of this, the goal for long-term simulations should be to track all matter over the whole time of the simulation, preferably until it reaches homologous expansion with a sufficient resolution to ensure physical trajectories with minimal impact from numerical effects.

In this chapter we achieved to simulate the complete BNSM system for 250 ms, which is an order of magnitude longer then our previous simulations. Over this time 5.2×10^{-2} $\mathrm{M}_{\odot}$ is ejected, using the virial criterion for defining unbound material. We could estimate how close material is in reaching homologous expansion. For the outflows of the first 25 ms ($2.2 \times 10^{-3}\mathrm{M}_{\odot}$) will 97% of this material the velocity not change more than 10% onward. For later ejecta which is slower and hotter will it take on the order of seconds to reach homologous expansion. We could show that using a long-term simulation of the full system results in changes of the velocity distribution even of the early ejecta compared to ballistic approximations or simulations of the cut out ejecta. Especially for the later is the missing pressure support prevalent, even for higher resolutions.

While in principle it would be possible to run this simulation even longer, with increasing time decreases the spatial resolution of the outer ejecta. Therefore is it necessary to increase also the resolution of the ejecta for long-term simulations. Fulfilling both, high resolution and long-term evolution is a highly computational expensive task. The next section discusses a method to increase ejecta resolution with minimal computational cost.

6. Particle Splitting

In this chapter we will focus on the resolution of the dynamical ejecta and how to improve it. We will use the implemented extended EoS and the asymmetric discretization for the energy equation described in the last chapters for the simulations here.

In the previous chapters we usually used simulations which where initialized with around 300000 particles. Typically between 1500 to 3000 particles are getting ejected at this chosen resolution. 99 % of the particles stay in the remnant and disc. Increasing the total amount of particles is a quite inefficient way to increase the resolution of the ejecta, since the ratio of bound material to ejected stays roughly the same, while the computational time increases with the total number of particles. A better way to achieve higher resolution is by trying to lower the ratio between ejected and bound particles by particle splitting. Kitsionas and Whitworth were the first who used this method for resolution improvements [213]. Our employed splitting scheme follows the same structure. Particles which fulfill a certain criteria are split into N_{split} daughter particles. The mass of the parent particle is evenly distributed

$$M_{\text{daughter}} = \frac{M_{\text{parent}}}{N_{\text{split}}} \tag{6.1}$$

between the daughter particles. The hydrodynamical quantities of the parent particle are inherited by the daughter particles. We run simulations for $N_{\text{split}} = 4 + 1$, where "$+1$" refers to a daughter particle at the original position of the parent particle. This is an approach similar to Vacondio et al. [214], which found in a systematic study that a daughter particle at the position of the parent particle reducing differences in density due to splitting. Fig. 6.1 illustrates how the daughter particles are distributed. A cube frame is used to position on four opposing vertices a daughter particle. We follow the idea of [213] and trying similarly to evenly divide the volume between the daughter particles with setting the position offset d $= 0.8 \cdot h_s \cdot 4^{-\frac{1}{3}}$ and choose the smoothing length of the daughter particles as $\delta h_s =$ d. The table 6.1 lists the positions of the daughter particles.

The orientation with respect to the coordinate system of the daughter particles are always the same and is independent of the position, velocity and neighborhood of the parent particle. We note that the employed splitting scheme is a easy to implement and simplistic choice for the first tests, since we want to focus more on the choice of the criterion for on-the-fly splitting to efficiently improve the resolution of the ejecta for minimized additional computational cost. To achieve this, the scheme should be sufficient, while we are aware that by choosing the position and orientation of the daughter particles depending on the direction the parent is moving and the position of the neighboring particles will reduce numerical noise.

6.1. Splitting criteria

The splitting criterion should only trigger where higher resolution is in need and mainly for the ejected material. Different possible criteria can achieve this. Low resolution is linked with high particle velocity, hence one possibility could be to use particle velocity or radial velocity as a criterion. The smoothing length normalized by the distance to center of mass $\frac{h_s}{r}$ can also be a measure to detect areas with low particle number density. Since we want to focus on the ejecta, a reasonable choice would also be the ejecta criterion eq. 2.57. Ideally we want the particles split before they are in a low resolution environment. Therefore as a first check we tested different thresholds for these four criteria to check when and how many particles would fulfill the criterion. We used the AD simulation from chapter 4.2.2 and tested at different times how many particles would have been split under different criteria. In the following we will refer to it as the fiducial simulation.

	x	y	z	h_s
1	d	d	d	d
2	d	-d	-d	d
3	-d	-d	d	d
4	-d	d	-d	d
5	0	0	0	d

Table 6.1.: positions of the daughter particles relative to position of the parent particle, where $d = 0.8 \cdot h_s \cdot 4^{-\frac{1}{3}}$.

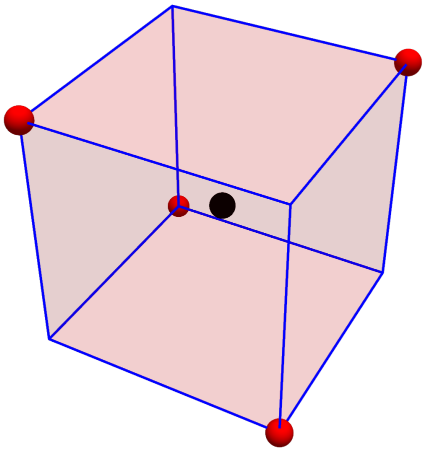

Figure 6.1.: Implemented particle splitting pattern. From one parent particle (black) into four daughter particles (red). Note that we put a additional daughter particle at the position of the parent.

Figure 6.2 shows a comparison between the criteria and how many particles would have been split for thresholds which appeared to be reasonable. Upper row shows the system projected in the x-y-plane, lower row in the x-z-plane. Purple shaded dots indicate particles which fulfill the criterion, while yellow ones do not. The snapshot of the simulation is about 1 ms after merger. On the most left side the criterion $v_{\text{rad}} > 0.15$ is shown. In this early phase this criterion shows promising results by detecting only the fast expanding matter. At later times the slow ejecta material is left out. Next panel shows the criterion $v > 0.24$. The main problem is that, although it identified fewer ejected particles than the radial velocity criterion, it applies to thousands of particles within the differentially rotating remnant. In the third panel is the criterion $\frac{h_s}{r} > 0.22$. In the x-y-plane one can see that region outside the remnant and the spiral arms is completely covered by this criterion. Here interestingly significant more particles in the polar direction would be split indicating the low resolution in this region. While only loosely bound and ejected material are caught by this criterion, not all ejecta over time will get split. The far right panel shows the criterion $\epsilon_{\text{stat}} > 0.97$ (see ejecta criterion eq. 2.57) which satisfies for all ejected and some loosely bound material. The advantage of this criterion is that all ejecta will get split shortly before it becomes unbound. At this early phase it has together with the radial velocity criterion the least amount of particles split. Unlike the radial velocity criterion, the number of split particles will grow over time, primarily enhancing the resolution within the ejecta and at the outer boundary of the torus. From this comparison the ejecta criterion seems to be most promising for getting the whole ejecta split, while the smoothing length criterion really applies splitting where low resolution starts to emerge.

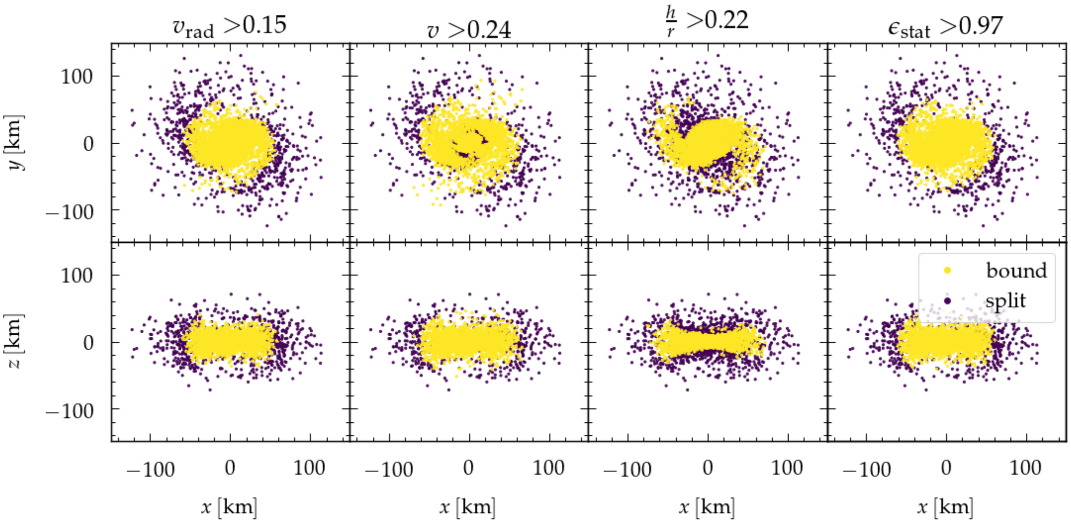

Figure 6.2.: Snapshot 1 ms after merger, showing for four different criteria for when particles should split. Purple shaded dots indicate particles which fulfill the criterion, yellow ones do not. Upper row show x-y-plane, lower row x-z-plane of the system. From left to right are the criteria $v_{\text{rad}} > 0.15$, $v > 0.15$, $\frac{h_s}{r} > 0.22$, $\epsilon_{\text{stat}} > 0.97$.

We opted to examine both of these criteria individually and in conjunction, and see the impact and differences between the runs. For that, we restarted at the time of merger the fiducial run but now with the splitting scheme. With this approach we can compare the original run with the new simulation including splitting to see what impact splitting has on the ejecta. Figure 6.3 shows a comparison of the ejected mass over time between the fiducial run (blue line) and the run including splitting (red line) for the three different criteria. Additionally, the amount of ejected particles that have been split is depicted (black dotted line) and the total amount of mass of particles which were split (black dashed line). Obviously in the cases where the ejecta criterion is also used as splitting criterion the red and black dotted line are on top of each other. For the smoothing length criterion we decreased the threshold from $\frac{h_s}{r} > 0.22$ to $\frac{h_s}{r} > 0.2$ to try to increase the fraction of split ejecta. At the right panel one can see that total ejecta is roughly a factor two higher than the split part of ejecta. Also in comparison to the simulation without splitting it starts with slightly higher ejecta but over time it converges to same amount of ejected matter after 15 ms after merger.

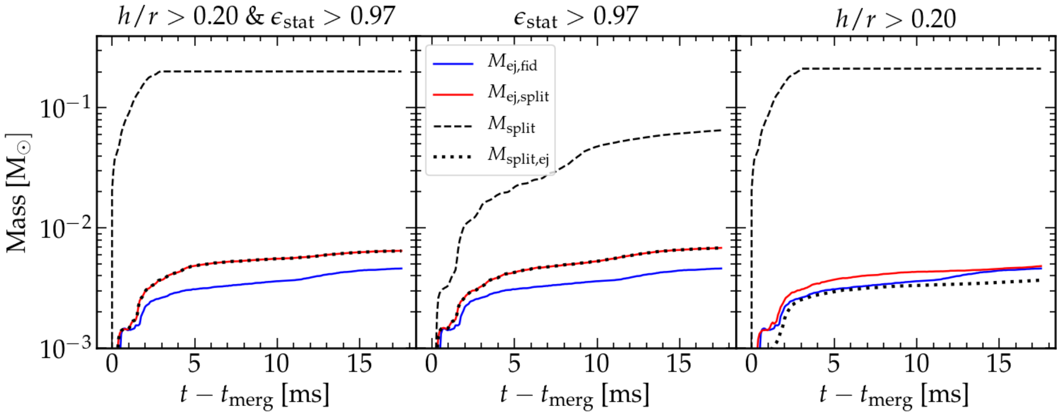

Figure 6.3.: Comparison between three different applied splitting criteria and their impact on ejecta mass over time. Left panel are $\epsilon_{\rm stat} > 0.97$ and $\frac{h_s}{r} > 0.2$ as criterion used, in the middle panel only the first, in the right panel only the latter. Solid blue line shows fiducial simulation without splitting, solid red line simulation with splitting, black dotted line is the amount of ejecta which is split, and dashed line depicts total amount of mass of split particles.

From our resolution study we saw, that with increasing particle number the amount of ejecta increases. We would expect the same trend through the increased resolution using particle splitting. This can be seen in the left and middle panel where in the simulation with splitting the amount of ejecta is increased by a factor two. Interestingly the amount of ejecta was not impacted if additionally to the ejecta criterion also the smoothing length criterion was used, even so that the combined criterion split 0.2 $M_\odot$ particles. Using just the ejecta criterion seems therefore the most efficient way to split and we will continue in the next section with this criterion.

Table 6.2.: comparison of simulations with different starting particle numbers with and without splitting. Table shows the amount of ejecta at end of the simulation outside a radius of 1000 km.

number of particles	simulation	$t - t_{\text{merg}}$ [ms]	M_{ej} $[10^{-3}\text{M}_{\odot}]$	N_{ej}
283×10^3	split	25.23	3.91	6321
136×10^3	split	26.80	1.46	925
70×10^3	split	27.03	2.56	1045
1420×10^3	fiducial	22.87	4.21	7518
682×10^3	fiducial	24.33	3.71	2346
339×10^3	fiducial	25.10	2.21	636
283×10^3	fiducial	25.33	2.24	737
136×10^3	fiducial	25.68	1.70	193
70×10^3	fiducial	26.06	1.61	115

6.2. Impact on resolution

We compare simulations with particle splitting to simulations of our resolution study in chapter 4.3 which we call from here on the fiducial simulations. We run three simulations using splitting with different initial particle number of 70×10^3, 136×10^3 and 283×10^3 up to 25 ms after merger.

Table (6.2) lists the simulations with and without splitting for different starting particles numbers. The total particle number in the simulations with splitting will rise over time. It shows also the ejecta in terms of mass and number of particles outside a radius of 1000 km at the end of each simulation. One can see a clear increase in the number of particles in the ejecta, which is relatively to the ejecta mass comparable with the fiducial runs which started with 5 times more total particles.

Figure 6.4 shows in the left panel the ejecta mass over time. The black lines depict the fiducial setup and the red lines the simulations with splitting. The different line styles correspond to the various initial particle numbers. While in the fiducial simulations a slight rise in ejecta mass is visible as the particle number increases, is this trend not clear in the splitting simulations. The splitting simulation with 136×10^3 particle run has least ejecta compared to the other two. The trend of increasing ejecta with increasing particle number is still within the uncertainty of the stochasticity, which we explored in chapter 3, where we show how sensible is ejecta to smallest changes in the system. The numerical noise, which is introduced through the particle splitting, might also be enough to interfere with this trend.

The right panel shows how much relative ejecta mass M_{fail} correspond to SPH particles for which the EoS interpolation fails, which we described in Section (4.2). We see the same trend as in the fiducial simulations, that with increasing particle number the relative amount of M_{fail} decreases. Additionally if we compare simulations with the same initial particle number, we clearly see a noticeable decrease in M_{fail} in the splitting simulations.

The amount of M_{fail} is more comparable with the fiducial simulation with particle number between 339×10^3 and 1420×10^3 particles. For the ejecta distributions we will compare the splitting simulations with the particle number in this higher range to see if it shows the same convergence trend we saw there.

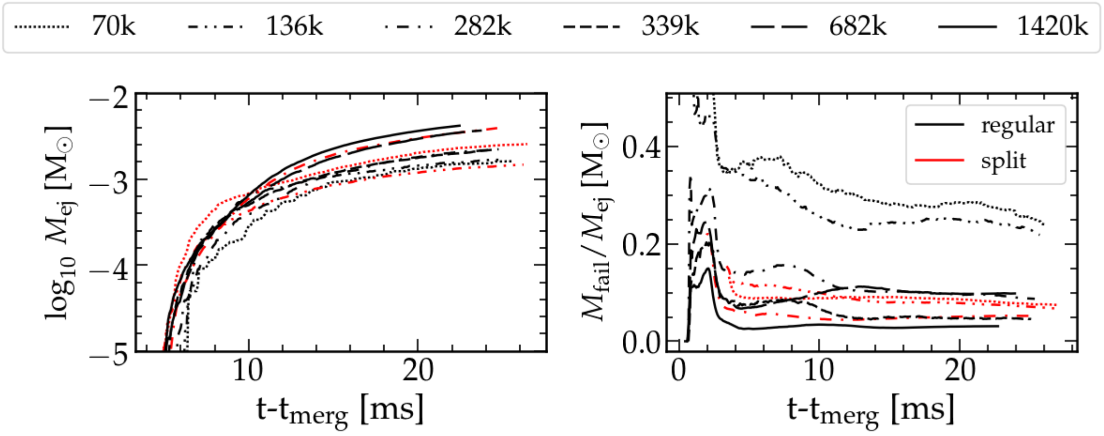

Figure 6.4.: Comparison between fiducial runs and simulations with particle splitting. Different line styles correspond to different initial particle numbers as described in the legend above. Black lines depict fiducial simulations and red lines simulations with splitting. Left: Amount of ejecta over time. Right: relative amount of matter which correspond to SPH particles for which the EoS interpolation failed.

Figure 6.5 shows a comparison between the angular mass distributions of the splitting simulations and the fiducial simulations at 25 ms after merger. The fiducial simulations exhibit a modest north-south asymmetry of approximately 10% in the total mass distribution across all resolutions. In contrast, the fast ejecta (v > 0.15 c) becomes more uniformly distributed with increased resolution. The splitting simulation is for lower resolutions but also show a north-south asymmetry at the highest resolution at around 10%. We can see the fast ejecta also distributes more evenly for higher resolution. At very low resolution the amount of fast ejecta decreases towards the poles and with increasing particle number it starts to even out. For very low initial particle number a mass deficit at the poles occurs which was also visible in the fiducial simulation with below 339×10^3 particles (see figure 4.13). The splitting simulation with 283×10^3 particles reveals a relatively smooth angular distribution, displaying less noise compared to other splitting simulations. This result is comparable to the reference simulation conducted with 1420×10^3 particles.

In figure 6.6 we see a comparison between the velocity distributions of the simulations with splitting and the fiducial simulations at 25 ms after merger. Similar to figure 4.14 the crossed bars show how much mass corresponds to SPH particles for which the EoS interpolation fails. In the fiducial simulations, the velocity distribution exhibits a peak at approximately 0.05–0.1 c, followed by a decline extending up to 0.8 c. With higher resolution, this decline approaches a power-law behavior, evident as a linear trend on the logarithmic scale. The same distribution can be reproduced using particle splitting while starting with only a fifth of the particle number. Comparing the last two panels, the ejecta velocity distribution of the ejecta and the velocity distribution of M_{fail} agree very well with each other between the fiducial simulation and the simulation using splitting.

As described in section 2.2 the error of the smoothing approximation in SPH is proportional to h_s^2 using the spline kernel. Figure 6.7 shows the ejecta smoothing length distribution normalized to the particle distance to the center of mass at 25 ms after merger. For the fiducial simulation with 339×10^3 particles the normalized smoothing length reaches up to 0.7. It decreases to below 0.5 for 682×10^3 particles and it stays below 0.4 for 1420×10^3 particles. For the simulations with splitting the distribution for a initial particle number of 70×10^3 and 136×10^3 particles stays below 0.6 and reduces also below 0.4 for 283×10^3 initial particles. As in velocity and angular distribution we see the same convergence effect as in the fiducial simulation with five times more total amount of particles. Starting with 283×10^3 particles with splitting reduces the average smoothing length in the ejecta by about 40 % and with this the error of the smoothing approximation by 75 % compared with the simulation without splitting.

Already with this simplistic splitting scheme, it is possible to accomplish an efficient measurable improvement of the ejecta resolution, which is comparable to simulations which need up to five times the total amount of particles to achieve the same resolution. While the computational time was comparable or faster to a run with 339×10^3 particles. The angular and velocity distribution affects directly kilonova light curve calculations. A clumpy or noisy distribution or asymmetries can lead to variation in luminosity for different viewing angles. We see a clear trend for higher resolution simulations that velocity and polar angle distribution gets smoother, while a north-south asymmetry remains.

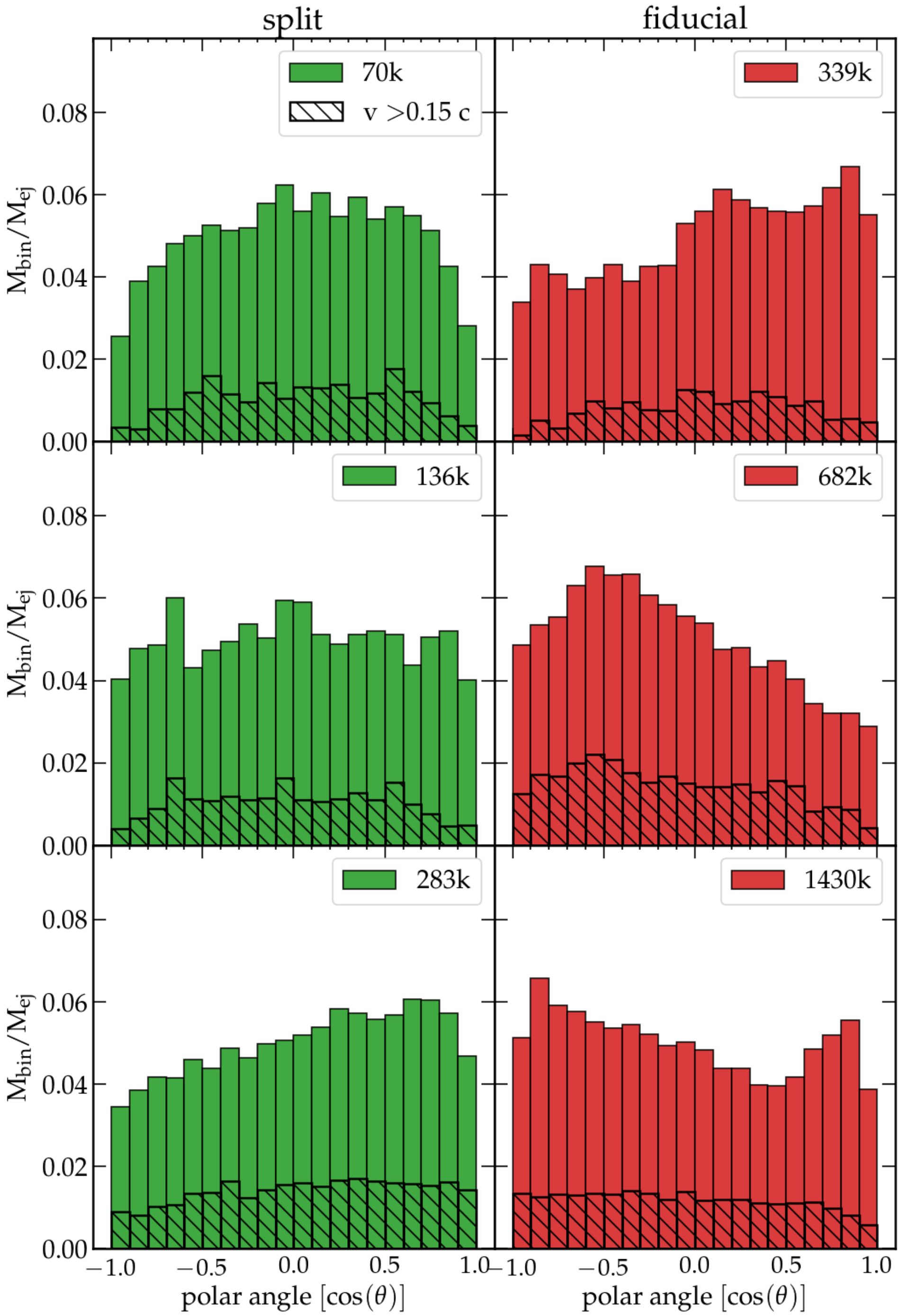

Figure 6.5.: Comparison of the polar angular distribution of ejecta between simulations with splitting (left) and fiducial simulations (right) for different particle numbers at around 25 ms after merger. Crossed bars show relative amount of ejecta faster than 0.15 c.

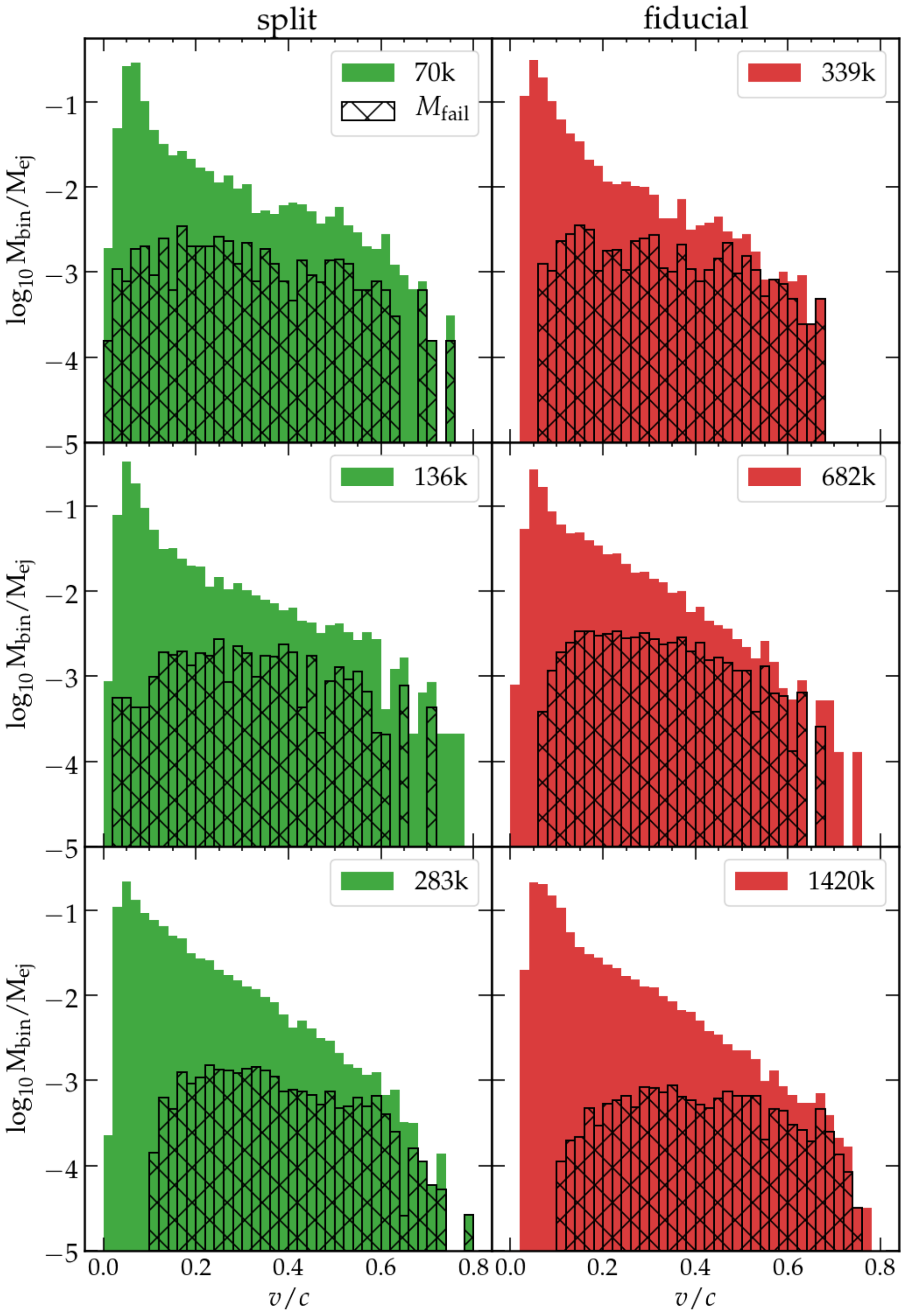

Figure 6.6.: Comparison of the ejecta velocity distribution between simulations with splitting (left) and fiducial simulations (right) for different particle numbers at around 25 ms after merger. Crossed bars show relative amount of ejecta for which the EoS interpolation fails.

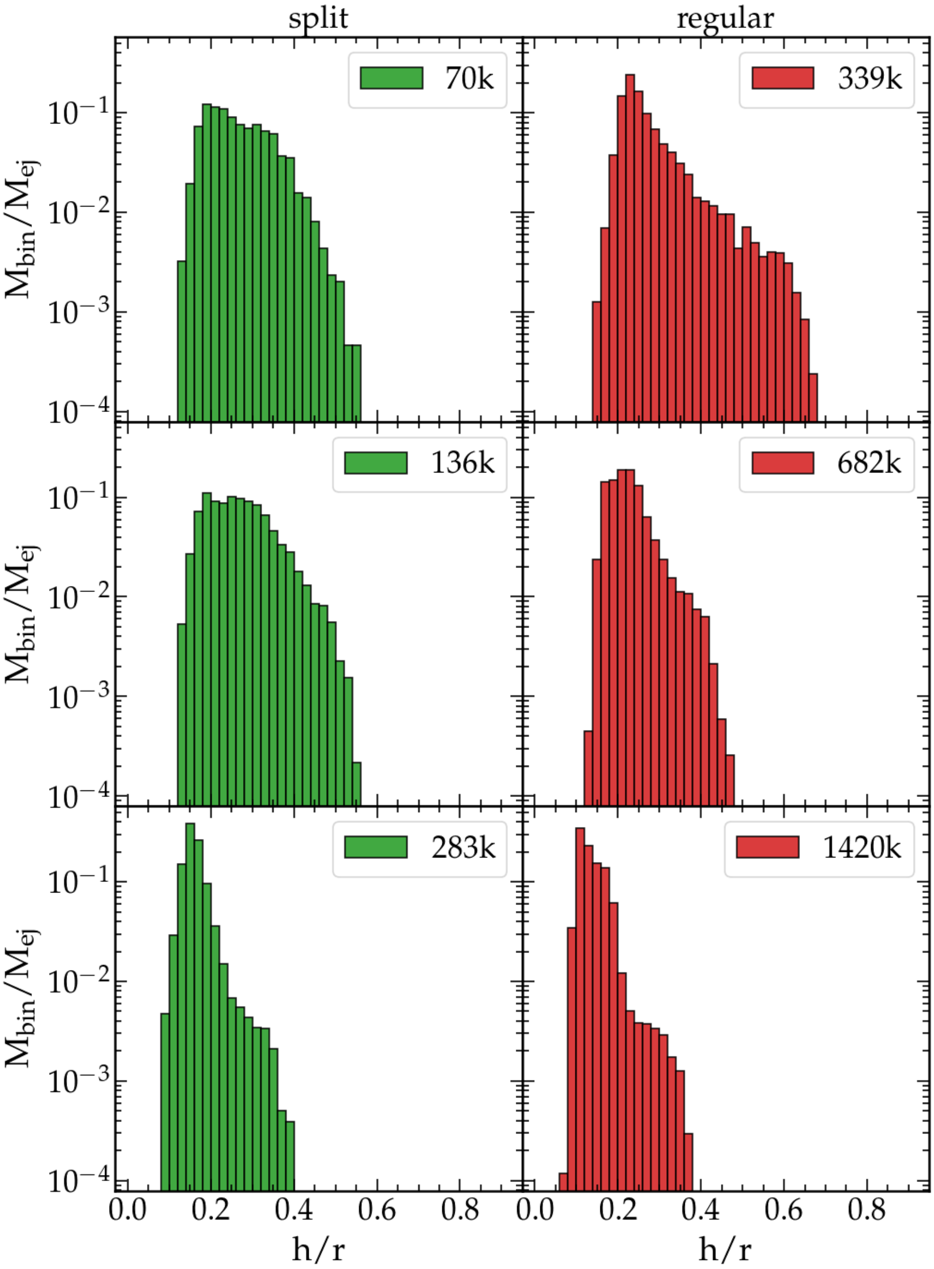

Figure 6.7.: Comparison of the ejecta smoothing length distribution between simulations with splitting (left) and fiducial simulations (right) for different particle numbers at around 25 ms after merger. Smoothing length is normalized to the distance of the particle distance to the center of mass.

7. Summary, conclusions and outlook

7.1. Conclusions

In this thesis, we addressed several challenges associated with simulating BNSM ejecta and focused on advancing the capabilities of numerical simulations.

First, we examined fluctuations in BNSM simulations, which occur even for a fixed physical and numerical setup. Collins et al. [143] were the first to discuss these variations and point out the possibility that these fluctuations might be a physical stochastic effect. We could show that the ejecta mass varies $\pm 25\%$ in our simulations for the same physical setup. Furthermore, also the ejecta distribution and symmetry as well as their velocity distribution vary. We found an antiproportional correlation between the amplitude of the main feature of the post-merger signal GW f_{peak} and the fluctuations of the ejecta mass. We showed that the fluctuations in ejecta mass and the f_{peak} amplitude were dependent on how the double core structure evolves. We tested how the spread of ejecta masses changes with different resolutions and did not see a reduction by increasing resolution. This might be a first indication that these variations are a physical effect. However, so far it is not possible to draw a clear conclusion. More research is needed, especially comparative studies between different numerical codes. This thesis was the first study to investigate the possibility of stochastic effects in BNSM. Several studies use numerical simulations to link the EoS and the amount of ejecta or kilonova light curves [104, 174, 202, 215–218]. Often, fit formulas are used to estimate the dynamical ejecta and disc ejecta from binary masses and tidal deformability. In future kilonova observations, the ejected mass is expected to be identified, and through the established correlations between the ejecta mass and the nuclear EoS, it will be possible to impose constraints on EoS. However, stochastic effects might make this route to constrain the EoS more challenging. Small perturbations from spin or magnetic fields of the NSs might play a crucial role in the evolution of the BNSM and the ejecta and therefore make direct fitting from ejecta mass to tidal deformability not possible. Also taking into account that we find up to 20 % variation in north-south symmetry gives the possibility that identical merger observed from the same inclination angle could have different kilonova light curves even if the total amount of ejecta is similar. So far studies which investigated correlations between ejecta mass and the EoS, have not discussed the possibility of stochastic fluctuations.

These studies acknowledge the fact that not all microphysical processes are included in numerical simulations and that the ejecta mass also depends on the resolution. Some estimate therefore an error of 50 % on the determined ejecta masses [104, 202, 217]. Whether this estimation is sufficient to also account for the fluctuation we observe for a fixed resolution is not clear. Even if the fluctuations we observe in our simulation are numerical, it is still important to take them into consideration when drawing conclusions from simulations. For a better understanding of the evolution of BNSM, future studies should take into account these fluctuations.

We address also long-term BNSM simulations, which are necessary to accurately describe kilonovae. Simulations that run only several tenths of milliseconds do not account for secular ejecta, which outflows over a significantly longer time scale than the merger time scale. In kilonova computations, determining the precise luminosities and their temporal evolution relies heavily on the total ejected matter. Additionally, radiative transfer models, which employ BNSM simulations as their initial data, operate under the assumption that the ejecta undergoes homologous expansion. Consequently, it is crucial to simulate BNSM over extended time scales to predict their electromagnetic counterpart signals. In chapter 4 we tackle two challenges in running long-term simulations. First, on a time scale of seconds the outflowing matter will change its density and temperature over several orders of magnitude. We present a method to extend a tabulated EoS towards lower values of rest-mass density and temperature. We see with our employed method a smooth continuation of the tabulated pressures and specific internal energies. Second, the expanding ejecta is phasing the problem of low resolution which increases numerical inaccuracy and can lead to nonphysical solutions, such as negative internal energies. We show that a different choice of discretization of the GRHD equations leads to a more stable evolution. A comparison between the old and new approach, using simulations of a $1.35 - 1.35 M_\odot$ symmetric binary merger system, reveal that the amount of SPH particles reaching nonphysical energies decreases from around 25% to under 10% of ejected matter.

We present a long-term simulation of a $1.35 - 1.35 M_\odot$ symmetric binary merger system using the extended EoS and improved discretization. We managed to evolve the complete system up to 250 ms after merger, which is an order of magnitude longer than our previous simulations. We are able to give an upper limit on how close outflowing material is to reach homologous expansion. We find that for 97% of the material ejected within the initial 25 ms after the merger, the maximum change in radial velocity is below 10% at the end of the simulation. Material ejected later moves more slowly and remains warmer, so its velocity is more affected by pressure work. It will take at least seconds for it to achieve homologous expansion. Previous studies mapped ejecta from BNSM simulations which only run roughly 20 ms into radial transfer code by propagating SPH particles at the velocity which they had at the end of the simulation further for 0.5 seconds [204, 205]. An other approach was to cut out the remnant in the hydrodynamic simulation and evolve only the ejecta further [207]. We compare the velocity distribution of the early ejecta at the end of our long-term simulation with other approaches to reach approximately homologous expansion. We see that assuming that velocity stays constant at early times and evolve matter ballistic gives similar results, but cutting out the central object and evolve only the ejecta further in the hydrodynamic simulation distort the velocity distribution. This is caused by the sudden lack of pressure support at the cut and even in higher resolution is the shift towards slower velocities significant for this method.

While our long-term simulation is a important step in the right direction, our results show that even longer simulations are needed. For that, resolution becomes a problem again for the continuously expanding matter. In our long-term simulation we started with 339×10^3 SPH particles, but only a few thousand particles are ejected. At some point, even with improved evolution, the numerical scheme will break down because of the lack of particles over the vast distances the material is expanding. However, increasing the total number of particles is very computational expensive and highly inefficient. In the last part of this thesis we introduce a way to increase the resolution efficiently only in the ejecta. We present particle splitting, which Kitsionas and Whitworth [213] introduced for resolution improvements in the context of star formation. So far this method was not employed for BNSMs simulations. We find comparable results in ejecta mass, angular and velocity distribution between simulations with 1420×10^3 particles and 283×10^3 using particle splitting, showing that we could improve the ejecta resolution by roughly a factor of 5.

In this work we did not consider the impact of neutrinos. One reason for it, especially for long-term simulations, is the high computational cost to include them. However, they are crucial for the evolution of the ejecta, the nucleosynthesis and the resulting kilonova. With particle splitting, this would be now be more approachable in the future. Starting with a lower total particle number but still having higher resolution in the ejecta saves computational costs and make it easier to conduct such demanding numerical simulations.

7.2. Outlook

We note that our study of stochastic effects in BNSM can at the moment only provide indications but not stronger statements. For possible more conclusive insights about this problem we plan for future studies to compare results of different codes to provide statements if the fluctuations we observe are code independent. Seeing the same effects in different simulation codes would strengthen the credibility, that what we observe in BNSM simulation is indeed a physical feature and not just numerical uncertainty. In this study we only simulated irrotational NSs. A additional method would also to simulate spinning NSs and see if these have an affect on the fluctuations.

Regarding our presented improvements of the SPH by implementing an extended EoS, using a more stable discretization of the energy equation and efficiently improving the ejecta resolution with particle splitting we plan to implement all these scheme also into the SPH code version which includes neutrino treatment. We pointed out that all this improvements are important for kilonova studies. To actually make full use of this results accurate neutrino transport is necessary. Our goals for the future are conducting high-resolution long-term BNSM simulations with neutrino treatment with an extensive analysis of the results with nucleosynthesis and radiative transfer calculations.

Future works can also improve some of the implemented schemes. A possible more consistent extension of the EoS can be implemented using a detailed composition for the extended part and also checking the treatment of correct coulomb corrections. The splitting scheme can be further improved, by trying to minimizing the impact of splitting on the particle neighbors. Taking the neighbors and the flow velocity into account by the positioning the daughter particles will decrease numerical noise.

Acknowledgments

First, I would like to thank my supervisor Gabriel Martínez-Pinedo for his patience and support over the last years which made it possible for me to write this thesis. He always made time for me when I needed it and gave me the guidance I needed. I am grateful for him being understanding, giving feedback and encouragement, especially in difficult times. I would like to express the same gratitude to Andreas Bauswein. He has helped me immensely over the last years with his patience, support and feedback. I would also like to thank Oliver Just, who was always willing to take the time to help me and discuss with me. Thanks to the many conversations and discussions with these three as supervisors, experts and mentors, I never gave up even in times when I doubted myself.

I would like to thank George Lioutas, Theodoros Soultanis, Vimal Vijayan, Sebastian Blacker and Mario Jakobs for all the nice discussions in the office, the exchange of knowledge and mutual support in our projects. Also a big thanks goes also to Thomas Neff for his aid on the aspects of working with a High-Performance computing cluster.

I want to thank the many more people at GSI who have made my work and life more enjoyable during the last years. I want to thank Ignacio, Zafar, Gerrit, Diana, Aris, Heamin, Marcel, Paul, Nithish, Chun Ming, Zewei, Luke, Andreas, Christine, Carsten, Xiao, Ninoy, Dag, Kevin and many others for insightful discussions about physics and our projects, for the small chats in office when one needs a break, for the hiking trips, for the dinners together, for the table tennis breaks after lunch, for all the enjoyable activities and shared memories.

I want to thank the TU Darmstadt, GSI and its R & D Program, as well as the HGS-HIRe program for the possibility to doctorate, for the financial support and for providing an excellent workspace and computational resources.

Last but not least I want to thank Katja Bauschinger for helping me dealing with my self-doubt and finding a way to finish this thesis.

Appendices

A. GRHD equations in co-moving frame

In the following we derive GRHD equation used in the SPH code, starting from the Valencia formulation in the form

$$\partial_0\left(\sqrt{\gamma}\mathbf{U}\right)+\partial_i\left(\sqrt{\gamma}\mathbf{F}^i\right)=\mathbf{S}, \tag{A.1}$$

with the conserved quantities

$$\mathbf{U}\left(\mathbf{W}\right)=\begin{pmatrix} D \\ S_i \\ \tilde{\tau} \end{pmatrix}=\begin{pmatrix} \rho W \\ \rho h W^2 \bar{v}_i \\ \rho h W^2-\rho-D \end{pmatrix}, \tag{A.2}$$

where $W=\alpha u^0=(1-\gamma_{ij}\bar{v}^i\bar{v}^j)^{-1/2}$ is the Lorentz factor. The vector $\mathbf{F}^i$ corresponds to the flux of conserved variables

$$\mathbf{F}^i=\alpha\begin{pmatrix} D\left(\bar{v}^i-\frac{\beta^i}{\alpha}\right) \\ S_j\left(\bar{v}^i-\frac{\beta^i}{\alpha}\right)+P\gamma^i_j \\ \tilde{\tau}\left(\bar{v}^i-\frac{\beta^i}{\alpha}\right)+P\bar{v}^i \end{pmatrix} \tag{A.3}$$

and $\mathbf{S}$ to the source vector

$$\mathbf{S}=\sqrt{\gamma}\begin{pmatrix} 0 \\ \frac{1}{2}\alpha S^{ik}\partial_j\gamma_{ik}+S_i\partial_j\beta^i-E\partial_j\alpha \\ \alpha S^{ij}K_{ij}-S^j\partial_j\alpha \end{pmatrix}, \tag{A.4}$$

with $E=\tilde{\tau}+D$, $S^{ij}:=\gamma^i_a\gamma^j_b T^{ab}=\rho h W^2\bar{v}^i\bar{v}^j+P\gamma^{ij}$ the projection of $\mathbf{T}$ in the space orthogonal to $\mathbf{n}$ and $K_{ij}:=-\frac{1}{2}\left(\gamma^a_i\nabla_a n_j+\gamma^a_j\nabla_a n_i\right)$ the extrinsic curvature. If we look at the first component we get the equation related to the conserved rest mass density

$$\partial_0\left(\sqrt{\gamma}D\right)+\partial_i\left(\sqrt{\gamma}\alpha D\left[\bar{v}^i-\frac{\beta^i}{\alpha}\right]\right)=0 \tag{A.5}$$

The differential operator ∂_0 can be expressed as

$$\partial_0=\frac{d}{dt}-\frac{u^i}{u^0}\partial_i \tag{A.6}$$

in the co-moving reference frame. We can also define the conserved rest mass density as $\rho^* = \sqrt{\gamma}D = \sqrt{\gamma}\rho W$. With that we can write (A.5) as

$$\begin{aligned}
&\frac{d\rho^*}{dt} - \frac{u^i}{u^0}\partial_i\rho^* + \partial_i\left(\alpha\rho^*\left[\bar{v}^i - \frac{\beta^i}{\alpha}\right]\right) = \\
&\frac{d\rho^*}{dt} - \frac{u^i}{u^0}\partial_i\rho^* + \partial_i\left(\rho^*\left[\frac{u^i}{u^0} + \beta^i - \beta^i\right]\right) = \\
&\frac{d\rho^*}{dt} - \frac{u^i}{u^0}\partial_i\rho^* + \rho^*\partial_i\frac{u^i}{u^0} + \frac{u^i}{u^0}\partial_i\rho^* = \\
&\frac{d\rho^*}{dt} + \rho^*\partial_i\frac{u^i}{u^0} = 0,
\end{aligned} \tag{A.7}$$

where we used the definition of the 3-velocity $\bar{v}^i = \frac{1}{\alpha}\left(\frac{u^i}{u^0} + \beta^i\right)$. With the definition of the coordinate velocity $v^i = \frac{u^i}{u^0}$ we get the equation

$$\frac{d\rho^*}{dt} = -\rho^*\partial_i v^i \tag{A.8}$$

The second component is the conserved momentum density equation with

$$\partial_0\left(\sqrt{\gamma}S_i\right) + \partial_i\left(\sqrt{\gamma}\alpha S_j\left[\bar{v}^i - \frac{\beta^i}{\alpha}\right] + \sqrt{\gamma}\alpha P\gamma^i_j\right) = \frac{1}{2}\alpha S^{ik}\partial_j\gamma_{ik} + S_i\partial_j\beta^i - E\partial_j\alpha. \tag{A.9}$$

We use (A.6) again and simplify the left-hand side of (A.9) with $\sqrt{\gamma}S_i = \sqrt{\gamma}\rho h W^2\bar{v}_i = \rho^*\hat{u}_i$ and the 3-velocity again.

$$\begin{aligned}
&\partial_0\left(\rho^*\hat{u}_i\right) + \partial_i\left(\rho^*\hat{u}_j\alpha\left[\bar{v}^i - \frac{\beta^i}{\alpha}\right] + \sqrt{\gamma}\alpha P\gamma^i_j\right) = \\
&\frac{d}{dt}\left(\rho^*\hat{u}_i\right) - \frac{u^i}{u^0}\partial_i\left(\rho^*\hat{u}_i\right) + \partial_i\left(\rho^*\hat{u}_j\alpha\left[\frac{u^i}{\alpha u^0} + \frac{\beta}{\alpha} - \frac{\beta^i}{\alpha}\right] + \sqrt{\gamma}\alpha P\gamma^i_j\right) = \\
&\hat{u}_i\frac{d\rho^*}{dt} + \rho^*\frac{\hat{u}_i}{dt} - \frac{u^i}{u^0}\partial_i\left(\rho^*\hat{u}_i\right) + \partial_i\left(\rho^*\hat{u}_j\frac{u^i}{u^0} + \sqrt{\gamma}\alpha P\gamma^i_j\right) = \\
&-\hat{u}_i\rho^*\partial_i\left(\frac{u^i}{u^0}\right) + \rho^*\frac{\hat{u}_i}{dt} - \frac{u^i}{u^0}\partial_i\left(\rho^*\hat{u}_i\right) + \frac{u^i}{u^0}\partial_i\left(\rho^*\hat{u}_i\right) + \hat{u}_i\rho^*\partial_i\left(\frac{u^i}{u^0}\right) + \partial_i\left(\sqrt{\gamma}\alpha P\gamma^i_j\right) = \\
&\rho^*\frac{\hat{u}_i}{dt} + \partial_i\left(\sqrt{\gamma}\alpha P\gamma^i_j\right),
\end{aligned} \tag{A.10}$$

where we used Eq. (A.8) for $\hat{u}_i\frac{d\rho^*}{dt}$. For the right-hand side we insert the definition of S^{ij},S_i and E and we get

$$
\begin{aligned}
&\frac{1}{2}\sqrt{\gamma}\alpha S^{ik}\partial_j\gamma_{ik} + \sqrt{\gamma}S_i\partial_j\beta^i - \sqrt{\gamma}E\partial_j\alpha = \\
&\frac{1}{2}\sqrt{\gamma}\alpha\left(\rho h W^2\bar{v}^i\bar{v}^k + P\gamma^{ik}\right)\partial_j\gamma_{ik} + \sqrt{\gamma}\rho h W^2\bar{v}_i\partial_j\beta^i - \sqrt{\gamma}\rho h W^2\partial_j\alpha + \sqrt{\gamma}P\partial_j\alpha = \\
&\frac{1}{2}\left(\frac{\rho^*\gamma^{ij}\hat{u}_j\gamma^{kl}\hat{u}_l}{\hat{u}^0} + \sqrt{\gamma}\alpha P\gamma^{ik}\right)\partial_j\gamma_{ik} + \rho^*\hat{u}_i\partial_j\beta^i - \rho^*\alpha\hat{u}^0\partial_j\alpha + \sqrt{\gamma}P\partial_j\alpha = \\
&\frac{\rho^*\gamma^{ij}\hat{u}_j\gamma^{kl}\hat{u}_l}{2\hat{u}^0}\partial_j\gamma_{ik} + \frac{1}{2}\sqrt{\gamma}\alpha P\gamma^{ik}\partial_j\gamma_{ik} + \rho^*\hat{u}_i\partial_j\beta^i - \rho^*\alpha\hat{u}^0\partial_j\alpha + \sqrt{\gamma}P\partial_j\alpha.
\end{aligned}
\tag{A.11}
$$

Now we can put everything but $\frac{d\hat{u}_i}{dt}$ on the right-hand side and use the conformal flatness condition $\gamma_{ij} = \psi^4\delta_{ij}$ to simplify to

$$
\begin{aligned}
\frac{d\hat{u}_i}{dt} &= \\
&= -\frac{1}{\rho^*}\partial_i\left(\sqrt{\gamma}\alpha P\gamma^i_j\right) + \frac{\gamma^{ij}\hat{u}_j\gamma^{kl}\hat{u}_l}{2\hat{u}^0}\partial_j\gamma_{ik} + \frac{1}{2\rho^*}\sqrt{\gamma}\alpha P\gamma^{ik}\partial_j\gamma_{ik} + \hat{u}_i\partial_j\beta^i \\
&\quad - \alpha\hat{u}^0\partial_j\alpha + \frac{1}{\rho^*}\sqrt{\gamma}P\partial_j\alpha \\
&= -\frac{1}{\rho^*}\alpha P\gamma^i_j\partial_i\sqrt{\gamma} - \frac{1}{\rho^*}\sqrt{\gamma}P\gamma^i_j\partial_i\alpha - \frac{1}{\rho^*}\sqrt{\gamma}\alpha\gamma^i_j\partial_i P - \frac{1}{\rho^*}\sqrt{\gamma}\alpha P\partial_i\gamma^i_j \\
&\quad + \frac{\gamma^{ij}\hat{u}_j\gamma^{kl}\hat{u}_l}{2\hat{u}^0}\partial_j\gamma_{ik} + \frac{1}{2\rho^*}\sqrt{\gamma}\alpha P\gamma^{ik}\partial_j\gamma_{ik} + \hat{u}_i\partial_j\beta^i - \alpha\hat{u}^0\partial_j\alpha + \frac{1}{\rho^*}\sqrt{\gamma}P\partial_j\alpha \\
&= -\frac{1}{\rho^*}\psi^6\alpha\partial_j P - \frac{6}{\rho^*}\psi^5\alpha P\partial_i\psi + \frac{4}{\rho^*}\psi^5\alpha P\partial_i\psi + \frac{2\hat{u}_k\hat{u}_k}{\psi^5\hat{u}^0}\partial_j\psi \\
&\quad + \frac{2}{\rho^*}\psi^5\alpha P\partial_j\psi + \hat{u}_i\partial_j\beta^i - \alpha\hat{u}^0\partial_j\alpha.
\end{aligned}
\tag{A.12}
$$

With that we get the conserved momentum equation in the form

$$
\frac{d\hat{u}_i}{dt} = -\frac{1}{\rho^*}\psi^6\alpha\partial_i P + \hat{u}_j\partial_i\beta^j - \alpha\hat{u}^0\partial_i\alpha + \frac{2\hat{u}_k\hat{u}_k}{\psi^5\hat{u}^0}\partial_i\psi. \tag{A.13}
$$

For the conserved energy density equation we look at the third component, where we have

$$
\partial_0\left(\sqrt{\gamma}\tilde{\tau}\right) + \partial_i\left(\sqrt{\gamma}\alpha\tilde{\tau}\left[\bar{v}^i - \frac{\beta^i}{\alpha}\right] + \sqrt{\gamma}\alpha P v^i\right) = \alpha S_{ij}K^{ij} - S^j\partial_j\alpha. \tag{A.14}
$$

Similar to the conserved momentum equation we use here on the left-hand side

$$
\sqrt{\gamma}\tilde{\tau} = \frac{\rho^*}{\rho W}\left(\rho h W^2 - P - \rho W\right) = \rho^*\left(hW - \frac{P}{\rho W} - 1\right) = \rho^*\tau^0 \tag{A.15}
$$

with τ^0 the specific total conserved energy to use (A.8) again. Now we can simplify the left-hand side to

$$\begin{aligned}
&\partial_0\left(\rho^*\tau^0\right)+\partial_i\left(\rho^*\alpha\tau^0\left[\bar{v}^i-\frac{\beta^i}{\alpha}\right]+\sqrt{\gamma}\alpha P\bar{v}^i\right)=\\
&\rho^*\frac{d\tau^0}{dt}+\tau^0\frac{d\rho^*}{dt}-\frac{u^i}{u^0}\partial_i\left(\rho^*\tau^0\right)+\partial_i\left(\rho^*\tau^0\frac{u^i}{u^0}\right)+\partial_i\left(\sqrt{\gamma}P\left[\frac{u^i}{u^0}+\beta^i\right]\right)=\\
&\rho^*\frac{d\tau^0}{dt}-\tau^0\rho^*\partial_i\left(\frac{u^i}{u^0}\right)-\frac{u^i}{u^0}\partial_i\left(\rho^*\tau^0\right)+\partial_i\left(\rho^*\tau^0\frac{u^i}{u^0}\right)+\partial_i\left(\sqrt{\gamma}P\left[\frac{u^i}{u^0}+\beta^i\right]\right)=\\
&\rho^*\frac{d\tau^0}{dt}+\partial_i\left(\sqrt{\gamma}P\left[\frac{u^i}{u^0}+\beta^i\right]\right).
\end{aligned}\tag{A.16}$$

For the right-hand side we can first use the definition of S_{ij} and S^j to get

$$\begin{aligned}
&\sqrt{\gamma}\alpha S_{ij}K^{ij}-\sqrt{\gamma}S^j\partial\alpha=\\
&\sqrt{\gamma}\alpha\left(\rho hW^2\bar{v}_i\bar{v}_j+P\gamma_{ij}\right)K^{ij}-\sqrt{\gamma}\rho hW^2\bar{v}^j\partial_j\alpha=\\
&\left(\rho^*\alpha Wh\frac{u_i}{W}\frac{u_j}{W}+\sqrt{\gamma}\alpha P\gamma_{ij}\right)K^{ij}-\rho^*\gamma^{jl}\bar{v}_l\partial_j\alpha=\\
&\rho^*\frac{\hat{u}_i\hat{u}_j}{hu^0}K^{ij}+\sqrt{\gamma}\alpha PK_i^i-\rho^*\gamma^{jl}\hat{u}_l\partial_j\alpha=\\
&\rho^*\frac{\hat{u}_i\hat{u}_j}{hu^0}K^{ij}-\rho^*\gamma^{jl}\hat{u}_l\partial_j\alpha
\end{aligned}\tag{A.17}$$

Both together leads to

$$\frac{d\tau^0}{dt}=-\frac{1}{\rho^*}\partial_i\left(\sqrt{\gamma}P\left[v^i+\beta^i\right]\right)+\frac{\hat{u}_i\hat{u}_j}{hu^0}K^{ij}-\gamma^{jl}\hat{u}_l\partial_j\alpha.\tag{A.18}$$

This is the evolution equation for τ^0, but in simulations with the SPH code was shown that in regions where the kinetic energy dominates evolving a conserved energy where a kinetic energy term is subtracted yields to more accurate results [42]. Originally it was defined as

$$\tau_{orig}=hW-\frac{P}{\rho W}-\frac{1}{2}\gamma^{ij}\hat{u}_i\hat{u}_j,\tag{A.19}$$

but to improve numerical stability it was in early studies changed to

$$\tau=hW-\frac{P}{\rho W}-\sqrt{1+\gamma^{ij}\hat{u}_i\hat{u}_j}\tag{A.20}$$

[219]. So for going from (A.18) to the evolution equation of τ, we can first use the CFC approximation again, and with that the fact that the extrinsic curvature K_{ij} can be calculated directly from the metric elements

$$2\alpha\psi^4 K^{ij} = \delta^{il}\partial_j\beta^l + \delta_{jl}\partial_i\beta^l - \frac{2}{3}\delta^{ij}\partial_k\beta^k. \tag{A.21}$$

With that we have

$$\begin{aligned}\frac{d\tau^0}{dt} = &-\frac{\psi^6}{\rho^*}\left(v^i+\beta^i\right)\partial_i P \\ &-\psi^6\frac{P}{\rho^*}\partial_i\left(v^i+\beta^i\right) \\ &-6\psi^5\frac{P}{\rho^*}\left(v^i+\beta^i\right)\partial_i\psi \\ &-\frac{\hat{u}_i}{\psi^4}\partial_i\alpha \\ &+\frac{1}{\psi^4}\frac{1}{hW}\left(\hat{u}_i\hat{u}_j\partial_j\beta^i - \frac{1}{3}\hat{u}_i\hat{u}_i\partial_j\beta^j\right).\end{aligned} \tag{A.22}$$

Since $\tau = \tau^0 + 1 - \omega$, where we define the kinetic term $\omega = \sqrt{1+\frac{\delta^{ij}\hat{u}_i\hat{u}_j}{\psi^4}}$. We can write the time derivative of τ as

$$\begin{aligned}\frac{d\tau}{dt} &= \frac{d\tau^0}{dt} + \frac{d}{dt}\left[1-\omega\right] \\ &= \frac{d\tau^0}{dt} - \frac{1}{2\omega}\frac{d}{dt}\left[\frac{\delta^{ij}\hat{u}_i\hat{u}_j}{\psi^4}\right] \\ &= \frac{d\tau^0}{dt} - \frac{1}{2\omega}\left[\frac{2}{\psi^4}\hat{u}_j\frac{d\hat{u}_i}{dt} - \frac{4\hat{u}_i\hat{u}_j\delta^{ij}}{\psi^5}\frac{d\psi}{dt}\right]\end{aligned} \tag{A.23}$$

At this point we have time derivatives on the right-hand side, one for the conserved momentum and one for ψ. For the first we can insert Eq. (A.13), for the latter we can use a relation from the CF approximation (see e.g. [168] Eq. B.2)

$$\partial_0\psi = \frac{\psi}{6}\partial_k\beta^k + \left(\partial_k\psi\right)\beta^k, \tag{A.24}$$

and Eq. (A.6). Applying these leads us to

$$
\begin{aligned}
\frac{d\tau}{dt} &= \frac{d\tau^0}{dt} - \frac{1}{\omega}\frac{\delta^{ij}\hat{u}_j}{\psi^4}\left(-\frac{1}{\rho^*}\alpha\psi^6\partial_i P - h\alpha u^0\partial_i\alpha - \hat{u}_j\partial_i\beta^j + \frac{2\hat{u}_k\hat{u}_k}{hu^0\psi^5}\partial_i\psi\right) \\
&\quad + \frac{2}{\omega}\frac{\hat{u}_i\hat{u}_j\delta^{ij}}{\psi^5}\left(\partial_0\psi + v^i\partial_i\psi\right) \\
&= \frac{d\tau^0}{dt} + \frac{\psi^6}{\rho^*}\frac{\hat{u}_i\alpha}{\omega\psi^4}\partial_i P + \frac{hW}{\omega}\frac{\hat{u}_i}{\psi^4}\partial_i\alpha - \frac{1}{\psi^4}\frac{1}{\omega}\hat{u}_i\hat{u}_j\partial_i\beta^j - \frac{1}{\omega}\frac{\hat{u}_i}{\psi^4}\frac{2\hat{u}_k\hat{u}_k}{hu^0\psi^5}\partial_i\psi \qquad \text{(A.25)} \\
&\quad + \frac{2}{\omega}\frac{\hat{u}_i\hat{u}_i}{\psi^5}\left[\frac{\psi}{6}\partial_k\beta^k + \left(\partial_k\psi\right)\beta^k\right] + v^i\frac{1}{\omega}\frac{2\hat{u}_k\hat{u}_k}{\psi^5}\partial_i\psi \\
&= \frac{d\tau^0}{dt} + \frac{\psi^6}{\rho^*}\left(v^i + \beta^i\right)\frac{hW}{\omega}\partial_i P + \frac{\hat{u}_i}{\psi}\frac{hW}{\omega}\partial_i\alpha - \frac{1}{\psi^4}\frac{1}{\omega}\hat{u}_i\hat{u}_j\partial_i\beta^j \\
&\quad - \frac{1}{\omega}\left(v^i + \beta^i\right)\frac{2\hat{u}_k\hat{u}_k}{\psi^5}\partial_i\psi + \frac{1}{\psi^4}\frac{1}{\omega}\frac{1}{3}\hat{u}_i\hat{u}_i\partial_k\beta^k + \frac{1}{\omega}\left(v^i + \beta^k\right)\frac{2\hat{u}_i\hat{u}_i}{\psi^5}\partial_k\psi \\
\\
&= \frac{d\tau^0}{dt} - \frac{\psi^6}{\rho^*}\left(v^i + \beta^i\right)\frac{hW}{\omega}\partial_i P + \frac{\hat{u}_i}{\psi}\frac{hW}{\omega}\partial_i\alpha - \frac{1}{\psi^4}\frac{1}{\omega}\left(\hat{u}_j\hat{u}_i\partial_i\beta^i - \frac{1}{3}\hat{u}_i\hat{u}_i\partial_k\beta^k\right).
\end{aligned}
$$

If we compare the additional terms with Eq. (A.22) we see that they only differ by the factor of $\frac{hW}{\omega}$ from the terms in $\dfrac{d\tau^0}{dt}$. So we can simplify it to

$$
\begin{aligned}
\frac{d\tau}{dt} = &- \frac{\psi^6}{\rho^*}\left(v^i + \beta^i\right)\left(1 - \frac{hW}{\omega}\right)\partial_i P - \psi^6\frac{P}{\rho^*}\partial_i\left(v^i + \beta^i\right) \\
&- 6\psi^5\frac{P}{\rho^*}\left(v^i + \beta^i\right)\partial_i\psi - \frac{\hat{u}_i}{\psi^4}\left(1 - \frac{hW}{\omega}\right)\partial_i\alpha \\
&+ \frac{1}{\psi^4}\left(\frac{1}{hW} - \frac{1}{\omega}\right)\left(\hat{u}_i\hat{u}_j\partial_j\beta^i - \frac{1}{3}\hat{u}_i\hat{u}_i\partial_j\beta^j\right).
\end{aligned}
\tag{A.26}
$$

The new set of conserved quantities are now

$$
\begin{pmatrix} \rho^* \\ \hat{u}_i \\ \tau \end{pmatrix} = \begin{pmatrix} \rho W\psi^6 \\ \rho h\left(v^i + \beta^i\right)u^0\psi^4 \\ \rho hW - \frac{P}{\rho W} - \sqrt{1 + \gamma^{ij}\hat{u}_i\hat{u}_j} \end{pmatrix}
\tag{A.27}
$$

and the GRHD equations are

$$
\frac{d\rho^*}{dt} = -\rho^*\partial_i v^i,
$$

$$
\frac{d\hat{u}_i}{dt} = -\frac{1}{\rho^*}\alpha\psi^6\partial_i P - \alpha\hat{u}^0\partial_i\alpha + \hat{u}_j\partial_i\beta^j + \frac{2\hat{u}_j\hat{u}_j}{\psi^5\hat{u}^0}\partial_i\psi
\tag{A.28}
$$

$$
\begin{aligned}
\frac{d\tau}{dt} = & -\frac{\psi^6}{\rho^*}\left(v^i+\beta^i\right)\left(1-\frac{hW}{\omega}\right)\partial_i P - \psi^6\frac{P}{\rho^*}\partial_i\left(v^i+\beta^i\right) \\
& - 6\psi^5\frac{P}{\rho^*}\left(v^i+\beta^i\right)\partial_i\psi - \frac{\hat{u}_i}{\psi^4}\left(1-\frac{hW}{\omega}\right)\partial_i\alpha \\
& + \frac{1}{\psi^4}\left(\frac{1}{hW}-\frac{1}{\omega}\right)\left(\hat{u}_i\hat{u}_j\partial_j\beta^i - \frac{1}{3}\hat{u}_i\hat{u}_i\partial_j\beta^j\right).
\end{aligned}
$$

B. Ejecta criteria

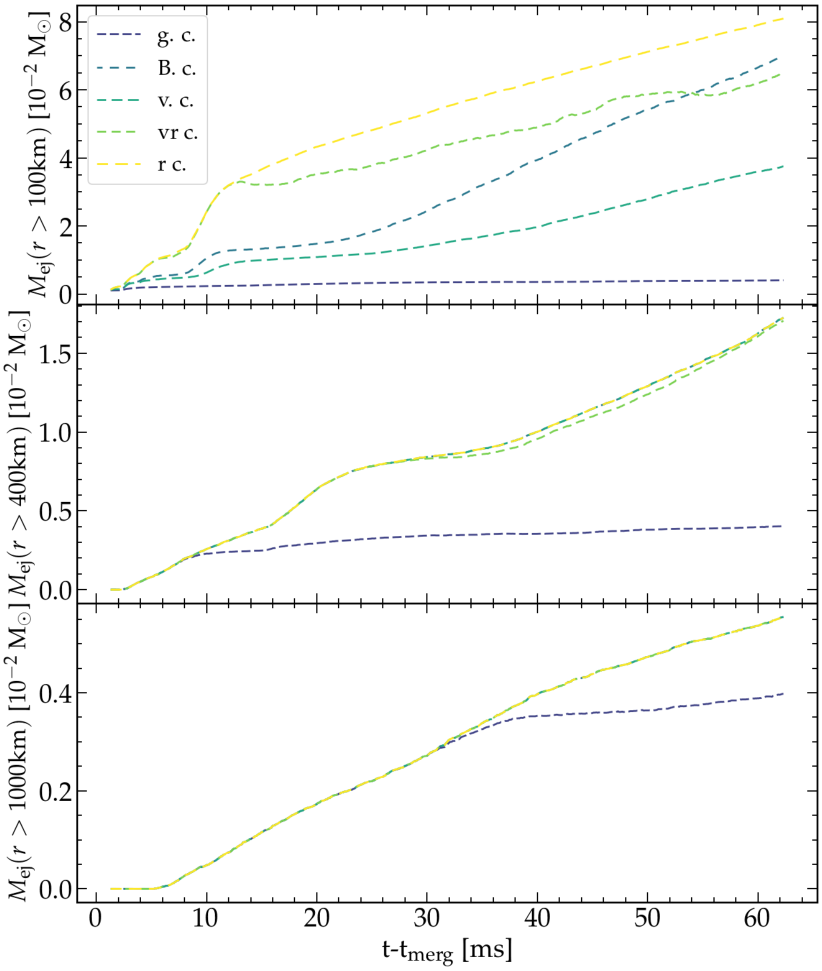

Figure B.1.: Ejecta over time for three different radial cuts (upper panel 100 km, middle panel 400 km, lower panel 1000 km) for different ejecta criteria (geodesic criterion (g. c.) - indigo line, Bernoulli criterion (B. c.) - teal line, virial criterion (v. c.) - turquoise line, radial velocity criterion (vr c.) - green line and all matter outside the radius (r c.) - yellow line).

When it comes to identifying ejecta, one need to be aware of the differences of the different criteria and what impact this can have on interpreting data. In section 2.3.3 we introduced already geodesic, Bernoulli and virial criteria, the latter is the criterion we chose to use in this work. As seen in Chapter 3, 4 and 5 we additionally look only look at material outside a certain radius for comparing ejecta from different simulations. The reason is, that each criterion has its short comings in deciding if a SPH particle is unbound or not, especially in highly dynamic environment. Further out of the system, where matter flow is less turbulent it is for the criteria easier to identify correctly unbound matter. As an example we take the simulation from section 4.2.2 with asymmetric discretization and show in figure B.1 evolution of the amount of ejecta over time for different criteria and three different radial cuts. The indigo line depicts the geodesic criterion, teal line the Bernoulli criterion, turquoise line the virial criterion and besides these three criteria shows the lime-green line how much material has a positive radial velocity and the yellow line how much material in total is outside the radial cut. The upper panel shows how much matter is identified as ejecta outside a radius of 100 km. In the first few milliseconds the different criteria disperse already. The torus around the remnant expands with hot shock heated material in it. The geodesic criterion only registers the very early dynamical outflow which moves ballistically out of the system before the torus forms. virial criterion registers also some hot disc material, and even more so the Bernoulli criterion. Most of the disc amount has an positive radial velocity component but at late times the Bernoulli criterion even defines material without that as ejecta. Comparing the middle and lower panel shows that further out the agreement between the different criteria increases.

Outside 1000 km all the criteria agree with each other except at later times the geodesic criterion which will at least within this 60 ms converge to $4 \cdot 10^{-3} \mathrm{M}_{\odot}$. This far out all material is ejecta, as can be seen by the overlap with the yellow line. We therefore choose typically a radial cut of 1000 km to compare ejection rate of different simulations. In some cases it still can be useful to look also at smaller radial cuts to compare how much material is in the torus or how fast the torus is expanding, as we did it for the stochasticity study in section 3.1. We want to note that the differences in ejecta between criteria is mainly due to not having long enough simulations to predict correctly how much material will be eventually ejected. Over a longer duration all the differences between the criteria will vanish, at the latest when all ejecta will reach homologous expansion.

C. Impact of Artificial viscosity

At the start of chapter 3 we mentioned uncertainties in the ejecta mass of numerical simulation because of limited resolution. In 3.2 we discussed that there exist fluctuations at a fixed setup which could be numerical but might be even a physical phenomenon. In this section we want to look into a model dependent uncertainty, the artificial viscosity scheme. Unlike in the last section, this is certain a purely numerical effect. Specifically, we want to look into the dissipation.

While SPH have many advantages compared to grid based simulations, one major disadvantage for simulating BNSM is that shocks can not be directly captured. Shock fronts are hydrodynamic discontinuities propagating supersonically through the medium. Through the smoothing process in SPH would be any discontinuity smoothed out. The artificial viscosity scheme outlined in 2.3.2 is crucial for accurately capturing shocks, a key aspect of modeling ejecta outflows. While grid-based codes resolve shocks with higher fidelity, they still suffer from systematic errors from shock-capturing schemes ([220]).

As the name suggests this scheme does not mimic physical viscosity on a microscopic scale but rather add an artificial dissipation term, which ensures that shock-waves are treated correctly. This means that entropy increases in shocks and dissipation occurs in shock fronts. But the artificial viscosity is not everywhere wanted, because in general artificial viscosity smooths out velocity and density distributions. That is why the scheme uses time dependent dissipation parameters. Dissipation is for each particle activated through a trigger which activates where dissipation is needed (in this case the velocity divergence is used as trigger). After the trigger increased the dissipation parameter ξ its value decays back to the floor value.

$$\frac{d\xi}{dt} = -\frac{\xi - \xi^0}{\tau_{\text{visc}}}, \tag{C.1}$$

where ξ^0 is the floor value. This is managed by a decay timescale

$$\tau_{\text{visc}} = \frac{h}{C_1 c_v}, \tag{C.2}$$

with the free parameter C_1. These two free parameters ξ^0 and C_1 have to be chosen. In [165] the idea of time-dependent viscosity parameter was introduced for SPH. The parameters were determined by standard hydrodynamical shock tests. Dissipation depends on the speed of sound, heat conductivity and viscosity of the medium. For NS matter these parameters are poorly constraint and so dissipation is.

Table C.1.: set of simulations with different artificial viscosity parameters. Table show set of parameters, ending time of the simulation and the amount of ejecta outside a radius of 1000 km. Some simulations with very high or low dissipation time C_1 terminated at during the merger.

C_1	ξ^0	$t - t_{\rm merg}$ [ms]	$M_{\rm ej}$ [$10^{-3}{\rm M}_\odot$]
0.5	0.01	14.85	6.68
0.5	0.02	0.20	–
0.5	0.005	0.09	–
0.25	0.01	20.81	8.56
0.25	0.02	23.61	8.04
0.25	0.005	22.16	8.69
0.1	0.01	20.15	6.96
0.1	0.02	20.67	5.06
0.1	0.005	21.30	5.96
0.05	0.01	25.02	4.32
0.025	0.01	23.22	4.06
0.025	0.02	16.67	2.43
0.025	0.005	18.21	2.94
0.01	0.01	23.60	3.13
0.01	0.02	25.06	3.28
0.01	0.005	10.99	1.30
0.005	0.01	20.82	3.00
0.005	0.02	25.02	3.41
0.005	0.005	0.30	–

In the following we test the impact on varying these two parameters on the BNSM simulations, not to dismiss or improve their chosen values but as a test to understand how sensitive the outcome is dependent on those parameters. We run 19 simulations from which 16 reached the post merger phase. We set them up to run up to roughly 20 ms after merger. For some chosen values of C_1 and ξ^0 lead to extreme values of ξ for certain SPH particles in shock regions, which lead in some occasions to nonphysical values of energy or momentum and caused the simulation to stop. 3 simulations with the most extreme values of C_1 stopped around the merger phase, 4 simulations did not reach 20 ms after merger. We take a standard setup of 1.35-1.35 M$_\odot$ system with 339×10^3 particles.

Table C.1 lists the chosen values of C_1 and ξ^0, how long each simulation run, and the ejected mass (r>1000 km). We decide here for a cut off of 1000 km, since we expect two effects by changing the viscosity. One is changing the amount of viscous heating which will change thermal outflows. Second is changing the lifetime of tidal arms which will change amount of dynamical outflows and shock heated outflows. Our ejecta criterion is prone to identify hot material as unbound. Even when this material has enough energy to overcome the gravitational potential, since it mostly thermal energy it still remains bound. With a greater radial cut we can make sure that we identify really only unbound material. Thereby we avoid identifying higher amount of hot material as higher amount of ejecta outflows. One can see from the table that for higher C_1 an increased amount of ejecta. While decreasing C_1 from its default value 0.05 decreases it at first but after reaching minimum at 0.01 there is a upwards trend again. In figure C.1 the evolution of ejecta is shown for radial cut at 100 km and 1000 km. In both cases the same trend is visible, that for high C_1 the rate of ejecta is increased. A minimal ejecta rate is reached for $C_1 =$ 0.01 and for lower values the rate of ejection increases again. C_1 regulates how fast after a shock the particle dissipation parameter ξ decays back to its default value ξ^0. Higher values of C_1 results in a faster decay of the dissipation after a shock. If the material stays for longer time highly viscous more kinetic energy converts to thermal energy. Especially at early times this weakens dynamical outflow and the formation of spiral arms. While thermal energy close to the remnant plays at early times only a subdominant role for ejecta and gets more important at later times further outside the remnant for thermal disc outflows. Only for $C_1 <$ 0.01 one can see an increase in ejecta for $r > 100$ km which is for $r > 1000$ km negligible.

We see that already at 5 ms seconds there is a factor three difference in ejecta between the different simulations. Comparing left and right panel shows the same trend can be seen, and hot material identified as ejecta do not play a crucial role here in this comparison. We show the difference in ξ^0 by solid, dashed, and dashed-dotted lines for values of 0.01, 0.02 and 0.005 respectively. We do not see a clear trend between different floor values ξ^0 for a chosen value of C_1. However, we recognize that for higher value of C_1 the spread in ejecta masses for different ξ^0 increases, while for very low values like $C_1 = 0.01$ there are only negligible differences between simulations.

This indicates, that the impact of ξ^0 on the system evolution depends on the dissipation decay time. For a longer dissipation decay time more particles stay above the floor value ξ^0 for a longer duration, so the impact of the high dissipation particles dominates and the effect of the dissipation at the floor value is negligible. When dissipation decays fast the impact of dissipation during shocks is suppressed and the dissipation due to the floor value which happens everywhere has a relatively stronger impact.

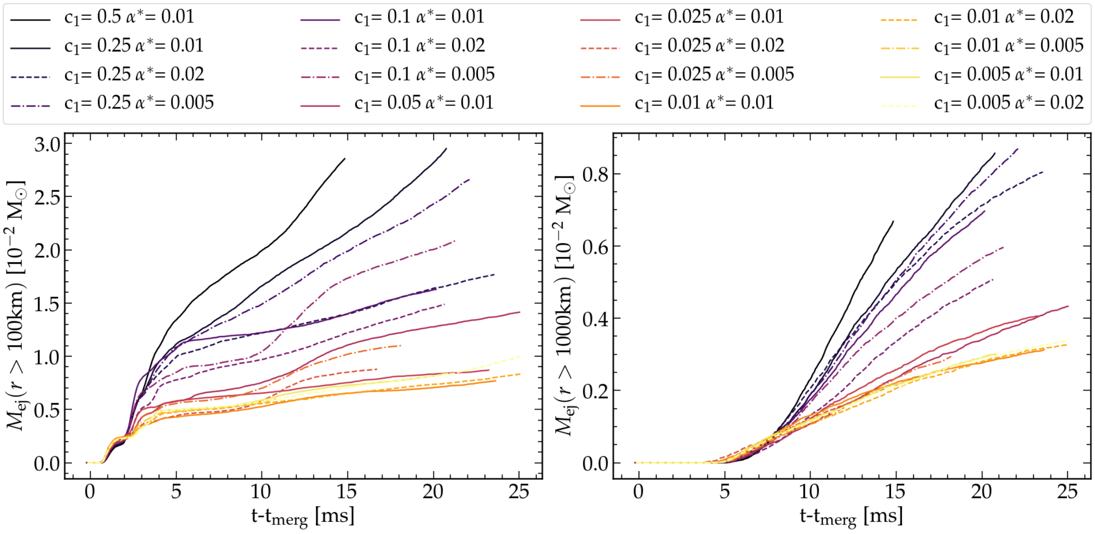

Figure C.1.: left: ejecta out side a radius of 100 km for different artificial viscosity parameter, right: ejecta outside a radius of 1000 km. Different colors indicate different dissipation decay time C_1 and base value ξ^0.

Figure C.2 shows the impact of the different dissipation parameters on different bulk properties of the simulations. The upper left panel shows the evolution of the minimum lapse function in the system which a measure for compactness of the central core. We see, that the dissipation has a direct effect on the compactness. Systems with slower decay time of the dissipation are reaching faster higher compactness then systems with fast decay of dissipation. This can be explained as followed. During the merger the deformed neutron stars expel matter first from the contact interface of the two stars. For low C_1 this interface undergoes stronger heating. The thermal pressure damps down the bounce between the two neutron star cores, which results in a higher minimum lapse as can be seen in the first minimum amplitude in the upper left panel of figure C.2. This is also in accord with the higher average temperature spike in the upper right panel.

This also leads to more matter squeezed out more rapidly at this first contact interface, which can also be seen in figure C.1 at the first 3 ms after merger. While the two neutron stars are merging vortices are forming near the contact interface through shearing. Heating through shearing is with longer dissipation stronger which dampens the quasi-radial motion of the double core structure as can be seen by the weaker amplitudes of the lapse function. While after the first bounce of the two cores the under-density in the center is comparable between the different settings, for low C_1 this smooths out faster in temperature and density and let the fused core spiral more towards the center. This leads to a more spherical symmetric remnant, which can be seen by the comparable weaker m=1 and m=2 density modes in figure C.1 lower panels. Because of that the spiral arms are strongly suppressed which reduces the amounts of ejecta significantly.

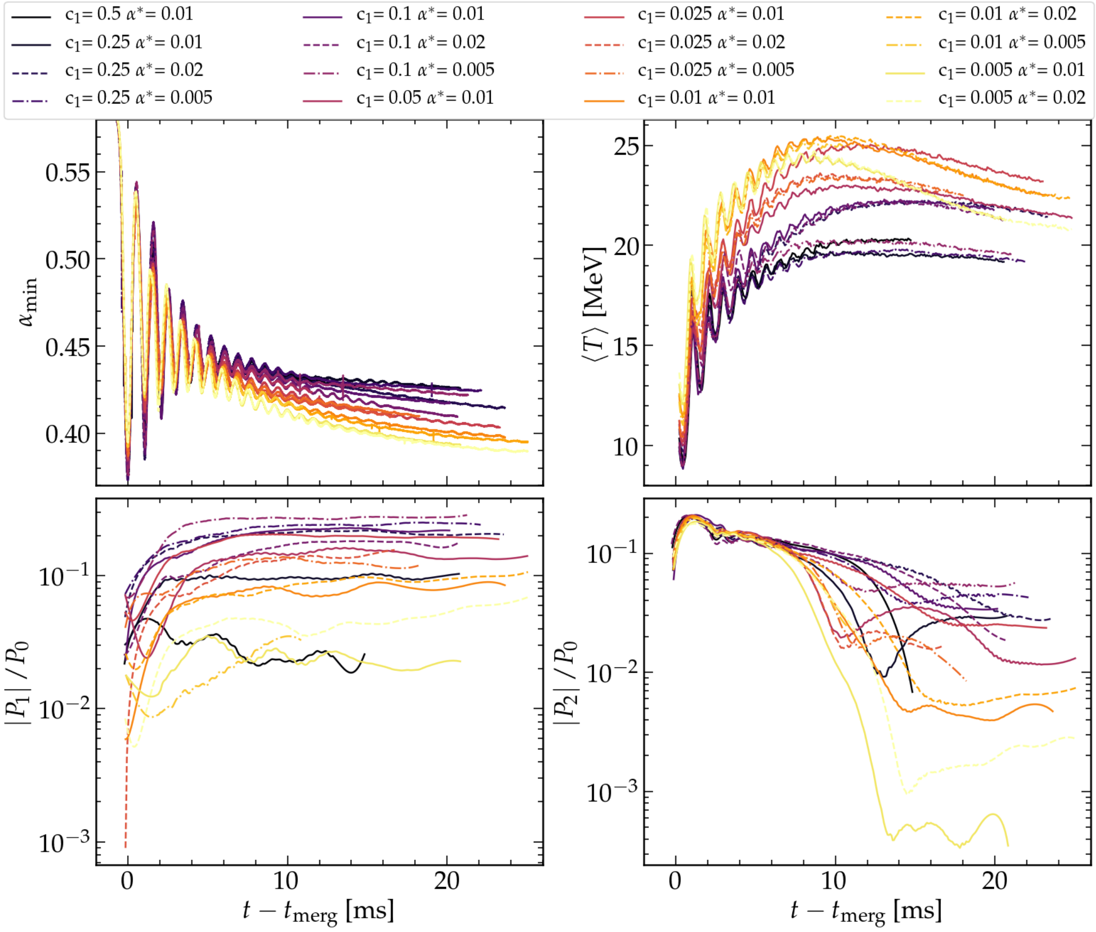

Figure C.2.: Upper left: minimum lapse function α over time. upper right: average temperature over time. lower left: normalized and smoothed amplitude of the m=1 density mode over time. lower right: normalized and smoothed amplitude of the m=2 density mode over time. Different colors indicate different dissipation decay time C_1 and base value ξ^0. m=1 and m=2 modes are smoothed using the Savitzky-Golay filter.

Ejecta mass only grows slowly 5 ms after merger through thermal expansion.

The stronger dissipation also weakens the differential rotation faster which ultimately let the remnant contract faster to a higher density. The thermal expansion cools the disc down and without strong spiral arms which can shock heat the disc matter the average temperature is decreasing faster after 8 to 10 ms after merger. The lapse function shows a clear correlation between the dissipation decay time and the rising compactness of the remnant. For the fastest decay time the variation in the default value ξ^0 becomes non-negligible for how fast the compactness rises. Also a clear correlation between the average temperature and the dissipation is visible. Faster decay in dissipation leads two lower average temperatures of the system.

While stronger dissipation clearly suppresses m=1 mode, the two simulations with the weakest dissipation are also comparatively weaker. We see that stronger dissipation smooth out the under-density in the center of the remnant, while for the simulations with the weakest dissipation the formed hydrodynamic vortices and the corresponding under-density in the center is from the start not strong enough to trigger the off-set of the remnant core which also results in a fainter m=1 mode. Similarly diminishes stronger dissipation the m=2 mode faster. We want to point out, that several simulations have a minimum at around 10 ms after merger and than m=2 gets slightly re-excited. We see similar behavior in the stochasticity simulations, so this behavior may not be in correlations with a change in dissipation.

Bibliography

[1] H.-T. Janka, Annual Review of Nuclear and Particle Science **62**, 407 (2012), arXiv:1206.2503 [astro-ph.SR] .

[2] J. M. Lattimer, Annual Review of Nuclear and Particle Science **71**, 433 (2021).

[3] M. Shibata, *100 Years of General Relativity: Volume 1* (World Scientific, 2015).

[4] J. M. Lattimer, in *Exotic Nuclei and Nuclear/Particle Astrophysics (V) From Nuclei to Stars: Carpathian Summer School of Physics 2014*, American Institute of Physics Conference Series, Vol. 1645 (AIP, 2015) pp. 61–78.

[5] K. Chatziioannou, H. T. Cromartie, S. Gandolfi, I. Tews, D. Radice, A. W. Steiner, and A. L. Watts, arXiv e-prints , arXiv:2407.11153 (2024), arXiv:2407.11153 [nucl-th] .

[6] G. F. Burgio, H. J. Schulze, I. Vidaña, and J. B. Wei, Progress in Particle and Nuclear Physics **120**, 103879 (2021), arXiv:2105.03747 [nucl-th] .

[7] I. Tews, J. M. Lattimer, A. Ohnishi, and E. E. Kolomeitsev, Astrophys. J. **848**, 105 (2017), arXiv:1611.07133 [nucl-th] .

[8] C. Drischler, J. W. Holt, and C. Wellenhofer, Annual Review of Nuclear and Particle Science **71**, 403 (2021), arXiv:2101.01709 [nucl-th] .

[9] S. Huth, C. Wellenhofer, and A. Schwenk, Phys. Rev. C **103**, 025803 (2021), arXiv:2009.08885 [nucl-th] .

[10] S. K. Greif, G. Raaijmakers, K. Hebeler, A. Schwenk, and A. L. Watts, Mon. Not. R. Astron. Soc. **485**, 5363 (2019), arXiv:1812.08188 [astro-ph.HE] .

[11] I. Tews, J. Margueron, and S. Reddy, European Physical Journal A **55**, 97 (2019), arXiv:1901.09874 [nucl-th] .

[12] Y. Lim and J. W. Holt, European Physical Journal A **55**, 209 (2019), arXiv:1902.05502 [nucl-th] .

[13] A. Kurkela, P. Romatschke, and A. Vuorinen, Phys. Rev. D **81**, 105021 (2010), arXiv:0912.1856 [hep-ph] .

[14] O. Komoltsev and A. Kurkela, Phys. Rev. Lett. **128**, 202701 (2022), arXiv:2111.05350 [nucl-th] .

[15] R. C. Tolman, Physical Review **55**, 364 (1939).

[16] J. R. Oppenheimer and G. M. Volkoff, Physical Review **55**, 374 (1939).

[17] J. M. Lattimer and M. Prakash, Science **304**, 536 (2004), arXiv:astro-ph/0405262 [astro-ph] .

[18] G. Baym, H. A. Bethe, and C. J. Pethick, Nucl. Phys. A **175**, 225 (1971).

[19] C. J. Pethick, D. G. Ravenhall, and C. P. Lorenz, Nucl. Phys. A **584**, 675 (1995).

[20] B. S. Sathyaprakash and B. F. Schutz, Living Reviews in Relativity **12**, 10.12942/lrr-2009-2 (2009), arXiv:0903.0338 .

[21] P. C. Peters and J. Mathews, Physical Review **131**, 435 (1963).

[22] C. Cutler and É. E. Flanagan, Phys. Rev. D **49**, 2658 (1994), arXiv:gr-qc/9402014 [gr-qc] .

[23] É. É. Flanagan and T. Hinderer, Phys. Rev. D **77**, 021502 (2008), arXiv:0709.1915 [astro-ph] .

[24] T. Hinderer, B. D. Lackey, R. N. Lang, and J. S. Read, Phys. Rev. D **81**, 123016 (2010), arXiv:0911.3535 [astro-ph.HE] .

[25] K. Hotokezaka, K. Kiuchi, K. Kyutoku, H. Okawa, Y.-i. Sekiguchi, M. Shibata, and K. Taniguchi, Phys. Rev. D **87**, 024001 (2013), arXiv:1212.0905 [astro-ph.HE] .

[26] T. Dietrich, T. Hinderer, and A. Samajdar, General Relativity and Gravitation **53**, 27 (2021), arXiv:2004.02527 [gr-qc] .

[27] T. Hinderer, Astrophys. J. **677**, 1216 (2008), arXiv:0711.2420 [astro-ph] .

[28] A. Bauswein, S. Blacker, G. Lioutas, T. Soultanis, V. Vijayan, and N. Stergioulas, Phys. Rev. D **103**, 123004 (2021), arXiv:2010.04461 [astro-ph.HE] .

[29] K. Hotokezaka, K. Kyutoku, H. Okawa, M. Shibata, and K. Kiuchi, Phys. Rev. D **83**, 124008 (2011), arXiv:1105.4370 [astro-ph.HE] .

[30] A. Bauswein, S. Goriely, and H. T. Janka, Astrophys. J. **773**, 78 (2013), arXiv:1302.6530 [astro-ph.SR] .

[31] L. Baiotti and L. Rezzolla, Reports on Progress in Physics **80**, 096901 (2017), arXiv:1607.03540 [gr-qc] .

[32] A. Bauswein and N. Stergioulas, Journal of Physics G Nuclear Physics **46**, 113002 (2019), arXiv:1901.06969 [gr-qc] .

[33] S. Bernuzzi, General Relativity and Gravitation **52**, 108 (2020), arXiv:2004.06419 [astro-ph.HE] .

[34] R. Fernández and B. D. Metzger, Annual Review of Nuclear and Particle Science **66**, 23 (2016).

[35] H. T. Janka and A. Bauswein, arXiv e-prints , arXiv:2212.07498 (2022), arXiv:2212.07498 [astro-ph.HE] .

[36] B. D. Metzger, Living Reviews in Relativity **23**, 1 (2019), arXiv:1910.01617 [astro-ph.HE] .

[37] N. Stergioulas, A. Bauswein, K. Zagkouris, and H.-T. Janka, Mon. Not. R. Astron. Soc. **418**, 427 (2011), arXiv:1105.0368 [gr-qc] .

[38] A. Bauswein and N. Stergioulas, Phys. Rev. D **91**, 124056 (2015), arXiv:1502.03176 [astro-ph.SR] .

[39] X. Zhuge, J. M. Centrella, and S. L. W. McMillan, Phys. Rev. D **54**, 7261 (1996), arXiv:gr-qc/9610039 [gr-qc] .

[40] M. Shibata, Phys. Rev. Lett. **94**, 201101 (2005), arXiv:gr-qc/0504082 [gr-qc] .

[41] M. Shibata, K. Taniguchi, and K. Uryū, Phys. Rev. D **71**, 084021 (2005), arXiv:gr-qc/0503119 [gr-qc] .

[42] R. Oechslin, H. T. Janka, and A. Marek, Astron. & Astrophys. **467**, 395 (2007), arXiv:astro-ph/0611047 [astro-ph] .

[43] A. Bauswein and H. T. Janka, Phys. Rev. Lett. **108**, 011101 (2012), arXiv:1106.1616 [astro-ph.SR] .

[44] A. Bauswein, H. T. Janka, K. Hebeler, and A. Schwenk, Phys. Rev. D **86**, 063001 (2012), arXiv:1204.1888 [astro-ph.SR] .

[45] K. Takami, L. Rezzolla, and L. Baiotti, Phys. Rev. D **91**, 064001 (2015), arXiv:1412.3240 [gr-qc] .

[46] S. Bernuzzi, T. Dietrich, and A. Nagar, Phys. Rev. Lett. **115**, 091101 (2015), arXiv:1504.01764 [gr-qc] .

[47] J. A. Clark, A. Bauswein, N. Stergioulas, and D. Shoemaker, Classical and Quantum Gravity **33**, 085003 (2016), arXiv:1509.08522 [astro-ph.HE] .

[48] A. Bauswein, N. Stergioulas, and H.-T. Janka, European Physical Journal A **52**, 56 (2016), arXiv:1508.05493 [astro-ph.HE] .

[49] L. Baiotti, Progress in Particle and Nuclear Physics **109**, 103714 (2019), arXiv:1907.08534 [astro-ph.HE] .

[50] J. L. Friedman and N. Stergioulas, International Journal of Modern Physics D **29**, 2041015-632 (2020), arXiv:2005.14135 [astro-ph.HE] .

[51] N. Sarin and P. D. Lasky, General Relativity and Gravitation **53**, 59 (2021), arXiv:2012.08172 [astro-ph.HE] .

[52] M. Ruffert, H. T. Janka, K. Takahashi, and G. Schaefer, Astron. & Astrophys. **319**, 122 (1997), arXiv:astro-ph/9606181 [astro-ph] .

[53] T. Di Matteo, R. Perna, and R. Narayan, Astrophys. J. **579**, 706 (2002), arXiv:astro-ph/0207319 [astro-ph] .

[54] K. Kohri, R. Narayan, and T. Piran, Astrophys. J. **629**, 341 (2005), arXiv:astro-ph/0502470 [astro-ph] .

[55] M. Shibata, Y.-I. Sekiguchi, and R. Takahashi, Progress of Theoretical Physics **118**, 257 (2007), arXiv:0709.1766 [astro-ph] .

[56] M. Shibata and Y. Sekiguchi, Progress of Theoretical Physics **127**, 535 (2012), arXiv:1206.5911 [astro-ph.HE] .

[57] R. Fernández and B. D. Metzger, Mon. Not. R. Astron. Soc. **435**, 502 (2013), arXiv:1304.6720 [astro-ph.HE] .

[58] B. D. Metzger and R. Fernández, Mon. Not. R. Astron. Soc. **441**, 3444 (2014), arXiv:1402.4803 [astro-ph.HE] .

[59] A. Perego, S. Rosswog, R. M. Cabezón, O. Korobkin, R. Käppeli, A. Arcones, and M. Liebendörfer, Mon. Not. R. Astron. Soc. **443**, 3134 (2014), arXiv:1405.6730 [astro-ph.HE] .

[60] O. Just, A. Bauswein, R. Ardevol Pulpillo, S. Goriely, and H. T. Janka, Mon. Not. R. Astron. Soc. **448**, 541 (2015), arXiv:1406.2687 [astro-ph.SR] .

[61] S. Fujibayashi, K. Kiuchi, N. Nishimura, Y. Sekiguchi, and M. Shibata, Astrophys. J. **860**, 64 (2018), arXiv:1711.02093 [astro-ph.HE] .

[62] J. M. Lattimer and D. N. Schramm, Astrophys. J. **210**, 549 (1976).

[63] J. M. Lattimer, F. Mackie, D. G. Ravenhall, and D. N. Schramm, Astrophys. J. **213**, 225 (1977).

[64] D. Eichler, M. Livio, T. Piran, and D. N. Schramm, Nature **340**, 126 (1989).

[65] C. Freiburghaus, S. Rosswog, and F. K. Thielemann, Astrophys. J. Lett. **525**, L121 (1999).

[66] C. Sneden, J. J. Cowan, and R. Gallino, Annu. Rev. Astron. Astrophys. **46**, 241 (2008).

[67] J. J. Cowan, C. Sneden, J. E. Lawler, A. Aprahamian, M. Wiescher, K. Langanke, G. Martínez-Pinedo, and F.-K. Thielemann, Reviews of Modern Physics **93**, 015002 (2021), arXiv:1901.01410 [astro-ph.HE] .

[68] E. M. Burbidge, G. R. Burbidge, W. A. Fowler, and F. Hoyle, Reviews of Modern Physics **29**, 547 (1957).

[69] A. G. W. Cameron, Publ. Astron. Soc. Pacific **69**, 201 (1957).

[70] Y. Z. Qian and S. E. Woosley, Astrophys. J. **471**, 331 (1996), arXiv:astro-ph/9611094 [astro-ph] .

[71] A. Arcones and F. K. Thielemann, Journal of Physics G Nuclear Physics **40**, 013201 (2013), arXiv:1207.2527 [astro-ph.SR] .

[72] J. Lippuner and L. F. Roberts, Astrophys. J. **815**, 82 (2015), arXiv:1508.03133 [astro-ph.HE] .

[73] S. Goriely, A. Bauswein, and H.-T. Janka, Astrophys. J. Lett. **738**, L32 (2011), arXiv:1107.0899 [astro-ph.SR] .

[74] O. Korobkin, S. Rosswog, A. Arcones, and C. Winteler, Mon. Not. R. Astron. Soc. **426**, 1940 (2012), arXiv:1206.2379 [astro-ph.SR] .

[75] S. A. Colgate and C. McKee, Astrophys. J. **157**, 623 (1969).

[76] L.-X. Li and B. Paczyński, Astrophys. J. Lett. **507**, L59 (1998), arXiv:astro-ph/9807272 [astro-ph] .

[77] B. D. Metzger, G. Martínez-Pinedo, S. Darbha, E. Quataert, A. Arcones, D. Kasen, R. Thomas, P. Nugent, I. V. Panov, N. T. Zinner, and et al., Mon. Not. R. Astron. Soc. **406**, 2650 (2010), arXiv:1001.5029 [astro-ph.HE] .

[78] L. F. Roberts, D. Kasen, W. H. Lee, and E. Ramirez-Ruiz, Astrophys. J. Lett. **736**, L21 (2011), arXiv:1104.5504 [astro-ph.HE] .

[79] S. R. Kulkarni, arXiv e-prints , astro-ph/0510256 (2005), arXiv:astro-ph/0510256 [astro-ph] .

[80] S. Goriely, P. Demetriou, H. T. Janka, J. M. Pearson, and M. Samyn, Nucl. Phys. A **758**, 587 (2005), arXiv:astro-ph/0410429 [astro-ph] .

[81] B. D. Metzger, A. Arcones, E. Quataert, and G. Martínez-Pinedo, Mon. Not. R. Astron. Soc. **402**, 2771 (2010), arXiv:0908.0530 [astro-ph.HE] .

[82] D. Kasen, N. R. Badnell, and J. Barnes, Astrophys. J. **774**, 25 (2013), arXiv:1303.5788 [astro-ph.HE] .

[83] M. Tanaka and K. Hotokezaka, Astrophys. J. **775**, 113 (2013), arXiv:1306.3742 [astro-ph.HE] .

[84] B. P. Abbott, R. Abbott, T. D. Abbott, F. Acernese, K. Ackley, C. Adams, T. Adams, P. Addesso, R. X. Adhikari, V. B. Adya, and et al., Astrophys. J. Lett. **848**, L13 (2017), arXiv:1710.05834 [astro-ph.HE] .

[85] B. P. Abbott, R. Abbott, T. D. Abbott, F. Acernese, K. Ackley, C. Adams, T. Adams, P. Addesso, R. X. Adhikari, V. B. Adya, and et al., Astrophys. J. Lett. **851**, L16 (2017), arXiv:1710.09320 [astro-ph.HE] .

[86] B. P. Abbott, R. Abbott, T. D. Abbott, F. Acernese, K. Ackley, C. Adams, T. Adams, P. Addesso, R. X. Adhikari, V. B. Adya, and et al., Astrophys. J. **875**, 160 (2019), arXiv:1810.02581 [gr-qc] .

[87] B. P. Abbott, R. Abbott, T. D. Abbott, F. Acernese, K. Ackley, C. Adams, T. Adams, P. Addesso, R. X. Adhikari, V. B. Adya, and et al., Phys. Rev. Lett. **119**, 161101 (2017), arXiv:1710.05832 [gr-qc] .

[88] B. P. Abbott, R. Abbott, T. D. Abbott, F. Acernese, K. Ackley, C. Adams, T. Adams, P. Addesso, R. X. Adhikari, V. B. Adya, and et al., Astrophys. J. Lett. **848**, L12 (2017), arXiv:1710.05833 [astro-ph.HE] .

[89] A. Goldstein, P. Veres, E. Burns, M. S. Briggs, R. Hamburg, D. Kocevski, C. A. Wilson-Hodge, R. D. Preece, S. Poolakkil, O. J. Roberts, and et al., Astrophys. J. Lett. **848**, L14 (2017), arXiv:1710.05446 [astro-ph.HE] .

[90] V. Savchenko, C. Ferrigno, E. Kuulkers, A. Bazzano, E. Bozzo, S. Brandt, J. Chenevez, T. J. L. Courvoisier, R. Diehl, A. Domingo, and et al., Astrophys. J. Lett. **848**, L15 (2017), arXiv:1710.05449 [astro-ph.HE] .

[91] D. A. Coulter, R. J. Foley, C. D. Kilpatrick, M. R. Drout, A. L. Piro, B. J. Shappee, M. R. Siebert, J. D. Simon, N. Ulloa, D. Kasen, and et al., Science **358**, 1556 (2017), arXiv:1710.05452 [astro-ph.HE] .

[92] M. Soares-Santos, D. E. Holz, J. Annis, R. Chornock, K. Herner, E. Berger, D. Brout, H. Y. Chen, R. Kessler, M. Sako, and et al., Astrophys. J. Lett. **848**, L16 (2017), arXiv:1710.05459 [astro-ph.HE] .

[93] S. Valenti, D. J. Sand, S. Yang, E. Cappellaro, L. Tartaglia, A. Corsi, S. W. Jha, D. E. Reichart, J. Haislip, V. Kouprianov, and et al., Astrophys. J. Lett. **848**, L24 (2017), arXiv:1710.05854 [astro-ph.HE] .

[94] V. A. Villar, J. Guillochon, E. Berger, B. D. Metzger, P. S. Cowperthwaite, M. Nicholl, K. D. Alexander, P. K. Blanchard, R. Chornock, T. Eftekhari, and et al., Astrophys. J. Lett. **851**, L21 (2017), arXiv:1710.11576 [astro-ph.HE] .

[95] G. Hallinan, A. Corsi, K. P. Mooley, K. Hotokezaka, E. Nakar, M. M. Kasliwal, D. L. Kaplan, D. A. Frail, S. T. Myers, T. Murphy, and et al., Science **358**, 1579 (2017), arXiv:1710.05435 [astro-ph.HE] .

[96] R. Margutti, E. Berger, W. Fong, C. Guidorzi, K. D. Alexander, B. D. Metzger, P. K. Blanchard, P. S. Cowperthwaite, R. Chornock, T. Eftekhari, and et al., Astrophys. J. Lett. **848**, L20 (2017), arXiv:1710.05431 [astro-ph.HE] .

[97] E. Troja, L. Piro, H. van Eerten, R. T. Wollaeger, M. Im, O. D. Fox, N. R. Butler, S. B. Cenko, T. Sakamoto, C. L. Fryer, and et al., Nature **551**, 71 (2017), arXiv:1710.05433 [astro-ph.HE] .

[98] B. P. Abbott, R. Abbott, T. D. Abbott, F. Acernese, K. Ackley, C. Adams, T. Adams, P. Addesso, R. X. Adhikari, V. B. Adya, and et al., Phys. Rev. Lett. **121**, 161101 (2018), arXiv:1805.11581 [gr-qc] .

[99] B. P. Abbott, R. Abbott, T. D. Abbott, F. Acernese, K. Ackley, C. Adams, T. Adams, P. Addesso, R. X. Adhikari, V. B. Adya, and et al., Physical Review X **9**, 011001 (2019), arXiv:1805.11579 [gr-qc] .

[100] A. Bauswein, O. Just, H.-T. Janka, and N. Stergioulas, Astrophys. J. Lett. **850**, L34 (2017), arXiv:1710.06843 [astro-ph.HE] .

[101] F. J. Fattoyev, J. Piekarewicz, and C. J. Horowitz, Phys. Rev. Lett. **120**, 172702 (2018), arXiv:1711.06615 [nucl-th] .

[102] K. Kiuchi, K. Kyutoku, M. Shibata, and K. Taniguchi, Astrophys. J. Lett. **876**, L31 (2019), arXiv:1903.01466 [astro-ph.HE] .

[103] B. Margalit and B. D. Metzger, Astrophys. J. Lett. **850**, L19 (2017), arXiv:1710.05938 [astro-ph.HE] .

[104] D. Radice, A. Perego, F. Zappa, and S. Bernuzzi, Astrophys. J. Lett. **852**, L29 (2018), arXiv:1711.03647 [astro-ph.HE] .

[105] L. Rezzolla, E. R. Most, and L. R. Weih, Astrophys. J. Lett. **852**, L25 (2018), arXiv:1711.00314 [astro-ph.HE] .

[106] M. Ruiz, S. L. Shapiro, and A. Tsokaros, Phys. Rev. D **97**, 021501 (2018), arXiv:1711.00473 [astro-ph.HE] .

[107] M. Shibata, S. Fujibayashi, K. Hotokezaka, K. Kiuchi, K. Kyutoku, Y. Sekiguchi, and M. Tanaka, Phys. Rev. D **96**, 123012 (2017), arXiv:1710.07579 [astro-ph.HE] .

[108] D. Kasen, B. Metzger, J. Barnes, E. Quataert, and E. Ramirez-Ruiz, Nature **551**, 80 (2017), arXiv:1710.05463 [astro-ph.HE] .

[109] M. Tanaka, Y. Utsumi, P. A. Mazzali, N. Tominaga, M. Yoshida, Y. Sekiguchi, T. Morokuma, K. Motohara, K. Ohta, K. S. Kawabata, and et al., Publ. Astron. Soc. Japan **69**, 102 (2017), arXiv:1710.05850 [astro-ph.HE] .

[110] D. Watson, C. J. Hansen, J. Selsing, A. Koch, D. B. Malesani, A. C. Andersen, J. P. U. Fynbo, A. Arcones, A. Bauswein, S. Covino, and et al., Nature **574**, 497 (2019), arXiv:1910.10510 [astro-ph.HE] .

[111] E. Berger, Annu. Rev. Astron. Astrophys. **52**, 43 (2014), arXiv:1311.2603 [astro-ph.HE] .

[112] E. Nakar, Phys. Rep. **442**, 166 (2007), arXiv:astro-ph/0701748 [astro-ph] .

[113] E. Nakar, O. Gottlieb, T. Piran, M. M. Kasliwal, and G. Hallinan, Astrophys. J. **867**, 18 (2018), arXiv:1803.07595 [astro-ph.HE] .

[114] A. S. Pozanenko, M. V. Barkov, P. Y. Minaev, A. A. Volnova, E. D. Mazaeva, A. S. Moskvitin, M. A. Krugov, V. A. Samodurov, V. M. Loznikov, M. Lyutikov, and et al., Astrophys. J. Lett. **852**, L30 (2018), arXiv:1710.05448 [astro-ph.HE] .

[115] D. Lazzati, R. Perna, B. J. Morsony, D. Lopez-Camara, M. Cantiello, R. Ciolfi, B. Giacomazzo, and J. C. Workman, Phys. Rev. Lett. **120**, 241103 (2018), arXiv:1712.03237 [astro-ph.HE] .

[116] O. Gottlieb, E. Nakar, T. Piran, and K. Hotokezaka, Mon. Not. R. Astron. Soc. **479**, 588 (2018), arXiv:1710.05896 [astro-ph.HE] .

[117] B. P. Abbott, R. Abbott, T. D. Abbott, S. Abraham, F. Acernese, K. Ackley, C. Adams, R. X. Adhikari, V. B. Adya, C. Affeldt, and et al., Astrophys. J. Lett. **892**, L3 (2020), arXiv:2001.01761 [astro-ph.HE] .

[118] N. Farrow, X.-J. Zhu, and E. Thrane, Astrophys. J. **876**, 18 (2019), arXiv:1902.03300 [astro-ph.HE] .

[119] M. W. Coughlin, T. Ahumada, S. Anand, K. De, M. J. Hankins, M. M. Kasliwal, L. P. Singer, E. C. Bellm, I. Andreoni, S. B. Cenko, and et al., Astrophys. J. Lett. **885**, L19 (2019), arXiv:1907.12645 [astro-ph.HE] .

[120] LIGO Scientific Collaboration, J. Aasi, B. P. Abbott, R. Abbott, T. Abbott, M. R. Abernathy, K. Ackley, C. Adams, T. Adams, P. Addesso, and et al., Classical and Quantum Gravity **32**, 074001 (2015), arXiv:1411.4547 [gr-qc] .

[121] F. Acernese, M. Agathos, K. Agatsuma, D. Aisa, N. Allemandou, A. Allocca, J. Amarni, P. Astone, G. Balestri, G. Ballardin, and et al., Classical and Quantum Gravity **32**, 024001 (2015), arXiv:1408.3978 [gr-qc] .

[122] Kagra Collaboration, T. Akutsu, M. Ando, K. Arai, Y. Arai, S. Araki, A. Araya, N. Aritomi, H. Asada, Y. Aso, and et al., Nature Astronomy **3**, 35 (2019), arXiv:1811.08079 [gr-qc] .

[123] S. T. Shoemake D, Arnaud N, Observing scenario timeline graphic, post-o3 (2025).

[124] B. Iyer, T. Souradeep, C. Unnikrishnan, S. Dhurandhar, S. Raja, and A. Sengupta, Ligo-india, proposal of the consortium for indian initiative in gravitational-wave observations (indigo) (2011).

[125] S. Fairhurst, in *Journal of Physics Conference Series*, Journal of Physics Conference Series, Vol. 484 (IOP, 2014) p. 012007, arXiv:1205.6611 [gr-qc] .

[126] M. Saleem, J. Rana, V. Gayathri, A. Vijaykumar, S. Goyal, S. Sachdev, J. Suresh, S. Sudhagar, A. Mukherjee, G. Gaur, and et al., Classical and Quantum Gravity **39**, 025004 (2022), arXiv:2105.01716 [gr-qc] .

[127] B. F. Schutz, Classical and Quantum Gravity **28**, 125023 (2011), arXiv:1102.5421 [astro-ph.IM] .

[128] B. P. Abbott, R. Abbott, T. D. Abbott, M. R. Abernathy, K. Ackley, C. Adams, P. Addesso, R. X. Adhikari, V. B. Adya, C. Affeldt, and et al., Classical and Quantum Gravity **34**, 044001 (2017), arXiv:1607.08697 [astro-ph.IM] .

[129] M. Punturo, M. Abernathy, F. Acernese, B. Allen, N. Andersson, K. Arun, F. Barone, B. Barr, M. Barsuglia, M. Beker, and et al., Classical and Quantum Gravity **27**, 194002 (2010).

[130] J. R. Wilson and G. J. Mathews, *Relativistic Numerical Hydrodynamics* (2003).

[131] J. A. Font, Living Reviews in Relativity **11**, 7 (2008).

[132] M. Alcubierre, *Introduction to 3+1 Numerical Relativity* (2008).

[133] T. W. Baumgarte and S. L. Shapiro, *Numerical Relativity: Solving Einstein's Equations on the Computer* (2010).

[134] L. Rezzolla and O. Zanotti, *Relativistic Hydrodynamics* (2013).

[135] S. Rosswog, Living Reviews in Computational Astrophysics **1**, 1 (2015), arXiv:1406.4224 [astro-ph.IM] .

[136] J. M. Martí and E. Müller, Living Reviews in Computational Astrophysics **1**, 3 (2015).

[137] V. Springel and L. Hernquist, Mon. Not. R. Astron. Soc. **333**, 649 (2002), arXiv:astro-ph/0111016 [astro-ph] .

[138] K. Kiuchi, S. Fujibayashi, K. Hayashi, K. Kyutoku, Y. Sekiguchi, and M. Shibata, Phys. Rev. Lett. **131**, 011401 (2023), arXiv:2211.07637 [astro-ph.HE] .

[139] S. Bernuzzi and T. Dietrich, Phys. Rev. D **94**, 064062 (2016).

[140] K. Kiuchi, L. E. Held, Y. Sekiguchi, and M. Shibata, Phys. Rev. D **106**, 124041 (2022), arXiv:2205.04487 [astro-ph.HE] .

[141] E. R. Most, L. J. Papenfort, and L. Rezzolla, Mon. Not. R. Astron. Soc. **490**, 3588 (2019), arXiv:1907.10328 [astro-ph.HE] .

[142] D. Radice, A. Perego, K. Hotokezaka, S. A. Fromm, S. Bernuzzi, and L. F. Roberts, Astrophys. J. **869**, 130 (2018), arXiv:1809.11161 [astro-ph.HE] .

[143] C. E. Collins, L. J. Shingles, A. Bauswein, S. A. Sim, T. Soultanis, V. Vijayan, A. Flörs, O. Just, G. Leck, G. Lioutas, and et al., Mon. Not. R. Astron. Soc. **529**, 1333 (2024), arXiv:2309.05579 [astro-ph.HE] .

[144] A. W. Steiner, M. Hempel, and T. Fischer, Astrophys. J. **774**, 17 (2013), arXiv:1207.2184 [astro-ph.SR] .

[145] R. Arnowitt, S. Deser, and C. W. Misner, Physical Review **116**, 1322 (1959).

[146] F. Banyuls, J. A. Font, J. M. Ibáñez, J. M. Martí, and J. A. Miralles, Astrophys. J. **476**, 221 (1997).

[147] J. R. Wilson, G. J. Mathews, and P. Marronetti, Phys. Rev. D **54**, 1317 (1996), arXiv:gr-qc/9601017 [gr-qc] .

[148] J. Isenberg and J. Nester, in *General Relativity and Gravitation. Vol. 1. One hundred years after the birth of Albert Einstein. Edited by A. Held. New York*, Vol. 1, edited by A. Held (1980) p. 23.

[149] M. Shibata, T. W. Baumgarte, and S. L. Shapiro, Phys. Rev. D **58**, 023002 (1998), arXiv:gr-qc/9805026 [gr-qc] .

[150] T. W. Baumgarte, G. B. Cook, M. A. Scheel, S. L. Shapiro, and S. A. Teukolsky, Phys. Rev. D **57**, 7299 (1998), arXiv:gr-qc/9709026 [gr-qc] .

[151] W. Briggs, V. Henson, and S. McCormick, *A Multigrid Tutorial, 2nd Edition* (SIAM, 2000).

[152] G. Faye and G. Schäfer, Phys. Rev. D **68**, 084001 (2003), arXiv:gr-qc/0305101 [gr-qc] .

[153] L. Blanchet, T. Damour, and G. Schaefer, Mon. Not. R. Astron. Soc. **242**, 289 (1990).

[154] M. Kölsch, T. Dietrich, M. Ujevic, and B. Brügmann, Phys. Rev. D **106**, 044026 (2022), arXiv:2112.11851 [gr-qc] .

[155] R. A. Gingold and J. J. Monaghan, Mon. Not. R. Astron. Soc. **181**, 375 (1977).

[156] L. B. Lucy, Astron. J. **82**, 1013 (1977).

[157] Q. Zhu, L. Hernquist, and Y. Li, Astrophys. J. **800**, 6 (2015), arXiv:1410.4222 [astro-ph.CO] .

[158] D. J. Price, Journal of Computational Physics **231**, 759 (2012), arXiv:1012.1885 [astro-ph.IM] .

[159] W. Dehnen and H. Aly, Mon. Not. R. Astron. Soc. **425**, 1068 (2012), arXiv:1204.2471 [astro-ph.IM] .

[160] J. J. Monaghan, Reports on Progress in Physics **68**, 1703 (2005).

[161] J. J. Monaghan, Annu. Rev. Astron. Astrophys. **30**, 543 (1992).

[162] R. Oechslin, S. Rosswog, and F.-K. Thielemann, Phys. Rev. D **65**, 103005 (2002), arXiv:gr-qc/0111005 [gr-qc] .

[163] P. Bodenheimer, G. P. Laughlin, M. Rózyczka, and H. W. Yorke, eds., *Numerical Methods in Astrophysics: An Introduction. Part of the Series in Astronomy and Astrophysics. Edited by Peter Bodenheimer* (2007).

[164] E. Chow and J. J. Monaghan, Journal of Computational Physics **134**, 296 (1997).

[165] J. P. Morris and J. J. Monaghan, Journal of Computational Physics **136**, 41 (1997).

[166] D. S. Balsara, Journal of Computational Physics **121**, 357 (1995).

[167] F. Foucart, P. Mösta, T. Ramirez, A. J. Wright, S. Darbha, and D. Kasen, Phys. Rev. D **104**, 123010 (2021), arXiv:2109.00565 [astro-ph.HE] .

[168] R. Oechslin, *Relativistic neutron stars mergers*, Ph.D. thesis, Universität Basel (2003).

[169] V. Paschalidis, W. E. East, F. Pretorius, and S. L. Shapiro, Phys. Rev. D **92**, 121502 (2015), arXiv:1510.03432 [astro-ph.HE] .

[170] W. E. East, V. Paschalidis, and F. Pretorius, Classical and Quantum Gravity **33**, 244004 (2016), arXiv:1609.00725 [astro-ph.HE] .

[171] D. Radice, S. Bernuzzi, and C. D. Ott, Phys. Rev. D **94**, 064011 (2016), arXiv:1603.05726 [gr-qc] .

[172] A. Savitzky and M. J. E. Golay, Analytical Chemistry **36**, 1627 (1964).

[173] T. Dietrich, S. Bernuzzi, M. Ujevic, and W. Tichy, Phys. Rev. D **95**, 044045 (2017), arXiv:1611.07367 [gr-qc] .

[174] T. Dietrich, M. Ujevic, W. Tichy, S. Bernuzzi, and B. Brügmann, Phys. Rev. D **95**, 024029 (2017), arXiv:1607.06636 [gr-qc] .

[175] S. Fujibayashi, K. Kiuchi, S. Wanajo, K. Kyutoku, Y. Sekiguchi, and M. Shibata, Astrophys. J. **942**, 39 (2023), arXiv:2205.05557 [astro-ph.HE] .

[176] O. Just, V. Vijayan, Z. Xiong, S. Goriely, T. Soultanis, A. Bauswein, J. Guilet, H. T. Janka, and G. Martínez-Pinedo, Astrophys. J. Lett. **951**, L12 (2023), arXiv:2302.10928 [astro-ph.HE] .

[177] J. D. Barrow, Phys. Rev. Lett. **46**, 963 (1981).

[178] S. Suzuki and K.-I. Maeda, Phys. Rev. D **55**, 4848 (1997), arXiv:gr-qc/9604020 [gr-qc] .

[179] C. Verhaaren and E. W. Hirschmann, Phys. Rev. D **81**, 124034 (2010), arXiv:0912.0031 [gr-qc] .

[180] S. Das and S. Roychowdhury, Chaos Solitons and Fractals **179**, 114410 (2024), arXiv:2303.14740 [gr-qc] .

[181] A. Sneppen, D. Watson, A. Bauswein, O. Just, R. Kotak, E. Nakar, D. Poznanski, and S. Sim, Nature **614**, 436 (2023), arXiv:2302.06621 [astro-ph.HE] .

[182] S. Rosswog, O. Korobkin, A. Arcones, F. K. Thielemann, and T. Piran, Mon. Not. R. Astron. Soc. **439**, 744 (2014), arXiv:1307.2939 [astro-ph.HE] .

[183] T. Soultanis, A. Bauswein, and N. Stergioulas, Phys. Rev. D **105**, 043020 (2022), arXiv:2111.08353 [astro-ph.HE] .

[184] G. R. Lee, R. Gommers, F. Waselewski, K. Wohlfahrt, and A. O'Leary, Journal of Open Source Software (2019).

[185] L. Lehner, S. L. Liebling, C. Palenzuela, and P. M. Motl, Phys. Rev. D **94**, 043003 (2016), arXiv:1605.02369 [gr-qc] .

[186] M. Hempel and J. Schaffner-Bielich, Nucl. Phys. A **837**, 210 (2010), arXiv:0911.4073 [nucl-th] .

[187] F. X. Timmes and D. Arnett, Astrophys. J. Suppl. **125**, 277 (1999).

[188] J. M. Aparicio, Astrophys. J. Suppl. **117**, 627 (1998).

[189] W. Benz, in *Numerical Modelling of Nonlinear Stellar Pulsations Problems and Prospects*, edited by J. R. Buchler (1990) p. 269.

[190] A. E. Evrard, Mon. Not. R. Astron. Soc. **235**, 911 (1988).

[191] F. A. Rasio and S. L. Shapiro, Astrophys. J. **377**, 559 (1991).

[192] J. F. Navarro and S. D. M. White, Mon. Not. R. Astron. Soc. **265**, 271 (1993).

[193] M. Steinmetz and E. Mueller, Astron. & Astrophys. **268**, 391 (1993).

[194] H. M. P. Couchman, P. A. Thomas, and F. R. Pearce, Astrophys. J. **452**, 797 (1995), arXiv:astro-ph/9409058 [astro-ph] .

[195] J. Hultman and D. Kaellander, Astron. & Astrophys. **324**, 534 (1997), arXiv:astro-ph/9711136 [astro-ph] .

[196] R. J. Thacker, E. R. Tittley, F. R. Pearce, H. M. P. Couchman, and P. A. Thomas, Mon. Not. R. Astron. Soc. **319**, 619 (2000), arXiv:astro-ph/9809221 [astro-ph] .

[197] J. C. Lombardi, Jr., Z. F. Proulx, K. L. Dooley, E. M. Theriault, N. Ivanova, and F. A. Rasio, Astrophys. J. **640**, 441 (2006), arXiv:astro-ph/0509511 [astro-ph] .

[198] S. Rosswog, Mon. Not. R. Astron. Soc. **498**, 4230 (2020), arXiv:1911.13093 [astro-ph.IM] .

[199] T. S. Tricco, Frontiers in Astronomy and Space Sciences **10**, 1288219 (2023), arXiv:2311.13666 [astro-ph.IM] .

[200] A. Bauswein, T. W. Baumgarte, and H. T. Janka, Phys. Rev. Lett. **111**, 131101 (2013), arXiv:1307.5191 [astro-ph.SR] .

[201] K. Hotokezaka, K. Kiuchi, K. Kyutoku, T. Muranushi, Y.-i. Sekiguchi, M. Shibata, and K. Taniguchi, Phys. Rev. D **88**, 044026 (2013), arXiv:1307.5888 [astro-ph.HE] .

[202] C. J. Krüger and F. Foucart, Phys. Rev. D **101**, 103002 (2020), arXiv:2002.07728 [astro-ph.HE] .

[203] R. Ardevol-Pulpillo, H. T. Janka, O. Just, and A. Bauswein, Mon. Not. R. Astron. Soc. **485**, 4754 (2019), arXiv:1808.00006 [astro-ph.HE] .

[204] C. E. Collins, A. Bauswein, S. A. Sim, V. Vijayan, G. Martínez-Pinedo, O. Just, L. J. Shingles, and M. Kromer, Mon. Not. R. Astron. Soc. **521**, 1858 (2023), arXiv:2209.05246 [astro-ph.HE] .

[205] L. J. Shingles, C. E. Collins, V. Vijayan, A. Flörs, O. Just, G. Leck, Z. Xiong, A. Bauswein, G. Martínez-Pinedo, S. A. Sim, and et al., Astrophys. J. Lett. **954**, L41 (2023), arXiv:2306.17612 [astro-ph.HE] .

[206] V. Vijayan, N. Rahman, A. Bauswein, G. Martínez-Pinedo, and I. L. Arbina, Phys. Rev. D **108**, 023020 (2023), arXiv:2302.12055 [astro-ph.HE] .

[207] A. Neuweiler, T. Dietrich, M. Bulla, S. V. Chaurasia, S. Rosswog, and M. Ujevic, Phys. Rev. D **107**, 023016 (2023), arXiv:2208.13460 [astro-ph.HE] .

[208] Y. Sekiguchi, K. Kiuchi, K. Kyutoku, M. Shibata, and K. Taniguchi, Phys. Rev. D **93**, 124046 (2016), arXiv:1603.01918 [astro-ph.HE] .

[209] D. Radice, F. Galeazzi, J. Lippuner, L. F. Roberts, C. D. Ott, and L. Rezzolla, Mon. Not. R. Astron. Soc. **460**, 3255 (2016), arXiv:1601.02426 [astro-ph.HE] .

[210] L. J. Papenfort, R. Gold, and L. Rezzolla, Phys. Rev. D **98**, 104028 (2018), arXiv:1807.03795 [gr-qc] .

[211] F. Zappa, S. Bernuzzi, D. Radice, and A. Perego, Mon. Not. R. Astron. Soc. **520**, 1481 (2023), arXiv:2210.11491 [astro-ph.HE] .

[212] E. Waxman, E. O. Ofek, D. Kushnir, and A. Gal-Yam, Mon. Not. R. Astron. Soc. **481**, 3423 (2018), arXiv:1711.09638 [astro-ph.HE] .

[213] S. Kitsionas and A. P. Whitworth, Mon. Not. R. Astron. Soc. **330**, 129 (2002), arXiv:astro-ph/0203057 [astro-ph] .

[214] R. Vacondio, B. D. Rogers, P. K. Stansby, P. Mignosa, and J. Feldman, Computer Methods in Applied Mechanics and Engineering **256**, 132 (2013).

[215] M. W. Coughlin, T. Dietrich, B. Margalit, and B. D. Metzger, Mon. Not. R. Astron. Soc. **489**, L91 (2019), arXiv:1812.04803 [astro-ph.HE] .

[216] M. Nicholl, B. Margalit, P. Schmidt, G. P. Smith, E. J. Ridley, and J. Nuttall, Mon. Not. R. Astron. Soc. **505**, 3016 (2021), arXiv:2102.02229 [astro-ph.HE] .

[217] V. Nedora, F. Schianchi, S. Bernuzzi, D. Radice, B. Daszuta, A. Endrizzi, A. Perego, A. Prakash, and F. Zappa, Classical and Quantum Gravity **39**, 015008 (2022), arXiv:2011.11110 [astro-ph.HE] .

[218] M. A. Pérez-García, L. Izzo, D. Barba-González, M. Bulla, A. Sagués-Carracedo, E. Pérez, C. Albertus, S. Dhawan, F. Prada, A. Agnello, and et al., Astron. & Astrophys. **666**, A67 (2022), arXiv:2204.00022 [astro-ph.CO] .

[219] A. Bauswein, R. Oechslin, and H. T. Janka, Phys. Rev. D **81**, 024012 (2010), arXiv:0910.5169 [astro-ph.SR] .

[220] F. Gittins, R. Matur, N. Andersson, and I. Hawke, Phys. Rev. D **111**, 023049 (2025), arXiv:2409.13468 [gr-qc] .